SPINEL-BASED TRANSITION METAL OXIDES AND RELATED SPECIES

SYNTHESIS AND MAGNETIC PROPERTIES OF SPINEL-BASED TRANSITION METAL OXIDES AND RELATED SPECIES

By

JONATHAN EVERETT MITCHELL, B.Sc. (Hons.)

A Thesis

Submitted to the School of Graduate Studies

in Partial Fulfilment of the Requirements

for the Degree

Master of Science

McMaster University

MASTER OF SCIENCE (2009) McMaster University

(Chemistry) Hamilton, Ontario

TITLE: Synthesis and Magnetic Properties of Spinel-Based Transition Metal Oxides.

AUTHOR: Jonathan Everett Mitchell, B.Sc. (Hons.) (University of Western Ontario)

SUPERVISOR: Professor John E. Greedan

NUMBER OF PAGES: xiv, 124

Abstract

Several transition metal oxides were investigated, most based on or derived from the spinel structure. Syntheses included both conventional solid state reactions and chimie douce approaches. The products were characterized by x-ray diffraction, SQUID magnetometry, and in some cases ICP-OES.

The lithium spinels LiM_2O_4 (M = V, Ti) were investigated for chemical lithium insertion and magnetic properties of their lithiated end products. These products, of formula $Li_2M_2O_4$, take on a rock salt structure but maintain the pyrochlore sublattice of the M^{3+} cations, a configuration that is subject to strong geometric magnetic frustration.

Several synthetic pathways for LiV_2O_4 and were investigated and evaluated based on their consistency in producing a chemically pure product with minimal magnetic defects. Although magnetic purity remained elusive, a ceramic synthesis using V_2O_3 and a mixture of $LiVO_3$ and Li_3VO_4 was the most reliable at generating a chemically pure product. The lithiated rock salt $Li_2V_2O_4$ was found to have sample dependent magnetic susceptibility. No Curie-Weiss region was determined up to 600 K, a good indication that the compound is strongly geometrically frustrated.

The investigation of $LiTi_2O_4$ and $Li_2Ti_2O_4$ resulted in the discovery that lithium leaching occurs via lithium-organic phases adsorbed to the particle surfaces during the chimie douce synthesis. While the process occurs in a matter of months

for $LiTi_2O_4$, a partially lithiated sample was completely returned to a pure spinel within a few weeks.

Investigation of the Jahn-Teller distorted spinel $NiRh_2O_4$ revealed the phase $Ni_xRh_{2-x}O_{3-\delta}$, which is related to the structure of orthorhombic Rh_2O_3(III). Magnetic properties of the new compound are unclear due to overlapping magnetic susceptibility with the spinel.

Acknowledgements

"No man is an Iland, intire of itselfe."

- John Donne, "Meditation XVII", *Devotions upon Emergent Occasions*.

The work performed in this thesis could not have been done without the help and support of a great number of people. First and foremost, I would like to thank my supervisor Dr. John Greedan for the wisdom and guidance he has given me in my years at McMaster. His support and direction have been an invaluable resource in the course of my research investigations.

I am also very grateful to Dr. Ignacio Vargas-Baca for the use of laboratory facilities and resources, as well as to Anthony Cozzolino for his tireless assistance and patient instruction concerning reactions with *n*-butyllithium. Special thanks go to those members of the McMaster Chemistry Department and the Brockhouse Institute of Materials Research who have assisted me and provided resources for sample preparation and characterization, namely Dr. Jacques Barbier, Dr. Yurij Mozharivskyj, Dr. Hanna Dabkowska, Dr. Anton Dabkowski, and Jim Garrett. Great appreciation goes to Dr. Paul Dube for the guidance provided in magnetic susceptibility measurements, and to John Rodda for his instruction regarding ICP-OES measurements. I would also like to thank Dr. Gillian Goward for sitting on my supervisory committee and offering a different perspective on my investigations.

Much appreciation goes out to the other members of the Greedan research group, both past and present, who have learned and grown along with me, offering suggestions and direction when I felt lost or confused. Thank you to Dr. Shahab Derakhshan, Dr. Heather Cuthbert, Tomoko Aharen, Farshid Ramezanipour, Dr. Antonio Diego Lozano-Gorrin, Dr. Craig Bridges, and Dr. Andrew Grosvenor.

Special thanks to all the friends who have helped to keep me sane in my time at McMaster, both within the chemistry department and without: Grace Lee, Teri Gullon, Matthew O'hara, Peju Ligali, Kenneth Chalcraft, Amber Chalcraft, Janice Hickey, Christa Homenick, James Anderson, MCGSS, the Stopcocks/Mother Liquors, karaoke friends, the McMaster Thespian Company, and many others. I could not hope to have lasted this long without you.

To my brother, sister, in-laws and nephews for always being there for me when I needed to talk or get away from it all for day or two: Glen, Michelle, Reuben and Thomas Mitchell, and Elizabeth, Daryl and Joshua Banman.

And lastly, to my parents Rick and Donna Mitchell, for always believing in me even when I didn't believe in myself, for their tireless love and unwavering support, and for teaching me to excel in everything I set my hand to. I dedicate this thesis to you.

Table of Contents

List of Tables

List of Figures

Chapter 1: Introduction

1.1 The Spinel Structure

1.1.1 Cubic Spinels

The spinel structure is a well known and robust crystal structure for solid oxide materials, the crystal structure for which is shown in Figure 1-1 [1]. The general formula for a spinel is AB_2X_4, where A and B are metal cations and X is an anion, most often oxygen. Most spinels are cubic with space group $Fd\bar{3}m$, for which this document uses the second setting. The anions form a cubic close packed lattice of 32 atoms per unit cell at Wyckoff position 32*e* (*u*, *u*, *u*). Both tetrahedral and octahedral interstitial sites are formed by this lattice. The A atoms fill one-eighth of the tetrahedral interstitial sites in the O-atom lattice at position 8*a* ($^1/_8$, $^1/_8$, $^1/_8$) with the B atoms filling one-half of the octahedral sites at 16*d* (½, ½, ½). The oxygen position parameter *u* is the only variable atomic position in the structure and usually deviates from the ideal value at $u = ¼$ by shifting slightly closer to the octahedrally coordinated atom, i.e. $u > ¼$, although in a few cases the octahedron is enlarged by $u < ¼$ [1]. This distorts the bond angles of the octahedra from the ideal 90°. The tetrahedral sites maintain their ideal bond angles, with the only effect resulting from $u > ¼$ being a slight enlargement of the interstices relative to the ideal oxygen position.

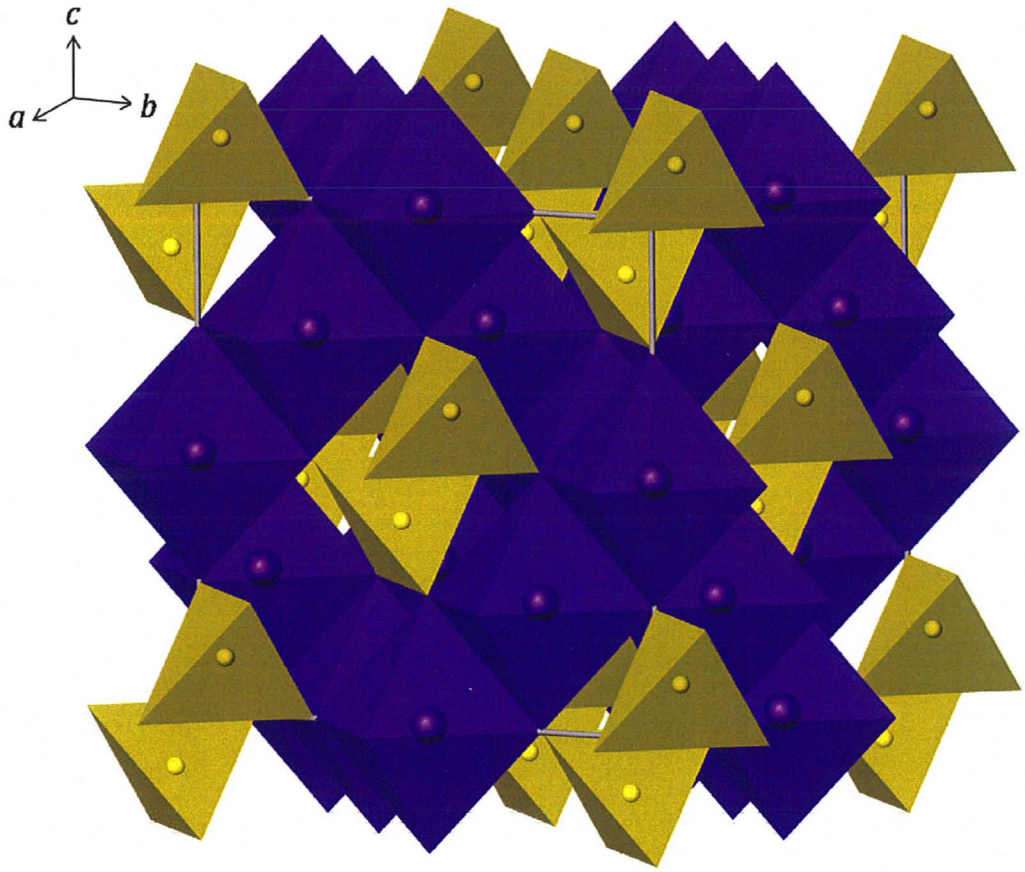

Figure 1-1. Crystal structure of an ideal cubic spinel, space group $Fd\bar{3}m$. The yellow tetrahedra represent A-site cations, the purple octahedral B-site cations, and the oxygen anions are located at the vertices of each polyhedron.

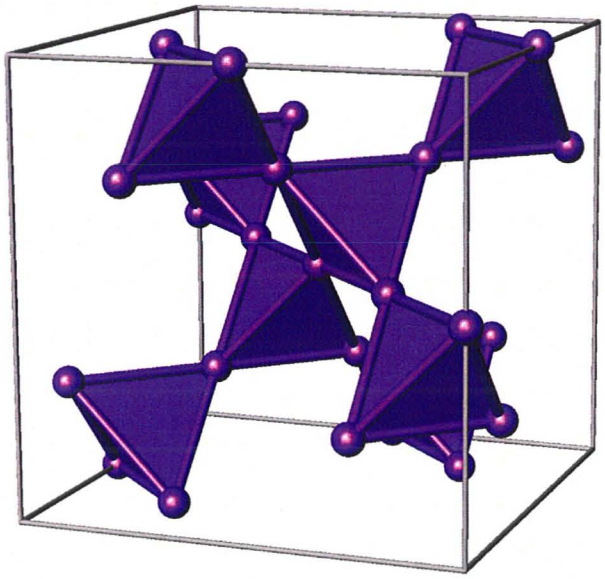

Figure 1-2. The pyrochlore sublattice of B-site ions in a cubic spinel made of a network of corner-sharing tetrahedra.

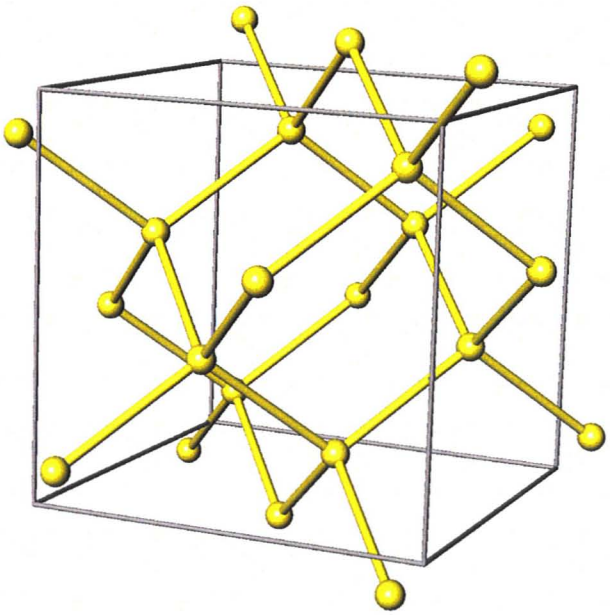

Figure 1-3. The diamond sublattice of A-site cations in a cubic spinel.

Both metal atom sites form a sublattice with other sites of the same type. The B-site atoms lie on a pyrochlore sublattice, *i.e.*, an infinite array of corner-sharing tetrahedra (Figure 1-2). This arrangement is strongly prone to developing geometric frustration, which will be discussed §1.2.3. The A site cations sit on a diamond sublattice where each A atom is surrounded tetrahedrally by four other A atoms (Figure 1-3). Another way to view the diamond lattice is as a lattice of zigzag chains situated in the tunnels formed by the pyrochlore sublattice of the B-cations, which run in the [110], [1$\bar{1}$0], [101], [10$\bar{1}$], [011], and [01$\bar{1}$] directions.

1.1.2 Lithiation of Spinel Phases

Due to the tunnel framework of the A-site cations in the spinel structure, transition metal oxide spinels are excellent candidates for lithium ion insertion. The intercalated lithium ions enter the hitherto empty 16*c* octahedral sites, which at high concentrations displace the 8*a* tetrahedral ions to the remaining 16*c* sites, forming a rock salt phase without alteration of the B-site pyrochlore sublattice (Figure 1-4). The maintenance of this topology at the B-site is crucial in producing novel compounds that display geometric frustration.

Spinel species shown to undertake lithium insertion include Co_3O_4 [2, 3], Fe_3O_4 [4, 5], and Mn_3O_4 [6], as well as the lithium transition metal spinels $LiMn_2O_4$ [6], LiV_2O_4 [7], and $LiTi_2O_4$ [8]. For the $Li_2M_2O_4$ series (M = Mn, V, Ti), only the Mn system has been characterized magnetically. The d^4 Mn^{3+} ions undergo Jahn-Teller

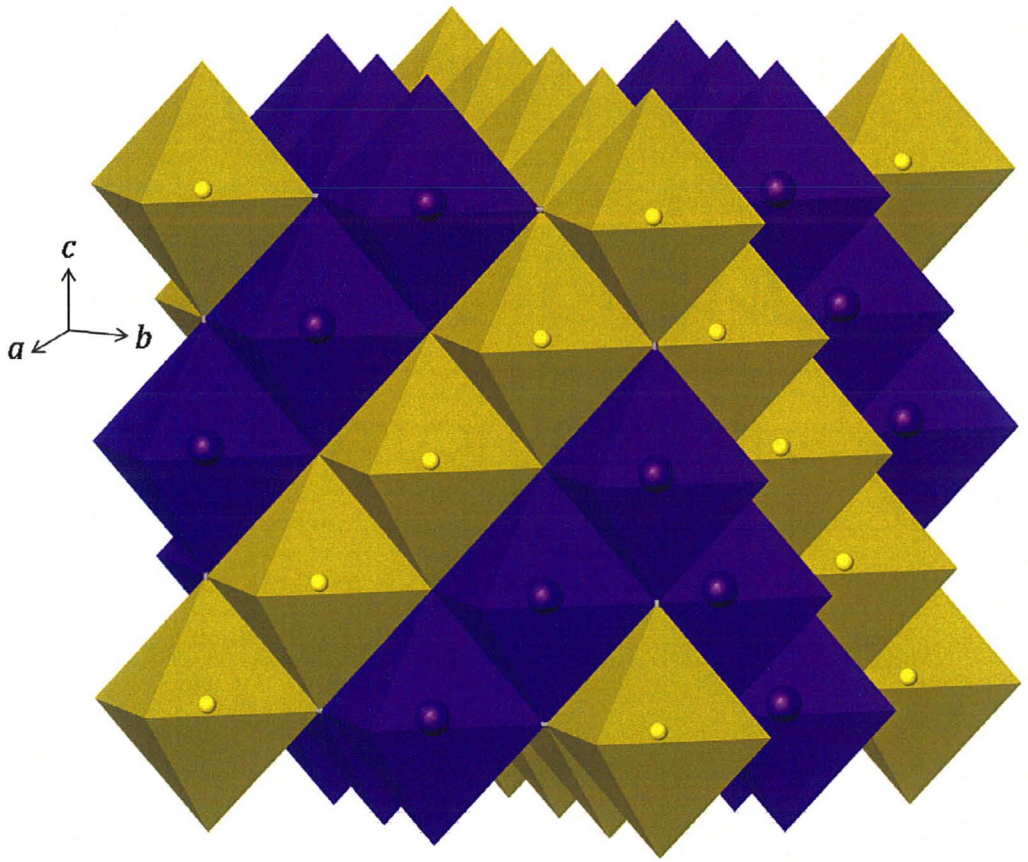

Figure 1-4. Crystal structure of an ideal cubic ordered rock salt, space group $Fd\bar{3}m$, synthesized by lithiation of a cubic spinel to maintain the pyrochlore sublattice of the B-site cations (purple octahedra). Note that the yellow octahedra of the A-site cations also form a pyrochlore sublattice. The anions are represented by the vertices of the polyhedra.

distortions resulting in a tetragonal unit cell with $I4_1/amd$ symmetry and an elongation of the c-axis relative the a-axis [9]. Below ~ 50 K, the magnetic spins develop short-range, two-dimensional correlations Kagomé planes that stack together along the (1 1 1) directions to form the Mn pyrochlore sublattice (See Figures 1-2 and 1-7) [9, 10]. No long range order has been found down to 1.6 K.

The structural and magnetic properties of $Li_2V_2O_4$ and $Li_2Ti_2O_4$ form a significant part of the subject matter of this investigation and will be discussed in Chapters 3 and 4, respectively.

1.2 Magnetism

1.2.1 The Curie-Weiss Law

Magnetism is a property of all materials arising from both the magnetic spins and orbital angular momentum of electrons. Paired electrons have zero spin and orbital angular momentum and are diamagnetic, whereas unpaired electrons lead to paramagnetism. The total magnetic moment can described in terms of the total angular momentum operator $\vec{J}$, which can be deconstructed into the orbital and spin angular momentum operators, $\vec{L}$ and $\vec{S}$, respectively, in the case that the spin-orbit coupling is negligible relative to the crystal field

$$\vec{\mu} = \mu_B g_J \vec{J} = \mu_B(\vec{L} + g_S \vec{S}) \qquad 1.1$$

where $\vec{\mu}$ is the magnetic moment operator, μ_B is the Bohr magneton, g_J is the Landé factor described by

$$g_J = 1 + \frac{J(J+1) + S(S+1) - L(L-1)}{2J(J+1)} \qquad 1.2$$

and g_S the spin-only Landé factor, which is ≈2. For *d*-group transition metals the orbital angular momentum is usually quenched by crystal field effects, *i.e.* $\vec{L} = 0$, and the magnetic moment can be described using only $\vec{S}$. This is known as the spin-only approximation. Of course, compounds with unpaired electrons also contain core diamagnetic paired electrons; however, this diamagnetic contribution is a few orders of magnitude smaller than that of the paramagnetic electrons and is temperature independent so corrections can easily be made [11].

In a paramagnetic material, the localized magnetic states that are thermally accessible can be described according to Boltzmann statistics. By applying a magnetic field, the induced magnetization in the sample can be measured as an indication of this distribution for a particular temperature T. This molar magnetic susceptibility χ can contain both temperature dependent and independent contributions. By applying perturbation theory, the relationship between molar susceptibility and temperature is given by the Van Vleck equation [12].

$$\chi = \frac{\langle \mu \rangle}{H} = \frac{\sum_n \left(\frac{E_n^{(1)^2}}{k_B T} - 2E_n^{(2)} \right) \exp\left(\frac{-E_n^{\circ}}{k_B T} \right)}{\sum_n \exp\left(\frac{-E_n^{\circ}}{k_B T} \right)} \qquad 1.3$$

Where $\langle \mu \rangle$ is the average magnetization, H is the applied magnetic field, k_B is the Boltzmann constant, E is the energy, the bracketed superscripts denote the order of the term according to perturbation theory, and n is the number of accessible states

for each energy term. Several cases arise which can greatly simplify the Van Vleck equation. In the first case, a unique and well defined ground state exists for which there are no accessible excited states, i.e. $E_n^{(2)} = 0$, and only temperature dependent terms remain. By setting the ground state $E_n^{\circ} = 0$, equation 1.3 can be reduced to the Curie law.

$$\chi = \frac{C}{T} \qquad 1.4$$

Where C is the Curie constant, unique for each system. When some of the excited states are thermally accessible, i.e. $E_n^{(2)} \gg k_B T$, then a temperature independent term, denoted χ_0, can be added to the Curie law.

$$\chi = \frac{C}{T} + \chi_0 \qquad 1.5$$

The Curie constant can be deconstructed into equation 1.6.

$$C = \frac{N\mu_B^2}{3k_B}[L(L+1) + 4S(S+1)] \qquad 1.6$$

where N is Avogadro's number. Fortunately, the coefficients to the bracketed expression are all fundamental constants, which reduce to $^1/_8$ when using emu units. Also, the orbital angular momentum contribution is normally quenched for transition metals, simplifying equation 1.6 to $C = \frac{1}{2}S(S+1)$. The effective magnetic moment in the spin-only situation is given by $\mu_{eff} = 2\sqrt{S(S+1)}\mu_B$, resulting in the relationship

$$C = \frac{\mu_{eff}^2}{8} \qquad 1.7$$

However, in non-dilute systems, magnetic spins are coupled to each other through a number of mechanisms, discussed in section 1.2.2. This case is not included in equation 1.3. However, it can in most cases be accounted for by the inclusion of the Weiss constant θ, producing the Curie-Weiss law.

$$\chi = \frac{C}{T - \theta} + \chi_0 \qquad 1.8$$

The Curie-Weiss law holds for a system at higher temperatures, but as T decreases approaching the Curie temperature, T_c, or the Néel temperature, T_N, i.e., the temperatures below which spontaneous ferromagnetism or antiferromagnetism set in, respectively, the magnetic susceptibility curve begins to deviate from that of the paramagnetic case. For a ferromagnet, where adjacent spins are coupled parallel to each other, there is a rapid increase followed by a levelling of the susceptibility as T approaches 0 K, in contrast to the asymptotic character of a purely paramagnetic material. Conversely, antiferromagnets, in which antiparallel coupling between adjacent spins dominates, reach a maximum susceptibility at the Néel temperature, thereafter decreasing as T approaches 0 K (Figure 1-5).

When the inverse of the magnetic susceptibility is plotted against temperature the Weiss constant, θ, is equivalent to the x-intercept, providing an indication of the type of magnetic interactions in the system. A positive value indicates ferromagnetic spin correlations while a negative value is characteristic of antiferromagnetic correlations (Figure 1-5).

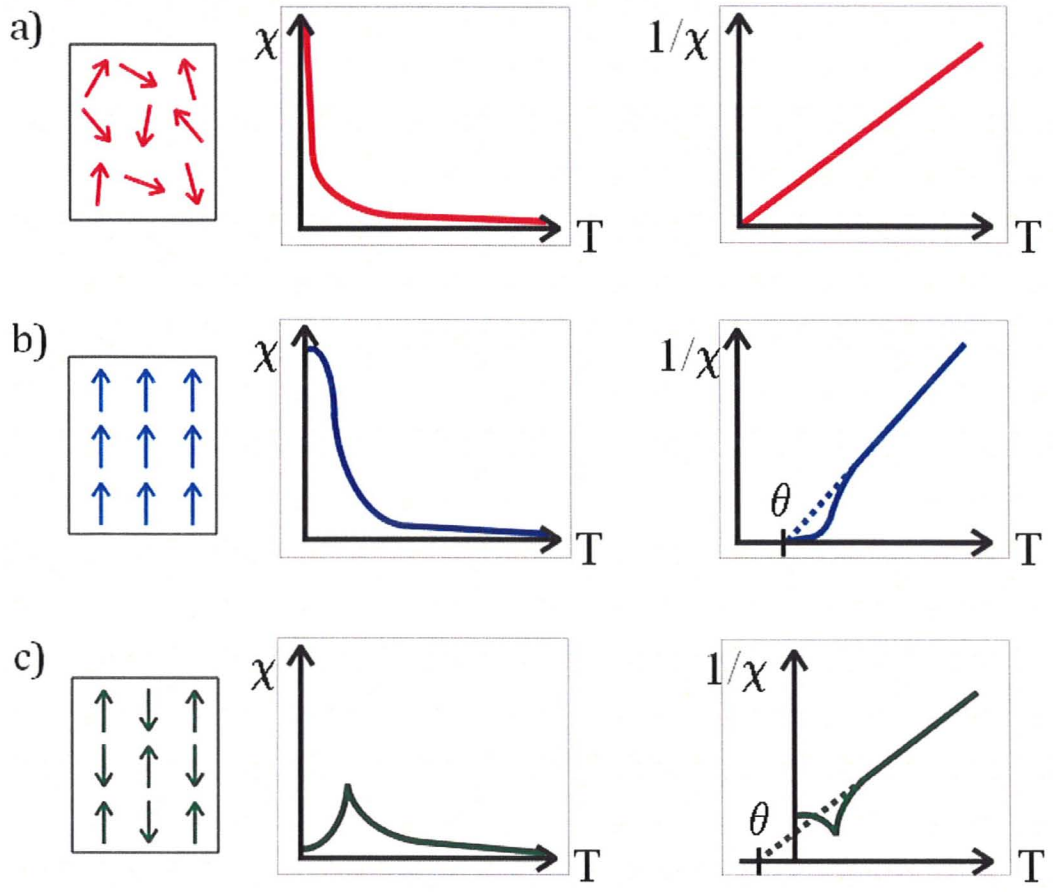

Figure 1-5. Two-dimensional representations of magnetic spin configurations (left), represented by arrows, along with typical magnetic susceptibility response for a χ vs. T plot (center) and $1/\chi$ vs. T plot (right) for each of a) paramagnetism, with randomly fluxuating spins; b) ferromagnetism, with static parallel spins ; and c) antiferromagnetism, with static antiparallel spins.

1.2.2 Magnetic Exchange

The cooperative exchange mechanisms that lead to ferromagnetism and antiferromagnetism have their origins on the electronic level. The interaction between two magnetic spins in neighbouring atoms is described by the Hamiltonian

$$\mathcal{H}_{ex} = -2J\vec{S}_1 \cdot \vec{S}_2 \qquad 1.9$$

where $\vec{S}_1$ and $\vec{S}_2$ are the magnetic spin operators for the two spins involved, and J is the exchange integral (unrelated to the total orbital angular momentum previously described). For a positive value of J a ferromagnetic interaction minimizes the total energy and is thus dominant, while for negative J an antiferromagnetic interaction results in an energy minimum and is preferred. Note that the sign convention is the same as for the Weiss temperature mentioned in §1.2.1. By mean field theory, a relationship between θ and J can be established.

$$\theta = \frac{2S(S+1)}{3k_B}\sum z_m J_m \qquad 1.10$$

where z_m is the number of neighbours of the mth degree for all values of m that $J_m \neq 0$ [13].

There are several pathways involved in magnetic exchange between cations with unpaired d-electrons. The Goodenough-Kanamori rules [14, 15] predict the probable interactions for direct exchange between two cations, as well cation-anion-cation, and even cation-anion-anion-cation exchange mechanisms; however reliable results can only be obtained for 180° and 90° overlapping for M-O-M interactions, M representing the transition metal cation. Competing processes for intermediate

angles make it difficult to predict the sign of J based on a simple set of rules, and more rigorous treatment is necessary. For the 90° cation-anion-cation arrangement seen between edge-sharing B-sites in spinels, some overlap occurs between the t_{2g} orbitals from each neighbouring cation, and so there exists some direct exchange between the transition metal cations. For the simple d^3-d^3 case, this interaction is predicted to be antiferromagnetic.

Another important magnetic interaction is that of superexchange. This process involves electron transfer from the intermediary anion to one or both of the bridging cations. The magnetic spin of the transferred electron is restricted by Hund's Rule and the Exclusion Principle and, since flipping magnetic spins during transfer is forbidden, also depends on the direction of the electron spins in the cations. A simple example for 90° superexchange found in a cubic spinel is d^3-d^3, where two major interactions exist. The first arises from a direct σ-bond overlap between an e_g orbital from each cation with two distinct p-orbitals from the anion, which results in ferromagnetic superexchange shown in Figure 1-6 (top). The second results from indirect π-bonding interaction between t_{2g} orbitals from both cations a single anionic p-orbital, resulting in the antiferromagnetic superexchange illustrated in Figure 1-6 (bottom).

1.2.3 Geometric Frustration

Magnetic frustration results from competition between constraints on magnetic interactions in a lattice such that not all constraints can be satisfied

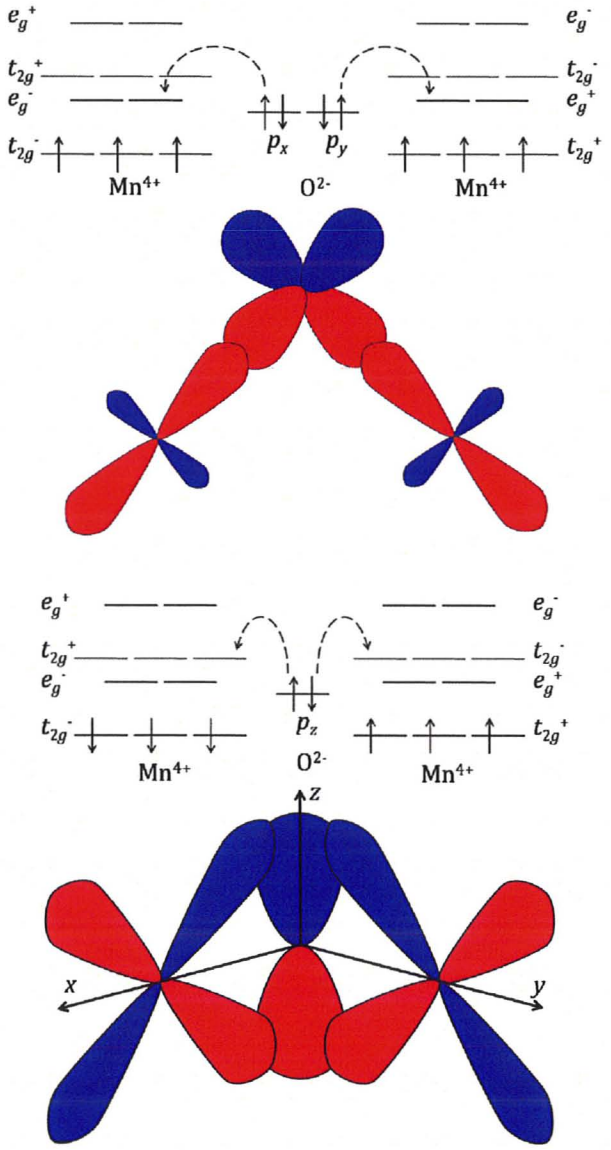

Figure 1-6. 90° magnetic superexchange interactions for a Mn^{4+}—O^{2-}—Mn^{4+} configuration. Top: The σ-bonding interaction. Electrons from two p-orbitals, here denoted as the p_x- and p_y-orbitals, are transferred to the respective empty e_g orbitals of both cations. The orthogonality of the p-orbitals results in ferromagnetic exchange. Bottom: The π-bonding interaction. The electrons from the same p-orbital, here the p_z-orbital, can exchange with the t_{2g} orbitals of both cations simultaneously, resulting in an antiferromagnetic interaction.

simultaneously. When this situation results solely from the topology of the magnetic atoms it is referred to as geometric frustration. The simplest example of a geometrically frustrated arrangement is that of three magnetic spins forming an equilateral triangle where all interactions are antiferromagnetic (Figure 1-7). The triangular plaquette can be extended in two dimensions, forming the edge-sharing triangular lattice or the corner sharing Kagomé lattice, both of which are prone to geometric frustration. In three dimensions the tetrahedron represents the most basic plaquette since it is essentially composed of four edge-sharing equilateral triangles. Lattices using tetrahedra as building blocks include the edge-sharing face centred cubic (Figure 1-7c) and the corner-sharing pyrochlore (Figure 1-2).

The ordering temperature of ferro- or antiferromagnetic material should be set by the Weiss constant, given its relationship with the exchange coupling interactions, *i.e.*, $T_c \approx \theta$. For ferromagnetic materials this approximately holds true and the ratio $|\theta|/T_c \approx 1.1 \rightarrow 1.2$. However, when antiferromagnetic interactions predominate $|\theta|$ can often be 2 to 4 times larger than T_N for a typical antiferromagnet. When dealing with frustrated systems, this ratio is usually enhanced, with strongly frustrated systems indicated by the somewhat arbitrary value of $|\theta|/T_N > 10$.

Long-range ordering in frustrated systems must occur via a compromise between the constraints on a system resulting in a non-collinear configuration known as a Néel state. For a triangle, this means a configuration where the spins are aligned at 120° to each other. Similarly, a compromise for the tetrahedral plaquette

involves the alignment of spins at 109.5° (Figure 1-8). While not a true antiferromagnetic state since the spins are not collinear, the coupling constants between magnetic moments indicate antiferromagnetic interactions and the constraint that the net moment must be zero is satisfied on a global scale rather than by the local coupling interactions.

However, while a lattice may adopt a Néel conformation of magnetic spins, many systems cannot establish long range order. This is especially for true for the pyrochlore lattice. Instead, such systems may adopt a short range ordering configuration, or complex ordering with an expanded magnetic unit cell may result which is believed to involve interactions beyond the nearest neighbours [16].

Many ground states exist which display only short range order. The spin glass is one such arrangement wherein the fluctuating spins of the paramagnetic state freeze in a random configuration below a freezing temperature, T_f. As with a true antiferromagnet, the net magnetic moment averaged over the whole lattice is zero. Evidence for a spin glass state must be collected from many experimental techniques. A divergence between the zero field and field cooled curves in the d.c. magnetic susceptibility data is expected below T_f, and a frequency dependence is seen for χ' in the a.c. susceptibility measurements. The removal of a large amount of entropy below the freezing temperature is expected in heat capacity measurements. Spin dynamics can be mapped by muon spin relaxation or inelastic neutron scattering, revealing the processes involved in spin freezing. Taken together, all

these techniques illuminate the character of the spin glass, eliminating the possibility of other ground states.

The spin liquid, conversely, is a cooperative paramagnetic ground state, where the spins remain dynamic down to the lowest temperature. As such, no T_f is observed. According to the resonance valence bond model, all spins have collinear alignment, forming spin-pairs with antiferromagnetic coupling. Both spins can cooperatively flip, hence maintaining dynamic spin fluctuation while also keeping the overall net magnetic moment zero. An individual spin will not be antiparallel with all of its nearest neighbours in this instance but remains coupled primarily to the other spin in the spin-pair.

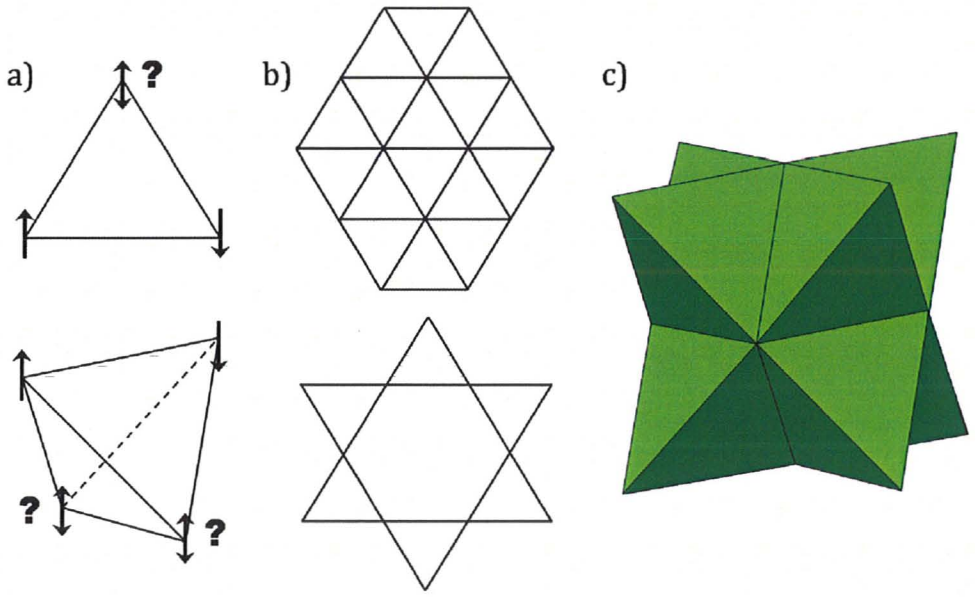

Figure 1-7. Representations of frustrated topologies when antiferromagnetic interactions predominate. a) Simple frustrated plaquettes. Top: Two-dimensional triangular plaquette, where only one of the three magnetic interactions can be satisfied at a given point in time. Bottom: Three-dimensional tetrahedral plaquette, with only one in six interactions satisfied at a time. b) Two dimensional lattices based on the triangular plaquette. Top: The triangular lattice made of edge-sharing triangles. Bottom: the Kagomé lattice made of corner sharing triangles. c) Three-dimensional face-centred cubic lattice, made of a network of edge-sharing tetrahedra.

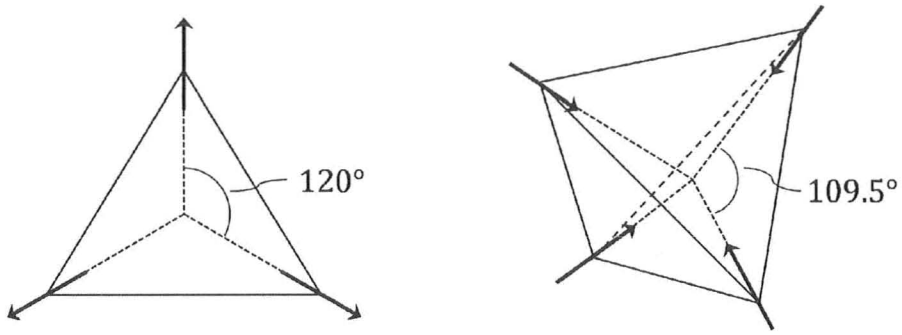

Figure 1-8. Two possible representations of the compromise that can occur for ground states on frustrated antiferromagnetic plaquettes. Left: A 120° triangular plaquette compromise. Right: A 109.5° tetrahedral Néel state.

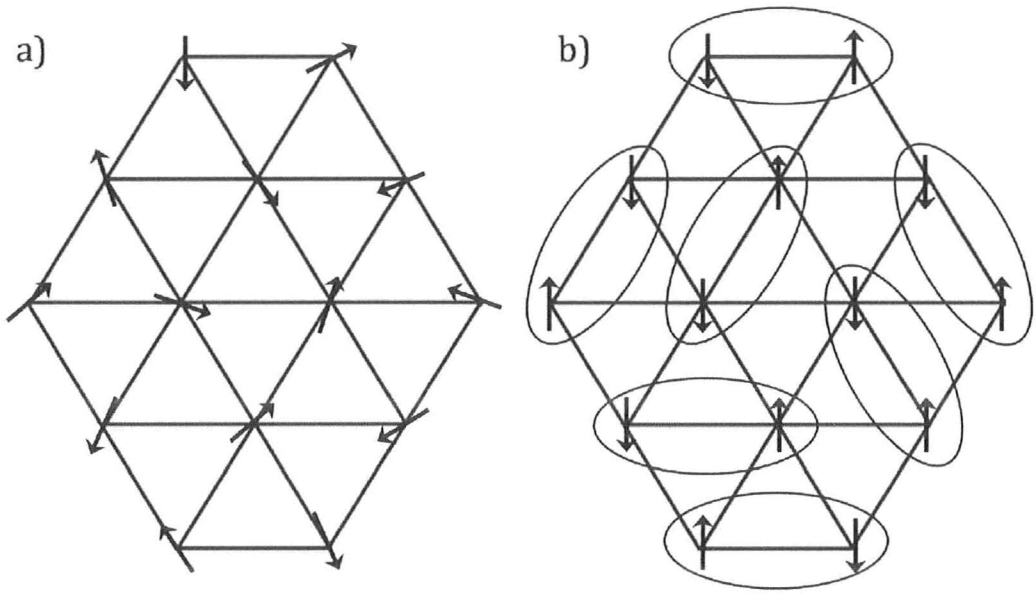

Figure 1-9. Exotic ground states shown on a triangular lattice. a) An example of a spin glass, where the moments freeze in random orientations. Note that this is different from the random dynamic spin orientations shown in Figure 1-5a.
b) The spin liquid, where spin dynamics persist, but spins are paired to form a singlet.

Chapter 2: Experimental Techniques

2.1 Diffraction Theory

2.1.1 Introduction

Any investigation of a material requires an understanding of its elemental composition and crystal structure. Diffraction techniques are particularly useful in determining the crystal structures of solid state materials because of to the regular repeating lattice of atoms, the repeating portion of which is known as a unit cell. X-ray, neutron, and electron diffraction are the three main techniques used to probe solid state structures.

X-ray diffraction is widely used for both powder and single-crystal specimens due to the easy availability of laboratory instruments. The wavelength λ of x-rays is on the order of angstroms and is characteristic of the metal used to construct the source, typically a transition metal such as Cu, Fe, Mo, or Co [17].

$$E_{x-ray} = \frac{hc}{\lambda} \qquad 2.1$$

In the above equation, h stands for Planck's constant and c is the speed of light. Since x-rays are scattered by the electron cloud of an atom, it becomes relatively difficult to detect elements with low atomic numbers with small electron clouds or to differentiate between elements with similar atomic numbers, as is explained later.

Electron diffraction is also relatively accessible and the ability to focus an electron beam at the angstrom level can allow crystal structure determination from a single grain even from a powder sample. Direct-space imaging of micro-crystals at this scale also allows insight into the relationship between real space structure and the diffraction pattern not available by other techniques. However, the strong interaction between electrons and matter frequently result in multiple diffraction events for a single beam of electrons, which can complicate structure determination.

Neutron diffraction differs from x-ray and electron diffraction in that the neutrons interact directly with the nucleus of an atom. The ability of an element to scatter neutrons depends on the composition of the nucleus and is measured by a quantity called the scattering length, which varies from element to element roughly independent of atomic number. As a result the ability of some light elements to scatter neutrons is comparable to that of much heavier elements and in some cases even elements that are adjacent on the periodic table can be distinguished by their widely different scattering lengths. Neutrons are also sensitive to magnetic fields making them an invaluable tool in the determination of magnetic structure. However, neutron sources are fairly scarce and the low intensity of the neutron beam produced requires large samples, on the gram scale, in order to be effective.

The remainder of this section will focus on diffraction theory as it applies to x-ray diffraction. Despite the obvious utility of neutron diffraction to the investigations at hand, no neutron experiments were performed. Its potential application will be discussed further in Chapter 6.

2.1.2 Bragg's Law

Planes of atoms in a crystal lattice form a three-dimensional diffraction grating. Following Bragg, the diffraction phenomenon can be treated as a specular reflection of an x-ray beam from parallel planes with interplanar spacing, d, where θ is the angle of incidence and reflection. Most of these waves will interact destructively upon reflection; however, the requirement for constructive interference of diffracted waves of wavelength λ is satisfied by [18]

$$n\lambda = 2d_{hkl}\sin\theta \qquad 2.2$$

where *hkl* represent the Miller indices of the reflection. This is known as the Bragg equation, and is illustrated in Figure 2-1. The resulting reflections produce an imaginary image in reciprocal space which can be mapped back to the corresponding atomic configuration in direct space. The reciprocal unit cell vectors $(\vec{a}^*, \vec{b}^*, \vec{c}^*)$ are related to their direct space counterparts $(\vec{a}, \vec{b}, \vec{c})$ by the following relationships:

$$\vec{a}^* = \frac{\vec{b}\times\vec{c}}{\left|\vec{a}\cdot(\vec{b}\times\vec{c})\right|} \quad \vec{b}^* = \frac{\vec{c}\times\vec{a}}{\left|\vec{b}\cdot(\vec{c}\times\vec{a})\right|} \quad \vec{c}^* = \frac{\vec{a}\times\vec{b}}{\left|\vec{c}\cdot(\vec{a}\times\vec{b})\right|} \qquad 2.3$$

$$\vec{a}^*\cdot\vec{a} = 1 \qquad \vec{b}^*\cdot\vec{b} = 1 \qquad \vec{c}^*\cdot\vec{c} = 1 \qquad 2.4$$

It is therefore perhaps more useful to consider a crystal structure from its reciprocal space construction. Although no energy is transferred to the lattice in elastic scattering, a small amount of momentum is transferred. This can be quantified as [19]

$$\vec{Q} = \vec{k} - \vec{k}' \qquad 2.5$$

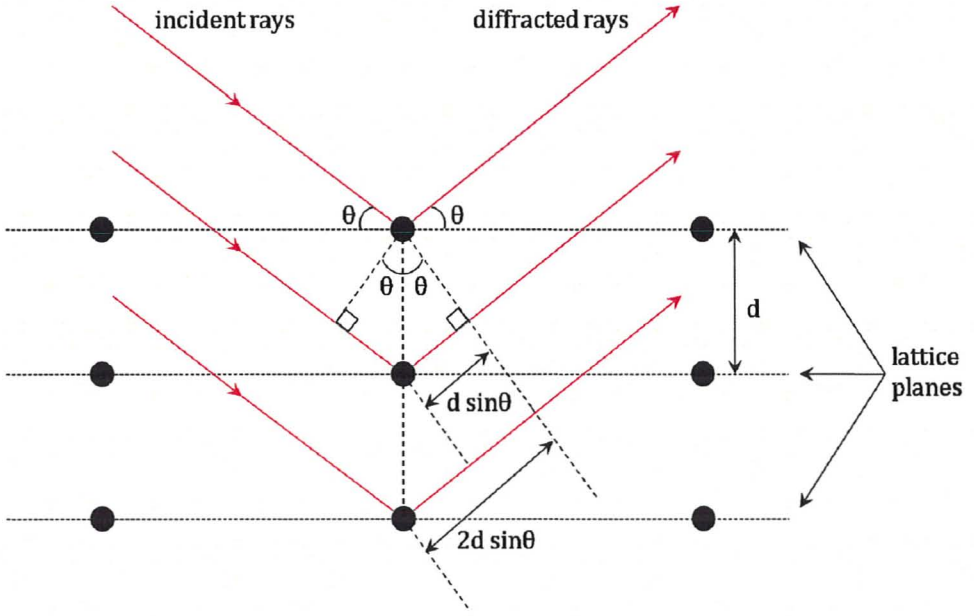

Figure 2-1. Illustration of Bragg's law of constructive interference for reflections from successive crystallographic planes with inter-plane spacing *d*.

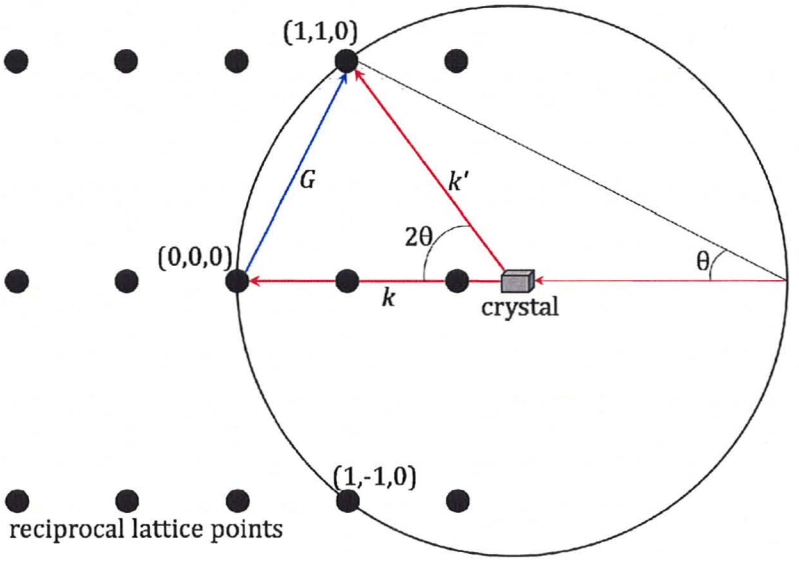

Figure 2-2. Two dimensional representation of Ewald's sphere mapping onto the crystal's reciprocal lattice.

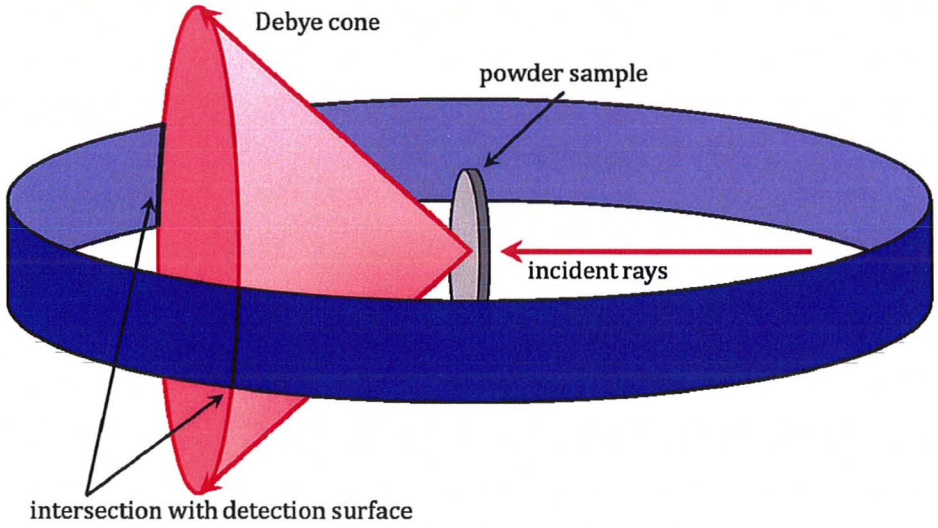

Figure 2-3. Transmission geometry powder diffraction showing the origin of a Debye-Scherrer cone and its intersection with the detection surface.

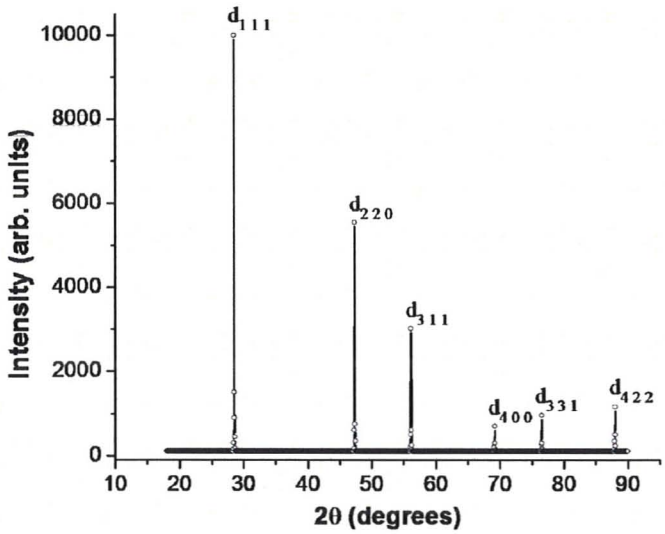

Figure 2-4. Powder x-ray diffraction pattern of elemental silicon. The cubic symmetry of the lattice results in the overlap of several equivalent peaks. For example, d_{220} contains contributions from $d_{\pm2\pm20}$, $d_{\pm20\pm2}$, and $d_{0\pm2\pm2}$ reflections.

where $\vec{Q}$ denotes the transferred momentum and $\vec{k}$ and $\vec{k}'$ are the incident and reflected wave vectors, each with the magnitude $|\vec{k}| = \frac{2\pi}{\lambda}$. By relating this condition to Bragg's Law, it follows that only those wave vectors which differ by a reciprocal lattice vector $\vec{G}$ will be diffracted, i.e. $\vec{G} = \vec{k}' - \vec{k}$ (see Figure 2-2), where

$$\vec{G} = \frac{2\pi}{d_{hkl}} = h\vec{a}^* + k\vec{b}^* + l\vec{c}^* \qquad 2.6$$

For a single crystal, the diffraction pattern results in a lattice of points in reciprocal space which satisfy the conditions of the Ewald's sphere. For poly-crystalline samples, the random orientation of millions of single micro-crystals results in a series of concentric cones of diffraction, or Debye-Scherrer cones, each corresponding to a particular diffraction plane in the real space lattice and hence to a reciprocal vector $\vec{G}$ (Figure 2-3). The superposition of Bragg peaks with equivalent d_{hkl} values, particularly in compounds with high symmetry (Figure 2-4), can be a significant complication for powder diffraction, making it a less powerful method than single crystal diffraction. This can be resolved to some extent through such techniques as the Rietveld method for data refinement [18, 20].

In the Rietveld method, the observed powder diffraction peaks are indexed to a unit cell of known symmetry and dimensions, the content of which is defined by intensity of the Bragg reflections, I_{hkl}. This intensity is in turn proportional to the square of the structure factor, F_{hkl}, defined by

$$F_{hkl} = \sum_{n=1}^{N} f_n(\sin\theta/\lambda)\exp[i2\pi(hx_n + ky_n + lz_n)] \qquad 2.7$$

where x_n, y_n, and z_n are the fractional atomic positions for an atom n with respect to the unit cell, and $f_n(\sin\theta/\lambda)$ is the atomic scattering factor. For x-ray diffraction, this latter quantity defines the number and distribution of electrons with respect to the nucleus for an atom n in the unit cell. Integrating f_n over one atomic site yields the total electron count, Z, for that atom. Thus, the intensity of a diffracted wave is roughly proportional to Z^2, making x-ray diffraction rather insensitive to elements with a low atomic number as compared against heavier elements. Additionally, f_n decays exponentially with $(\sin\theta/\lambda)^2$, resulting in a rapid decrease in peak intensity as diffraction angle increases. However, the widespread availability of x-ray sources for both single-crystal and powder diffraction make it the most useful diffraction technique for initial phase analysis.

2.1.3 X-ray Diffraction

Laboratory x-rays can be produced in an evacuated tube by bombarding a metal (e.g. Cu, Mo, Fe, Co) with electrons produced by thermionic emission from a heated cathode [17]. When the electrons collide with the metal surface, they are decelerated by bremsstrahlung and most of their kinetic energy is transferred to background radiation, forming a continuous spectrum. However, some of the collisions will cause excitation of atomic electrons in core energy levels. As the excited electrons relax to the ground state of the K shell, x-ray energy is released at a wavelength characteristic for the particular metal being bombarded. The emission spectrum for a metal normally has several sharp peaks corresponding to decay from

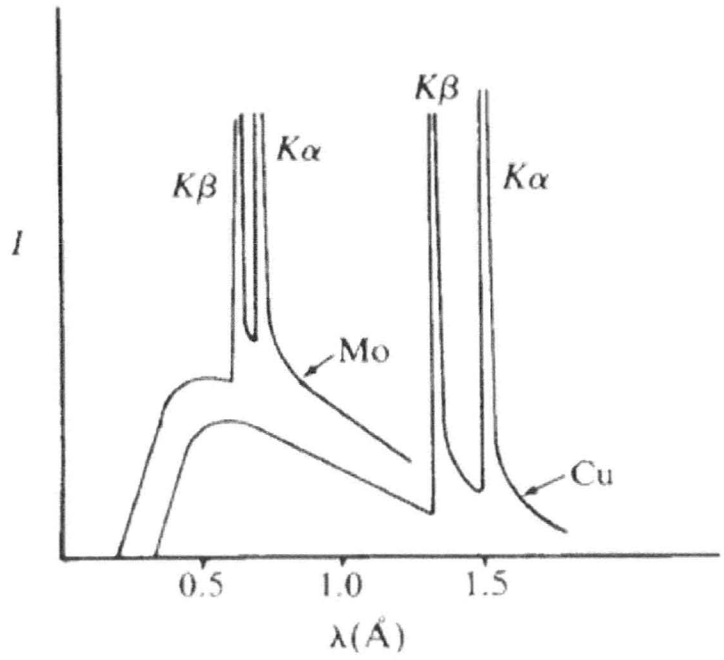

Figure 2-5. Characteristic x-ray spectra for Cu and Mo x-ray sources. Note how the K peaks are split into doublets. Reproduced from Stout & Jensen [17].

the L shell (Kα), the M shell (Kβ), etc, amid a lower intensity background radiation caused by the aforementioned bremsstrahlung.

The spectral lines for a given shell are further split (e.g., into $K\alpha_1$ and $K\alpha_2$ spectral lines, see Figure 2-5) due to the Pauli Exclusion Principle and the requirement for two electrons in an orbital to have opposite spins. Thus, slightly different energies are associated with each electronic decay mechanism. A diffraction pattern collected using both Kα wavelengths would result in a complex pattern of doubled peaks with only slightly different diffraction angles. To simplify the pattern significantly, a monochromator such as single crystal graphite or germanium is usually employed to obtain a single x-ray wavelength, frequently $K\alpha_1$.

X-rays are strongly absorbed by most materials, so care must be taken to ensure that the proper geometry is used to minimize the amount of radiation absorbed. A Guinier-Hägg camera can collect high resolution powder diffraction patterns using transmission geometry, using a monochromator to selectively focus a narrow beam of $K\alpha_1$ radiation to produce high intensity, well-resolved diffraction patterns. The camera uses photographic film to collect a diffraction pattern over a large range of 2θ simultaneously in about an hour. The film must then be developed and digitized by use of a line scanner before it can be analyzed. The most common approach for powder x-ray diffraction experiments involves a diffractometer with Bragg-Brentano reflection geometry, where the x-ray beam is reflected from the sample onto a detector. Diffractometer configurations making use of charge-coupled devices (CCDs) and phosphor screens as the detectors are becoming increasingly common in modern laboratories. Typically, a pattern is collected by rotating the detector around the sample incrementally and taking equally timed measurements, rather than the simultaneous data collection using film technology. Although a quick data set for phase identification can be collected in about the same amount of time as for a Guinier-Hägg camera, a diffraction pattern with significantly higher intensity and resolution can be obtained if the total time for data-collection is extended to several hours. The direct digitization of data is also advantageous in removing the steps of film processing and scanning.

2.1.4 Rietveld Refinement

The most widely used procedure for refining powder data is the Rietveld method, which fits a structural model to the entire observed diffraction pattern, simultaneously, until a good agreement between the model and the experiment is reached [18, 20]. This offers a significant advantage over fitting peaks individually, since the reflection of multiple crystallographic planes with similar d-spacing frequently results in partial or total peak overlap. Using a least-squares refinement, the Rietveld function is minimized to fit the pattern:

$$F = \sum_{i}^{N} w_i \left[y_i(obs) - \frac{1}{c} y_i(calc) \right]^2 \qquad 2.8$$

where w_i is a weighting factor based on the counting statistics ($w_i = 1/\, y_i(obs)$), $y_i(obs)$ and $y_i(calc)$ are the observed and calculated peak intensities at the i^{th} step, and c is a scale factor.

Instrumental parameters must also be taken into consideration, such as the zero point, peak asymmetry, preferred orientation, instrumental resolution, and peak shape, which can have a bearing on the form of the diffraction pattern. The instrumental resolution function describes the full-width at half-maximum (FWHM) as a function of reflection angle:

$$H_{hkl}^2 = U \tan^2 \theta + V \tan \theta + W \qquad 2.9$$

where U is defined by the wavelength resolution $\Delta\lambda/\lambda$, V is due to the beam divergence and mosaic spread of the sample, and W is related to the incident beam cross section and sample diameter [18].

The calculated peak pattern is based on a Gaussian line shape for individual peaks, based on the following equation for the intensity, y_i, at a given position, $2\theta_i$:

$$y_i = t\, F_{hkl}^2\, j_{hkl}\, L_{hkl}\, \frac{2\sqrt{\ln 2}}{H_{hkl}\sqrt{\pi}} \exp\left[-\frac{4\ln 2\,(2\theta_i - 2\theta_{hkl})^2}{H_{hkl}^2}\right] \qquad 2.10$$

where t is the step width of the counter, F_{hkl} is the structure factor of the reflection, j_{hkl} is the multiplicity of the reflection, and θ_{hkl} is the Bragg angle. L_{hkl} is the Lorentz factor which accounts for the way a reciprocal lattice point passes through the Ewald's sphere and depends heavily on the direction from which the point approaches the sphere. Other line shapes such as Lorentzian or Pseudo-Voigt, a convolution of Gaussian and Lorentzian peak shapes, can be employed in the event that a Gaussian fit provides insufficient agreement on its own.

Several agreement factors can be used to evaluate the goodness of fit of the calculated model to the observed diffraction pattern. The profile agreement factor, R_p, is the most obvious choice:

$$R_p = 100\frac{\sum_i |y_i(obs) - y_i(calc)|}{\sum_i |y_i(obs)|} \qquad 2.11$$

However, the weighted R factor, R_{wp}, is more appropriate for handling the statistical weighting of peaks over the full range of reflection angles.

$$R_{wp} = \left[\frac{\sum_i w_i\left(y_i(obs) - y_i(calc)\right)^2}{\sum_i w_i\left(y_i(calc)\right)^2}\right]^{1/2} \qquad 2.12$$

R_{wp} is frequently compared against the expected R factor, R_{exp},

$$R_{exp} = \left[\frac{(N - P + C)}{\sum_i w_i \left(y_i(obs)\right)^2}\right]^{1/2} \qquad 2.13$$

where N is the number of data points, P is the number of refined parameters, and C is the number of constraints. The ratio of their squares, i.e., $\chi^2 = R_{wp}^2/R_{exp}^2$, should be minimized for most refinements.

2.2 DC SQUID

Magnetic susceptibilities are commonly measured using a dc Superconducting Quantum Interference Device (SQUID) magnetometer, which makes use of a superconducting magnet to apply the adjustable external magnetic field. The sample is passed through a small metal loop, which senses minute changes in the magnetic field generated by the induced magnetization of the sample. There are generally three sets of inductance coils measuring 4 cm in total length. The main central pick up coil has twice as many turnings as each of the two smaller coils on either side, which wind in the opposite direction to the main coil. The induced current is converted to voltage, which takes the shape of an inverted parabola over the range of the inductance coils (Figure 2-6). Normally, two independent measurements are taken at a given temperature, each consisting of about 25 data points per parabola, which are then fit to a function describing the expected voltage. This function is in turn averaged over the three measurements and converted to magnetic moment, μ. This can be converted to molar susceptibility using

$$\chi = \frac{\mu}{mols} \div H \qquad 2.14$$

where H is the applied magnetic field.

The high sensitivity of the SQUID is due to its employ of the Josephson junction, which consists of two superconductors separated by a very thin layer of insulating material. The quantum mechanical wave functions from the Cooper pairs which cause the superconductivity leak into the forbidden insulating layer. If that layer is sufficiently thin, the wave functions will overlap, allowing the Cooper pairs to tunnel through the junction. In the absence of a magnetic or electric field, this tunneling produces a direct current through the junction according to the DC Josephson effect. Maintaining a DC voltage difference across the junction produces the AC Josephson effect, where oscillations in the current in the radio frequency range result

The Quantum design SQUID magnetometer is a radio frequency (RF) instrument, which is less sensitive than a direct current (DC) SQUID due to its use of only one Josephson junction, but is still highly sensitive and usually sufficient for transition metal oxides. The Josephson junction is mounted on a superconducting loop coupled in parallel to a resonant LC circuit, i.e. an inductor connected across a capacitor (Figure 2-7). When a difference in d.c. voltage across the junction is maintained, the Cooper pairs tunnel through the junction in an oscillating manner according to the a.c. Josephson effect described above. In the presence of a magnetic field the flow of Cooper pairs is altered by the Meissner effect, which produces

current to oppose changes of magnetic flux in the loop in quantized amounts of $hc/2e = 2 \times 10^{-7}$ Oe·cm^{-2}. This changes the phase of the wave-function, altering the induced AC voltage in the loop, which is then detected by the resonant LC circuit and the signal fed through a lock-in amplifier. The magnetic susceptibility is thus indirectly measured by interpreting from the changes in the AC voltage, which give an indication of the magnetic flux through the loop [21-23].

The SQUID can be operated in two different modes: the DC mode and the RSO or Reciprocating Sample Option mode. The former involves slowly passing the sample through the three inductance coils several times, resulting in an averaged signal with small error. The RSO method uses rapid oscillation of the sample through the coils, significantly reducing the amount of time need to obtain data, and so diminishing experiment time. This process also greatly increases sensitivity while reducing noise.

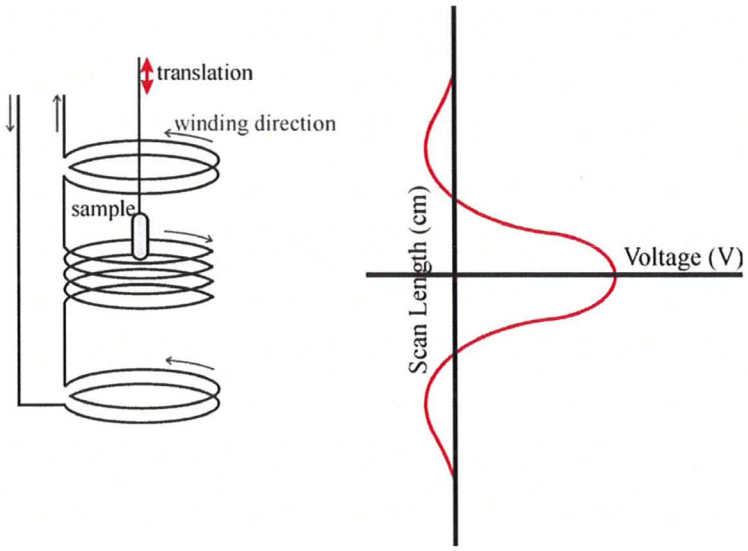

Figure 2-6. Left: Sample translation inside the pick-up coils for a SQUID magnetometer, with alternating coils winding in opposite directions. Right: The voltage signal produced for such a translation. Both images use a common length scale to highlight the correspondence between coil position and signal output. Reproduced from H.L. Cuthbert[24].

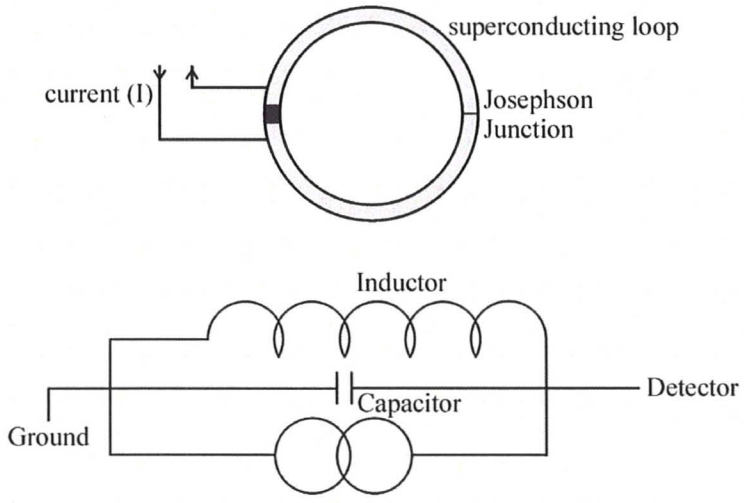

Figure 2-7. The RF SQUID arrangement showing the Josephson junction (top) coupled with the resonant LC circuit (bottom). Reproduced from H.L. Cuthbert [24].

Chapter 3: Synthesis, Structure, and Magnetic Properties of Lithium Vanadium Oxide Spinel-Based Systems

3.1 LiV_2O_4

3.1.1 Background

LiV_2O_4 was first synthesized by Reuter and Jaskowsky in their investigation of the electrical properties of the LiV_2O_4-MgV_2O_4 system, producing polycrystalline samples by reacting Li_2O, V_2O_3, and VO_2 [25]. Most syntheses to date have synthesized polycrystalline powders of the spinel by employing ceramic [25-28], chimie douce [29] or electrochemical methods [7]. Single crystal growth has been achieved by the hydrothermal approach [30], although more recent flux techniques have shown fewer lattice defects [31-33].

Lithium vanadate is a normal cubic spinel crystallizing in the $Fd\bar{3}m$ space group with reported lattice parameters ranging from 8.22 Å [25] to 8.255(6) Å [34], though a majority of references give a value close to 8.24 Å [28], and an oxygen parameter $u \approx 0.26$. Due to the mixed 3+/4+ valency of the vanadium ions it displays metallic properties with a reported single crystal resistivity on the order of 10^{-4} Ω·cm [30]. Magnetic susceptibility measurements have indicated a broad maximum at ~16 K to 20 K [35, 36]. The data could be described by a Curie-Weiss law, with a Curie constant C ranging from 0.35 to 0.535 emu/mol V [36, 30], a Weiss temperature θ between ~ -30 and -63 K [37, 38], and a small temperature

independent term χ_0 on the order of 10^{-5} to 10^{-4} cm^3/mol LiV_2O_4. Krimmel *et al.* [26] found weak ferromagnetic spin correlations for itinerant electrons above 40 K, while antiferromagnetic spin fluctuations dominate below this temperature. No long range order has been found down to 100 mK [39], nor has any geometrically frustrated spin ice or spin glass ground state been discovered.

In 1997 Kondo *et al.* [35] discovered a crossover from localized moments to Fermi liquid behaviour below $T_K \sim 28$ K, wherein the heat capacity coefficient $\gamma(T) \equiv C_p(T)/T$ was found to be 0.42 J/mol K^2 at 1 K. From this, the ratio of the effective mass of conduction electrons to the free electron mass, m^*/m_e, was determined to be 180.5 [40]. This is the first example of a *d*-metal oxide heavy fermion (HF) material, which typically have $m^*/m_e \approx$ 100-1000, a finding that has been confirmed by subsequent studies into the physical properties of LiV_2O_4 [26, 28, 39-44]

Theoretical treatment has taken into account the trigonal D_{3d} point symmetry of the V atoms, which results in a splitting of the t_{2g} orbitals into a lower energy, nondegenerate, localized a_{1g} orbital and two higher energy, doubly degenerate, itinerant e_g' orbitals [45] (not to be confused with the highest energy on-axis e_g orbitals). Density-of-states calculations show a small separation of these orbital states ($\sim$ 0.14 eV) with one of the 1.5 valence electrons per vanadium ion occupying the a_{1g} orbital, while the remaining half-electron partially fills the e_g' orbitals at the Fermi level forming a conduction band [45-49]. This mimics the situation in traditional HF compounds, where weak orbital hybridization between localized *f*-

orbitals and conducting *s*, *p*, and *d* orbitals is responsible for HF behaviour. The origin of HF qualities in LiV_2O_4 remains under considerable debate [50-54].

The remainder of section 3.1 is concerned with the synthetic techniques, structural properties, and magnetic susceptibility measurements of LiV_2O_4. Since the products are intended to be lithiated, producing $Li_2V_2O_4$ (see section 3.2), a chemically pure sample free of magnetic defects is desired. The samples are therefore evaluated in § 3.1.4 on their fulfillment of these criteria.

3.1.2 Experimental

Polycrystalline samples of LiV_2O_4 were prepared in several ways, using both the solid state ceramic method (Samples 1-6) and so called "chimie douce" approaches (Samples 7-13).

Ceramic Preparation

The ceramic method involves the intimate grinding of stoichiometric quantities of powdered starting materials with an agate mortar and pestle, pressing the resulting mixture into one or more pellets, and heating to several hundred degrees Celsius for a reaction to occur. This may be done in air, under a flowing gas, or sealed under vacuum in a fused silica tube, depending on the requirements for the particular reaction.

For all reactions, lithium vanadium oxide precursors, namely beige $LiVO_3$, pale yellow Li_3VO_4, and a 50 % mixture of the two nominally denoted as $Li_2VO_{3.5}$, were synthesized by reaction of an intimately ground and pelletized mixture

containing stoichiometric amounts of yellow V_2O_5 (99 %, Alfa Inorganics) with a 5 % excess of white Li_2CO_3 (99.1 %, J.T. Baker) powders for about one day at 550 °C. The pellets were fired in an alumina crucible open to air to allow for the evolution of carbon dioxide gas. X-ray diffraction was used in each case to determine phase formation and confirm complete decomposition of the carbonate, releasing CO_2. In some cases, additional firing time was needed. Black $LiVO_2$ was synthesized by reducing pellets of $LiVO_3$ under flowing hydrogen at 800 °C for about a day. V_2O_3 was produced by heating V_2O_5 to 600 °C under flowing H_2 gas for 12 hours.

All samples prepared by ceramic methods were placed in a platinum crucible and sealed under vacuum in fused silica tubes. The reaction details and known impurity phases are summarized in Table 3-1. In all cases, at least one regrinding step was needed. The "VO" (99.5 %, CERAC) powder used to synthesize samples 1 and 2 was determined to have a formula of $VO_{0.94}$ when analyzed by thermo-gravimetric analysis (TGA). No measures were taken to make up for this slight oxygen deficiency. The VO_2 (99.5 %, CERAC) used to synthesize Sample 3 was found by TGA to have partially oxidized to V_6O_{13} over time, with an average composition of $VO_{2.075}$. The ratio of this starting material with V_2O_3 was adjusted accordingly to account for this change in stoichiometry. Firing temperatures were kept relatively low, with T_{max} = 800 °C, to prevent evaporation of Li_2O, resulting in long reaction times of at least 10 days. LiV_2O_4 is a black compound which frequently contains many highly reflective facets upon removal from the furnace, an indication of microcrystal formation.

Chimie Douce Preparations

So-called "chimie douce" methods involve the use of reagents to topotactically alter the chemical composition of a solid state compound at relatively low temperatures (i.e., <500 °C), while maintaining the structural framework. In the synthesis of LiV_2O_4, this involves the removal of half the lithium from layered $LiVO_2$ by chemical means, followed by firing the resulting powder at a temperature of at least 300 °C for two days. In practice 550 °C is required for a more crystalline product. $LiVO_2$ was synthesized as described above. Reaction conditions and impurity phases for each sample are summarized in Table 3-2.

Sample 7 was produced by reaction of $LiVO_2$ with a stoichiometric amount of aqueous $Na_2S_2O_8$ (98+ %, Sigma-Aldrich) open to air at ambient temperature over four days. The aqueous phase was decanted and the residue washed three times with water, then with methanol, and finally acetone to dry it. The powder was pressed into a pellet and heated to 300 °C in a platinum crucible sealed in a fused silica tube for 10 days.

Samples 8 through 12 were synthesized by reaction of $LiVO_2$ with gaseous I_2 in an evacuated fused silica tube at 220 °C for 2-3 days. In each case, some dark purple iodine gas remained unreacted, and was isolated by gradually removing the reaction vessel from the tube furnace, causing the I_2 gas to deposit as a solid at the cooler end of the vessel. The presence of the expected LiI byproduct was confirmed by the high hygroscopicity of the sample and by X-ray diffraction which indicated a composition of $LiI{\cdot}3H_2O$. This byproduct was removed by washing three times with

methanol, after which the solid phase was separated by centrifugation and the liquid phase decanted. The $Li_{0.5}VO_2$ powder was then returned to an evacuated fused silica tube and heated to undergo the transformation to LiV_2O_4. The variations taken in each reaction process are recorded in Table 3-2.

Sample 13 was prepared at ambient temperature by reacting $LiVO_2$ with a stoichiometric amount of I_2 dissolved in chloroform under a nitrogen atmosphere. The system was reacted at room temperature for two weeks while waiting for the disappearance of the characteristic brown colour of the dissolved I_2, which did not occur. After allowing the product to settle and decanting the liquid phase, the solid phase was washed with chloroform three times. The product was further washed with methanol to remove any residual $LiI{\cdot}3H_2O$ as described above, then heated in an evacuated fused silica tube to 300 °C for 2 days, followed by an additional 24 hours at 550 °C.

Powder X-ray Diffraction

The polycrystalline products were examined using one of two x-ray powder diffractometers. Samples 1, 2, and 3 were analyzed using a Guinier-Hägg camera equipped with a Cu $K\alpha_1$ radiation source (λ = 1.54056 Å) from 2θ = 15° to 65°. High purity elemental silicon was used as an internal standard, the diffraction pattern for which is shown in Figure 2-4. The reflection peaks were recorded on photographic film which was developed and digitized using a KEJ LS20 line scanner.

Table 3-1. Reaction conditions and impurity phases for ceramic syntheses of LiV_2O_4. Molar percent impurities were estimated using the Rietveld scaling factors via the method described by Hill & Howard [57].

Sample	Reaction Conditions	Impurity Phase(s)
1	$LiVO_3 + VO$ - 10 days at 750 °C - White lining formed on inside of silica tube	None evident (Guinier)
2	$LiVO_3 + VO$ - 10 days at 750 °C - White lining formed on inside of silica tube	None evident (Guinier)
3	$^1/_3\ Li_3VO_4 + {}^2/_3\ V_2O_3 + {}^1/_3\ VO_2$ - Total of 25 days at temperatures ranging from 600-800 °C - White lining on formed on inside of silica tube	Li_3VO_4, $LiVO_3$, unknown
4	$\frac{1}{2}\ Li_2VO_{3.5} + \frac{3}{4}\ V_2O_3$ - 10 days at 700 °C - Ratio Li:V 0.95:2 (ICP-OES)	Trace
5	$\frac{1}{2}\ Li_2VO_{3.5} + \frac{3}{4}\ V_2O_3$ - 14 days at 700 °C - Ratio Li:V 1.09:2 (ICP-OES)	Trace
6	$LiVO_2 + \frac{1}{4}\ V_2O_3 + \frac{1}{4}\ V_2O_5$ - 13 days at 650 °C, 11 days at 750 °C	Li_3VO_4 (5.9 %), V_4O_7 (0.6 %)

Table 3-2. Reaction conditions and impurity phases for chimie douce syntheses of LiV_2O_4. Molar percent impurities were estimated using the Rietveld scaling factors via the method described by Hill & Howard [57].

Sample	Reaction Conditions and Delithiating Agents	Impurity Phase(s)
7	$Na_2S_2O_8$ (aq) • Washed with H_2O, MeOH, then acetone • Heated to 300 °C for 10 days	Amorphous, unknown (trace)
8	$I_2(g)$ • Washed with MeOH • Heated to 300 °C for 2 days after washing	LiV_2O_5 (1.8 %), Li_3VO_4 (trace), Amorphous
9	I_2 (g) • Heated to 350 °C for 2 days before washing • Washed with MeOH • Heated to 700 °C for 3 days • Ratio Li:V 1.04:2 (ICP-OES)	$LiVO_2$ (2.5 %)
10	I_2 (g) • ~5% molar excess I_2 • Washed with MeOH • Heated to 300 °C then 550 °C for 24 hours each after washing • Ratio Li:V 0.93:2 (ICP-OES)	V_2O_3 (3.7 %), $LiVO_2$ (2.7 %)
11	I_2 (g) • ~10 % molar excess I_2 • Heated to 550 °C for 2 days before washing • Washed with MeOH	V_2O_3, V_3O_5, Li_3VO_4, unidentified phases
12	I_2 (g) • ~3 % molar excess I_2 • Heated to 550 °C for 2 days before washing • Washed with MeOH	V_2O_3, V_3O_5, Li_3VO_4, unidentified phases
13	I_2 (in $CHCl_3$) • Left with stirring for two weeks • Washed with $CHCl_3$ • Heated to 300 °C for 2 days, then 550 °C for 24 hours after washing	$LiVO_2$ (15.3 %), V_2O_3 (11.0 %)

All remaining samples were analyzed using a PANalytical X'Pert PRO diffractometer using a Cu $K\alpha_1$ radiation source, Ge monochromator, and sample spinner. The data were collected over a 2θ range from 10° to 80°. Data sets were collected with a step size of 0.0083556 ° a step time of either 100 s or 850 s. Rietveld data refinement was carried out using the General Structure Analysis System Experiment Graphical User Interface (GSAS-EXPGUI) software package [55, 56]. Molar percentages of impurity phases for each sample were estimated by conversion from the weight fraction W_p of phase p determined using the Hill and Howard method [57]:

$$W_p = \frac{S_p(ZMV)_p}{\sum_i S_i(ZMV)_i} \qquad 3.1$$

where S is the Rietveld scaling factor, Z is the number of formula units per unit cell, M is the formula mass of the phase, and V is the volume of the unit cell. Due to the strength of the impurity phase signals, Samples 11 and 12 were not subjected to Rietveld refinement.

ICP-OES

The ratios of Li:V for Samples 4, 5, 9, and 10 were probed by inductively coupled plasma equipped with an optical emission spectrometer (ICP-OES) using a Varian Vista Pro Spectrometer. Carefully weighed samples were digested in a concentrated 2:5 solution of HNO_3:H_2SO_4 with the aid of a Milestone Ethos Pro microwave oven. The resulting solutions were volumetrically diluted, then vaporized in a high-temperature plasma. The vaporized ions excited in the plasma

emit light at wavelengths characteristic for each element. The light is dispersed through a grating and the intensities at pre-calibrated emission wavelengths were captured by CCD camera. These light intensities were converted to concentration following a simple linear relationship established beforehand using standard solutions with known concentrations of the elements being probed. The results are recorded in Tables 3-1 and 3-2 for samples where ICP-OES data were collected.

Magnetic Measurements

Magnetic measurements were performed for Samples 2, 4, 5, 9, and 10 using a Quantum Design MPMS SQUID magnetometer. Samples were encased in a gelatin capsule. Using the RSO mode, zero field cooled (ZFC) and field cooled (FC) data were collected at 2 K increments over the range 2-30 K and at 5 K increments from 35 to 300 K. The applied magnetic field was either 100 Oe or 500 Oe (see Table 3-6), which were also the field strengths used for the FC measurements. The inverse susceptibility curves were fitted to a Curie-Weiss law using a non-linear curve fitting function. Fits to Samples 4, 5 and 9 were performed using the inverse ZFC curve. The FC curve was used for Sample 2 due to several noisy points in the ZFC data. For Sample 10 a slight kink in the data at ~230 K becomes apparent in the inverse ZFC curve and the Curie-Weiss fit was performed using the FC data instead.

3.1.3 Results

Structural Characterization

The observed powder x-ray diffraction (XRD) pattern for Sample 4, along with the pattern calculated by Rietveld refinement, expected Bragg reflections, and difference pattern is shown in Figure 3-1. Powder XRD patterns for all other samples of LiV_2O_4 are included in the Appendix along with the respective Rietveld refinement, where applicable. The unit cell parameter *a*, oxygen position parameter *u*, and Rietveld agreement factors for each sample are recorded in Table 3-3 and interatomic distances and bond angles for Sample 4 are given in Tables 3-4 and 3-5, respectively. All thirteen samples had lattice parameters within the range found in the literature [28].

The powder patterns for two different solid state reactions, represented by Samples 1 and 2 and Samples 4 and 5 respectively, showed no evidence of the formation or retention of impurity phases, or their signals were so small at the level of detection as to be considered insignificant. Impurities formed for both Sample 3 and Sample 6 and were retained even after extended and repeated reaction periods. For Sample 3, the main impurities were Li_3VO_4 and $LiVO_3$ along with at least one unidentified phase. The relatively low quality of the data collection prevented an estimate by Rietveld refinement as to the molar percent of the impurity phases. For Sample 6, Li_3VO_4 and V_2O_7 were identified with an estimated mole percent of 5.9 % and 0.6 %, respectively.

Table 3-3. Lattice parameter a, oxygen position parameter u, and Rietveld refinement agreement factors for all syntheses of LiV_2O_4.

Sample	a (Å)	u (fractional coordinate)	R_p	R_{wp}	χ^2
1	8.2435(1)	N/A	N/A	N/A	N/A
2	8.2332(2)	N/A	N/A	N/A	N/A
3	8.2403(2)	N/A	N/A	N/A	N/A
4	8.24331(3)	0.26296(9)	0.0392	0.0498	1.70
5	8.24751(2)	0.2605(2)	0.0777	0.1036	1.35
6	8.24023(3)	0.2618(2)	0.0732	0.0940	1.53
7	8.24271(8)	0.2639(2)	0.0690	0.0886	2.90
8	8.2406(1)	0.2584(2)	0.0696	0.0902	2.10
9	8.24487(2)	0.2601(1)	0.0648	0.0845	0.914
10	8.24698(4)	0.2571(1)	0.0606	0.0789	1.14
11	8.2420(4)	N/A	N/A	N/A	N/A
12	8.2443(9)	N/A	N/A	N/A	N/A
13	8.2444(1)	0.2590(3)	0.0715	0.0909	1.23

Table 3-4. Selected interatomic distances for Sample 4.

Atoms	Distance (Å)
Li – O	1.970(1)
V – O	1.9598(7)
V – V	2.91445(1)

Table 3-5. Selected bond angles for Sample 4.

Atoms	Angle (°)
O – Li – O	109.4712(3)
O – V – O	83.59(5)
O – V – O	96.41(5)
Li – O – V	120.84(3)
V – O – V	96.07(5)

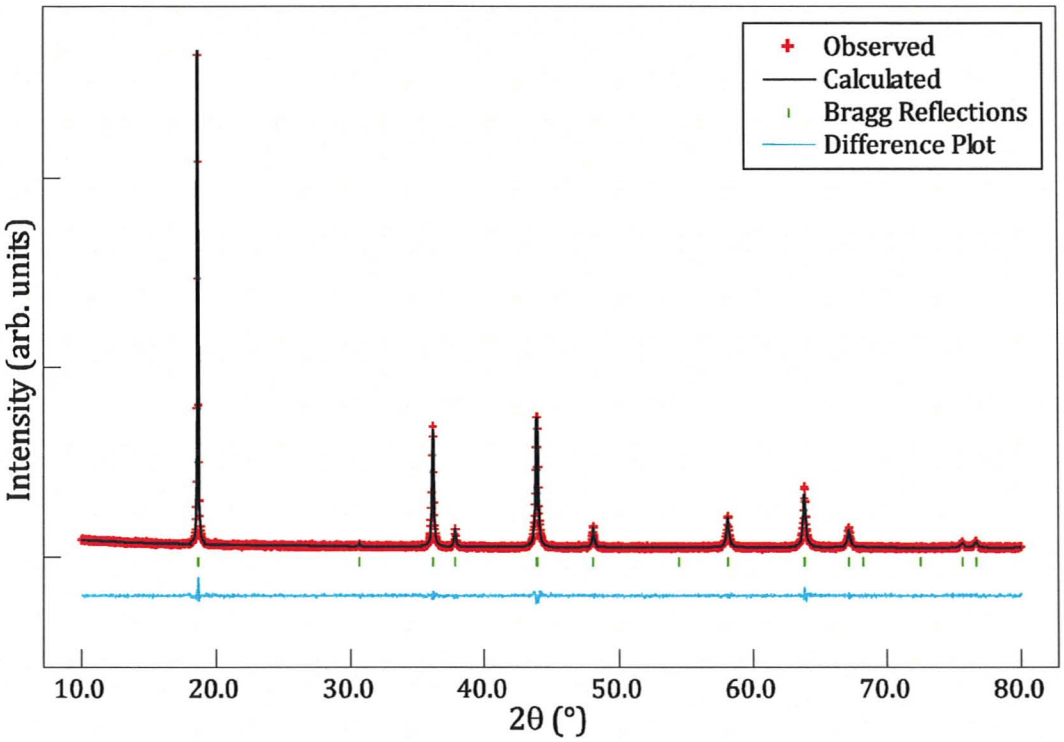

Figure 3-1. X-ray diffraction pattern and Rietveld refinement for Sample 4. Crystallographic data are recorded in Tables 3-3 to 3-5.

All chimie douce syntheses had at least one impurity phase present, though many could not be identified. In particular Sample 7 shows several unidentified peaks (2θ ~11-13°, 21.5°, 22.5°, 23.5°, 25°, 27°, 32.5°) and at least one broad low intensity feature (2θ ~28-32°, potentially also 15°, 41-43°, 54-56°, see Figure A-6). The broad features were initially attributed to sample degradation due to contact with water. Sample 8 also showed the unattributed cluster of peaks around 2θ ~ 11-13° in addition to impurity phases LiV_2O_5 and Li_3VO_4 (Figure A-7). Inclusion of the latter phase did not result in any significant improvement in the Rietveld refinement of. Samples 9, 10, and 13 all contain varying amounts of the starting material $LiVO_2$, while Samples 10 and 13 also show evidence of V_2O_3 formation. High intensity signals for several impurities phases were evident for both Samples 11 and 12, the latter of which LiV_2O_4 is clearly a minor phase.

Magnetic Data

Experimental parameters and magnetic susceptibility data derived by fitting the data to a Curie-Weiss law for the relevant samples are shown in Figures 3-2 to 3-6 and summarized in Table 3-6. All of the susceptibility plots show overlapping ZFC and FC curves down to the lowest temperature measured and exhibit paramagnetic behaviour down to at least ~30 K. The expected broad maximum at ~16 K is only really evident for Samples 2 and 4, although it is still largely masked by a small Curie tail in both curves (Figures 3-2 and 3-4). In contrast, the feature is completely concealed by much larger Curie tails for the remaining samples. This

feature indicates some short range ordering occurs around 16 K. No long range magnetic ordering has previously been reported down to 2 K for LiV_2O_4 [28] and the current study is no exception, although the Curie tails do prevent elucidation of magnetic behaviour in the lowest temperature region.

The mixed 3+/4+ oxidation state of the vanadium ions results in magnetic spins of $S = ½$ and $S = 1$ for the respective valencies. Using the spin only approximation the Curie constant would be expected to fall between $C = 0.375$ and 1.00 emu·K/mol V. The literature provides a more narrow range from $C = 0.35$ [36] to 0.535 emu·K/mol V [28] which most of the current samples fall into. This system is normally interpreted as a $S = ½$ system with a slightly enlarged Landé factor of $g \approx 2.0$ to 2.4, indicating the angular orbital momentum contribution L is not completely quenched. The remaining half electron per vanadium ion primarily participates in electronic conduction.

The exception to this trend is Sample 2, which has a much smaller C than has been reported previously. This may be related to the relatively small lattice parameter observed for this sample; however, an oxygen deficient lattice would result in a decreased valency for vanadium, and thus a spin system that is closer to $S = 1$ than $S = ½$, i.e. a larger Curie constant would be expected rather than a smaller one. Conversely, if the smaller lattice parameter is due to a deficiency of lithium, which would be lost by be evaporation during the sintering process, a higher vanadium valency would result, resulting in a lower value for C. Even taking these

Table 3-6. Experimental and magnetic parameters for Curie-Weiss magnetic susceptibility for Samples 2, 4, 5, 9, and 10. The Applied Field is the magnetic field applied to the samples. C is the Curie constant, θ is the Weiss temperature, and χ_0 is the temperature independent term. The error in the last digit is given in parentheses.

Sample	Applied Field (Oe)	C (emu·K·mol^{-1} V)	θ (K)	$\chi_0 \times 10^{-5}$ (emu·mol^{-1} LiV_2O_4)
2	100	0.150(2)	-29(1)	7.0(9)
4	100	0.429(6)	-36(2)	22(3)
5	500	0.398(3)	-32.5(8)	11(1)
9	100	0.405(5)	-26(1)	22(2)
10	500	0.374(3)	-24.7(7)	76(1)

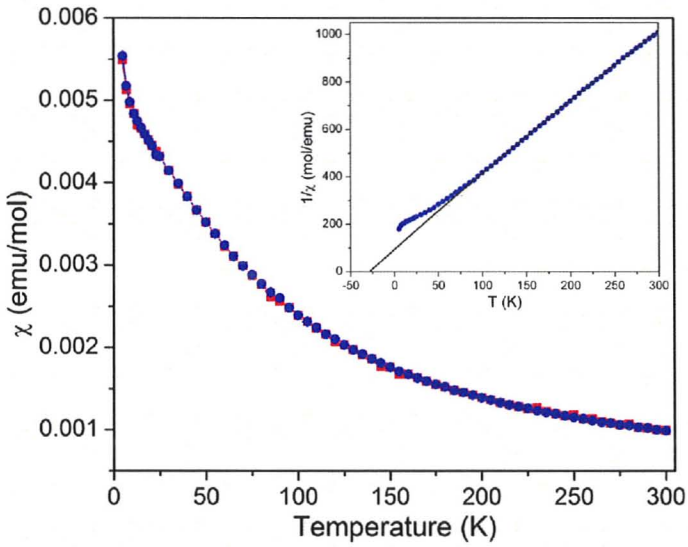

Figure 3-2. Magnetic susceptibility vs. temperature plot for LiV_2O_4 Sample 2. Red squares are ZFC data, blue circles are FC. Inset: Inverse FC susceptibility plot with Curie-Weiss fit. The intercept of the T axis represents the Weiss temperature θ.

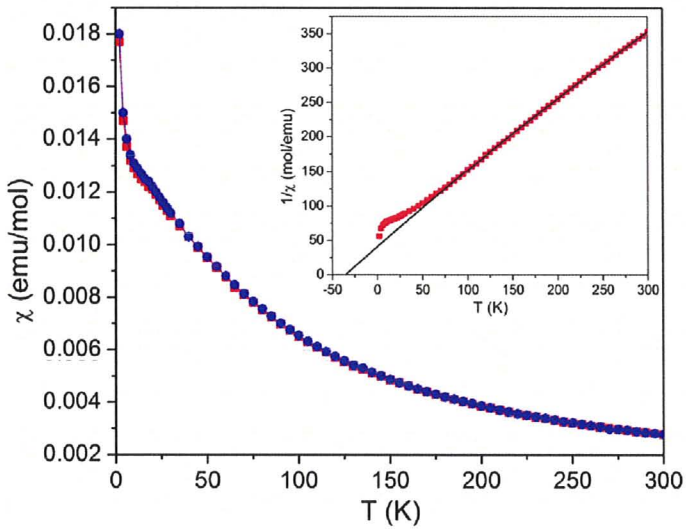

Figure 3-3. Magnetic susceptibility vs. temperature plot for LiV_2O_4 Sample 4. Red squares are ZFC data, blue ccircles are FC. Inset: Inverse ZFC susceptibility plot with Curie-Weiss fit. The intercept of the T axis represents the Weiss temperature θ.

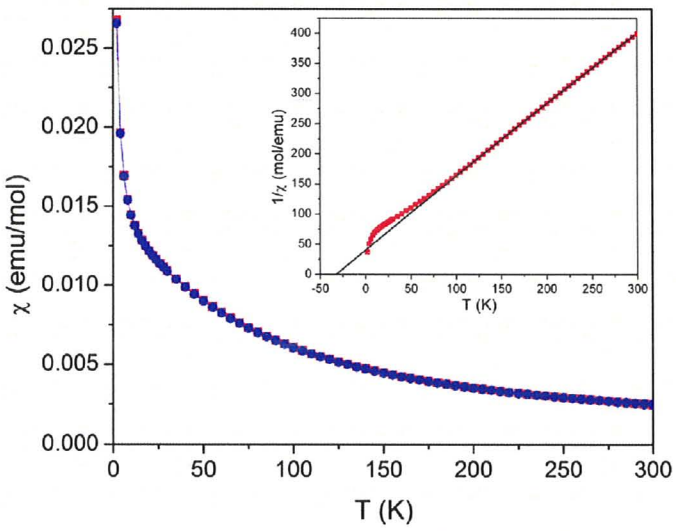

Figure 3-4. Magnetic susceptibility vs. temperature plot for LiV_2O_4 Sample 5. Red squares are ZFC data, blue circles are FC. Inset: Inverse ZFC susceptibility plot with Curie-Weiss fit. The intercept of the T axis represents the Weiss temperature θ.

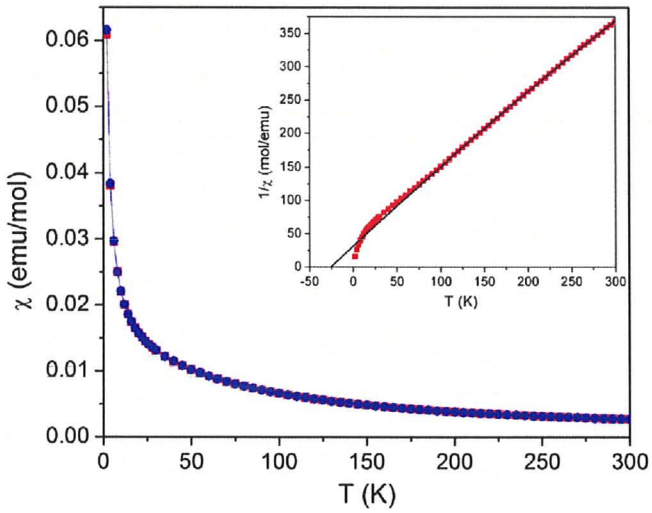

Figure 3-5. Magnetic susceptibility vs. temperature plot for LiV_2O_4 Sample 9. Red squares are ZFC data, blue circles are FC. Inset: Inverse ZFC susceptibility plot with Curie-Weiss fit. The intercept of the T axis represents the Weiss temperature θ.

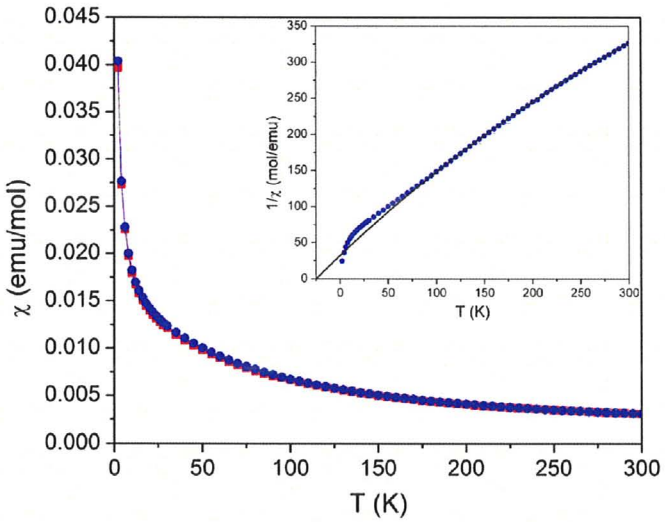

Figure 3-6. Magnetic susceptibility vs. temperature plot for LiV_2O_4 Sample 10. Red squares are ZFC data, blue circles are FC. Inset: Inverse FC susceptibility plot with Curie-Weiss fit. The intercept of the T axis represents the Weiss temperature θ.

explanations into consideration the Curie constant obtained for Sample 2 falls well below the expected value.

The inverse ZFC susceptibility curve of Sample 10 (not shown) reveals a kink at ~230 K that is nearly imperceptible in the normal susceptibility data. The origin of the kink is unknown, but may be related to the contribution of a small amount of V_2O_3 impurity, which undergoes a metal-insulator transition around 150 K [58, 59]; however, this transition temperature does not correspond to the observed temperature of the kink at 230 K, suggesting that other unknown factors are more likely at play.

The Weiss temperature θ is consistent in all cases with that found in the literature. Since no long range ordering occurs, the short range magnetic ordering around 16 K can be taken as the magnetic transition temperature T_N. The resulting degree of frustration seems to indicate a normal θ value for an antiferromagnetic material, ranging from $|\theta|/T_N = 2.4$ for Sample 9 to $|\theta|/T_N = 3.6$ for Sample 10. Nonetheless, the absence of long range order is a strong indicator of the presence of frustration.

3.1.4 Discussion

Evaluation of Synthetic Techniques

Since the ultimate goal of this research project was to study the structural and magnetic properties of the fully lithiated form of LiV_2O_4, a synthesis that could reliably produce a structurally and magnetically pure parent product was desired.

In addition, a small particle size is needed in order to allow the lithium to penetrate to the centre the LiV_2O_4 particles and to prevent kinetic hindrance by adsorption of lithium-organic byproducts by increasing surface area. Furthermore, shorter reaction times are always a desirable trait when considering synthetic processes.

One problem inherent to all the ceramic syntheses in this study is the volatility of lithium oxide, Li_2O, at higher temperatures, particularly in the process of forming the lithium vanadate precursor compounds. Typically, a 5 % molar excess of Li_2CO_3 was employed to account for this loss which may result in an off-stoichiometric product depending on the degree of Li_2O evaporation in a particular reaction. All samples were affected by this to some extent, as even the chimie douce methods rely on lithium vanadate precursors formed by solid state reactions. However, this concern is doubled for the purely ceramic methods due to the chance of further lithium evaporation during the sintering process. Care must be taken to ensure that the platinum crucible is sealed and that the silica tube is evacuated sufficiently such that no atmospheric oxygen remains that can react with the starting materials in the pellets. Additionally, the temperature must be kept low enough to prevent Li_2O evaporation, resulting in relatively long reaction times.

The reaction of $LiVO_3$ with VO used for Samples 1 and 2 results in a crystallographically pure product, although the relatively large noise level inherent in the use of the photographic film-based Guinier-Hägg camera may conceal some minor impurity phases. The main difficulty with this method comes from the use of typically non-stoichiometric vanadium (II) oxide which exists in a composition

range as VO_x ($0.85 \leq x \leq 1.10$). This can lead to uncertainty in the oxygen content of the LiV_2O_4 product, requiring more complicated reaction conditions to account for the oxygen deficiency or excess. The need for this is best shown by the results of Sample 2, which not only had a much smaller unit cell than the other LiV_2O_4 species but also had a significantly reduced Curie constant in the magnetic susceptibility data.

Both the reaction of Li_3VO_4, V_2O_3, and VO_2 and that of $LiVO_2$, V_2O_3, and V_2O_5, represented by Samples 3 and 6, respectively, were incomplete after a total sintering time of nearly four weeks each, as evidenced by the presence of impurity phases in the powder patterns of both samples. For Sample 6, the impurity phases made up an estimated total of 6.5 % of the molar quantity in the powder examined. While this is a fairly small quantity, it is still far larger than the amount detectable in the remaining samples produced by ceramic methods.

Samples 4 and 5, which were produced by heating pellets of "$Li_2VO_{3.5}$" and V_2O_3, each resulted in powder diffraction patterns that were essentially free of impurity phases. ICP-OES results indicate a slight lithium deficiency for Sample 4 and a slight excess for Sample 5. The magnetic data for both samples fit well with what has been reported before, although Sample 5 shows a much more significant Curie tail, which has been discussed previously. Slight differences in the synthetic procedures may be responsible for the increased amount of magnetic impurity, and further studies need to be performed to determine whether the magnitude of the Curie tail can be controlled.

The presence of impurity phases in all chimie douce syntheses suggests the methods used were not optimal for producing pure LiV_2O_4. Two samples, #7 and #8, show a cluster of impurity peaks at low angle, indicative of a large unit cell, but no phase has been identified which can explain the presence of these peaks. All other samples contain identifiable impurity phases. While in some cases reaction to the spinel may be progressed by sintering the products at higher temperatures, this defeats the purpose of using chimie douce methods to produce LiV_2O_4. Not only would there be significant uncertainty in the stoichiometry of the reactants, but the total reaction time would begin to approach that required for ceramic syntheses and the risk of losing Li_2O is again reintroduced.

The focus of the chimie douce inquiry was the novel method involving I_2 (g) as the delithiating agent, which resulted in a wide variation in phase purity with only slight variations in reaction procedure. For example, while Sample 9 was nearly phase pure, LiV_2O_4 was not even the major phase in Sample 12. The problem of impurity phases was exacerbated by incomplete reaction of I_2 (g), as evidenced both by the persistence of $LiVO_2$ in most samples and the remainder of unreacted iodine for even stoichiometric reactions. Because of this, the degree of lithiation cannot be directly determined from the ratio of the reactants and some excess amount of I_2 must be added each time. Despite this by comparing Samples 9 and 10 it can be seen that even when I_2 is in excess some side reactions can occur, producing a fully delithiated product V_2O_3 while leaving some of the starting material $LiVO_2$. The fact that this full delithiation maintains the V^{3+} oxidation state

as the expected delithiation product, VO_2, would involve the oxidation of vanadium from 3+ to 4+. This shows that evaporation of Li_2O can be a problem even for chimie douce reactions. Further study on this reaction method would be needed to understand all the interactions going on inside the reaction vessel.

The exceptionally large Curie tails in evidence from the magnetic susceptibility data for Samples 9 and 10 demonstrate that LiV_2O_4 produced by the gaseous I_2 delithiation process is prone to magnetic impurities in addition to chemical ones, as the low temperature upturns are most likely due to paramagnetic site defects in the spinel lattice [28]. While Curie tails were also observed for all ceramic samples for which magnetic susceptibility data were collected, those seen for the chimie douce synthesis tended to be much larger, completely masking the broad peak around 16 K. As with chemical defects, it may be possible to reduce the Curie tails by refining the synthetic process; however, with other methods already available that can reliably reproduce the desired chemical and magnetic properties there seems little reason to continue improving this method of LiV_2O_4 synthesis.

Iodine was also found to be a poor delithiating agent when dissolved in an organic solvent, contrasting strongly with the efficacy of Br_2 to accomplish the same feat [7, 60]. While the I_2 dissolved in chloroform did succeed in removing some lithium from the spinel lattice, a significant amount of $LiVO_2$, ~15 % by mol, did not appear to react at all even after nearly two weeks of stirring, while the impurity V_2O_3 made up another 11 % of the molar composition in the powdered sample.

3.2 $Li_2V_2O_4$

3.2.1 Background

$Li_2V_2O_4$ has an ordered rock salt structure where both the vanadium and lithium ions form distinct but interlocking pyrochlore sublattices with other cations of the same element. It is a metastable phase reportedly transforming to layered $LiVO_2$ above 500 °C in argon atmosphere [61]. It can therefore only be synthesized by chimie douce or electrochemical methods using LiV_2O_4 spinel as the starting material [7, 60]. Lithiation to $Li_{1+x}V_2O_4$ occurs via a two-step process [7]. First, the inserted lithium occupies one-half of the hitherto empty 16*c* octahedral sites in the $Fd\bar{3}m$ unit cell without disturbing the lithium ions on the tetrahedral 8*a* sites. Around the composition $x = 0.5$ the remaining A-site cations begin to migrate into the octahedral holes until at $x = 1.0$ the 16*c* sites are completely filled and the 8*a* sites are empty. As a result, the lattice parameter does not increase according to Végard's law upon lithiation but rather is described by two curves from $0 \leq x \leq 0.4$ and $0.6 \leq x \leq 1.0$ with an approximately linear region in the middle [60]. Chemical lithiation is limited by electrostatic interactions to a maximum composition of $x = 1.0$ [7], although electrochemical insertion can push the value as high as $x = 1.5$, which results in the break-up of the spinel-like sub-structure [62].

The study of $Li_2V_2O_4$ has primarily been focused on its electrochemical properties in relation to the use of LiV_2O_4 as a positive electrode in lithium ion batteries [7, 52, 61-63]. Open circuit voltage measurements reflect the lithium

insertion scheme outlined above, with a gradual decrease in voltage observed above $x \approx 0.45$ for the cell construction Li/1 M $LiClO_4$ in propylene carbonate/$Li_{0.94+x}V_2O_4$ [7]. A later study using $LiBF_4$ at the anode reports a sharp drop in voltage at $x \approx 0.4$ followed by a linear decrease in voltage to $x = 1.0$, a difference attributed to a more careful handling of the starting materials [60]. Electrical conductivity measurements show it is semiconducting with σ on the order of $10^{-6}\ \Omega^{-1}cm^{-1}$ with a significantly enhanced Li^+ diffusion rate compared to LiV_2O_4 at room temperature [63]. Cyclic voltametry between the compositions LiV_2O_4 and $Li_2V_2O_4$ shows continued cyclability above 100 cycles.

The rest of section 3.2 is devoted to the current study of lithium insertion into LiV_2O_4 to form $Li_2V_2O_4$. Sample preparation and structural composition are examined giving attention to the role of particle size in lithiating the spinel phase. Magnetic susceptibility data on several samples are presented for the first time with some anomalous results.

3.2.2 Experimental

For labeling purposes, the Samples of $Li_2V_2O_4$ are given alphanumeric codes wherein the first digit corresponds to the sample number of the LiV_2O_4 specimen used to synthesize the lithiated compound, and the second digit distinguishes between different lithiation trials.

Sample Preparation

Polycrystalline samples of $Li_2V_2O_4$ were prepared by chimie douce reaction of prepared LiV_2O_4 with n-butyllithium (*n*-BuLi) in hexane. For each reaction a three- to fourfold excess of *n*-BuLi (2.0 M, Sigma-Aldrich or 2.7 M, Alfa Aesar) in hexane was diluted to ~0.5 M with sodium-dried hexane and stirred with LiV_2O_4 powder in a N_2 atmosphere for 5 to 10 days at ambient temperature. The exception to this procedure was Sample 5B, which was reacted with undiluted 2.7 M *n*-BuLi for seven days followed by a second reaction in diluted *n*-BuLi for six days. When the reaction was completed, the products were allowed to settle, the liquid phase decanted using positive pressure dynamic vacuum, and the powder washed three times with sodium-dried hexanes before being dried by vacuum. For Sample 4B the LiV_2O_4 precursor Sample 4 was ball-milled for three days prior the lithiation reaction in order to decrease particle size and hence increase lithiation.

One attempt, Sample 5A, was made to lithiate LiV_2O_4 using lithium metal dissolved in liquid ammonia, NH_3. Powder of the spinel was added to an excess of Li metal dissolved in liquid NH_3, kept at -78 °C in an acetone-dry ice bath. The setup was left to sit for several hours after which the ammonia was decanted from the solid and any remaining lithium metal deactivated by washing with ethanol three times.

Powder X-ray Diffraction

X-ray diffraction patterns of the powdered samples were collected using a PANalytical X'Pert PRO diffractometer with a Cu $K\alpha_1$ radiation source using the same methods and parameters as described in §3.1.2. The program EVA was used to identify both major and minor phases, and Rietveld data refinement was accomplished using the GSAS-EXPGUI suite of programs [55, 56]. Molar percentages of impurity phases were established by converting the weight fractions found by the Hill and Howard method described previously [57].

Structural determination of Sample 2A was performed using a Guinier-Hägg camera with a monochromated Cu $K\alpha_1$ radiation source and using elemental silicon powder as an internal standard, the peaks for which are indicated with an asterisk (*) in the diffraction pattern. The data were processed according to the procedures laid out in §3.1.2.

ICP-OES

ICP-OES measurements were performed on Samples 4A, 4B, 5B, and 9A according to the method described in §3.1.2.

Magnetic Measurements

Magnetic measurements were performed on Samples 4A, 4B, 5B, and 9A using a Quantum Design MPMS SQUID magnetometer. Measurements performed §3.1.2. High temperature data (320-600 K) were collected using an oven insert with

quartz sample holders. The applied magnetic field was 100 Oe for the low temperature Sample 9A data set and 500 Oe for each other data set.

3.2.3 Results and Discussion

Structural Characterization

The powder x-ray diffraction patterns for all samples of $Li_2V_2O_4$ are shown in Figures 3-7 to 3-12. Lattice parameter *a*, oxygen parameter *u*, Rietveld refinement parameters, and molar percent of LiV_2O_4 impurity are recorded in Table 3-7. Selected interatomic distances and bond angles for Sample 4B are recorded in Tables 3-8 and 3-9, respectively.

For Sample 2A LiV_2O_4 spinel remains the major phase. Only a small amount of lithiation was achieved in this reaction as indicated by the slight increase in unit cell volume (~ 0.14 %) over the parent specimen and the small shoulders that have emerged at the lower angle edge of the LiV_2O_4 peaks.

Sample 5A, which was reacted with lithium metal dissolved in liquid NH_3, did not appear to undergo any lithiation at all. The only phase present is the spinel LiV_2O_4, with no evidence that any lithiation might have occurred such as the lower angle shoulders observed for Sample 2A. The unit cell obtained by Rietveld refinement is paradoxically smaller than that found for the parent Sample 5 spinel, perhaps indicating that a small amount of vanadium reduction was achieved by removal of oxygen atoms rather than by insertion of lithium.

Table 3-7. Lattice parameter a and oxygen coordinate u for $Li_2V_2O_4$, molar percent and lattice parameter a for LiV_2O_4 where applicable, and Rietveld agreement factors for all lithiation attempts.

Sample	a (Å)	u (fractional coordinate)	Molar % LiV_2O_4	a (Å) of LiV_2O_4	R_p	R_{wp}	χ^2
2A	N/A	N/A	Major Phase	8.237(11)	N/A	N/A	N/A
4A	8.29825(4)	0.2541(2)	25.5	8.2516(2)	0.0801	0.1020	1.26
4B	8.29567(4)	0.2563(1)	0.0	N/A	0.0452	0.0594	1.91
5A	N/A		Major Phase	8.2460(2)	0.0860	0.1112	1.42
5B: #1	8.29722(5)	0.2598(2)	47.0	8.25068(5)	0.0585	0.0788	2.48
#2	8.29803(4)	0.2550(2)	26.3	8.2570(1)	0.0740	0.0961	1.68
9A	8.29475(3)	0.2531(1)	22.6	8.2490(2)	0.0530	0.0698	2.24

Table 3-8. Selected interatomic distances for Sample 4A.

Atoms	Distance (Å)
Li – O	2.127(1)
V – O	2.0231(9)
Li – Li	2.93296(1)
Li – V	2.93296(1)
V – V	2.93296(1)

Table 3-9. Selected bond angles for Sample 4A.

Atoms	Angle (°)
O – Li – O	87.22(5)
O – Li – O	92.78(5)
O – V – O	87.01(6)
O – V – O	92.99(6)
Li – O – Li	87.15(5)
Li – O – V	89.891(4)
Li – O – V	175.92(7)
V – O – V	92.92(5)

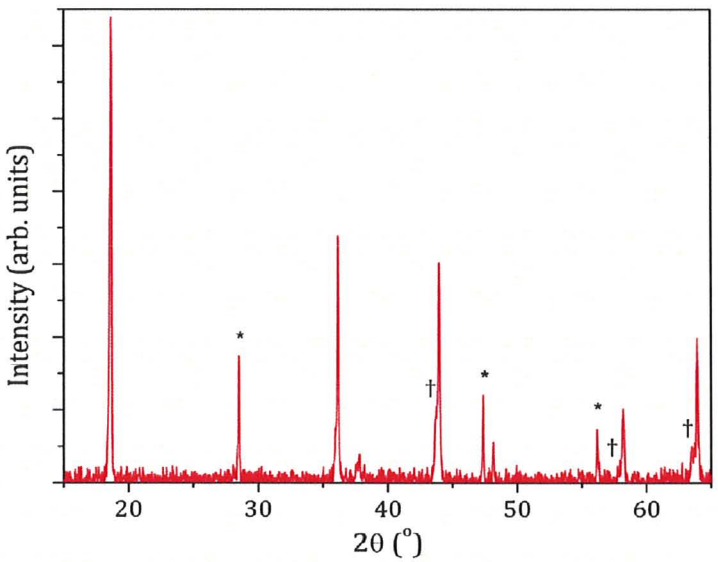

Figure 3-7. Powder x-ray diffraction pattern for Sample 2A. The most visible $Li_2V_2O_4$ peaks appear as slightly lower angle shoulders to the main LiV_2O_4 peaks and are denoted by (†). Silicon peaks are labeled with an asterisk (*).

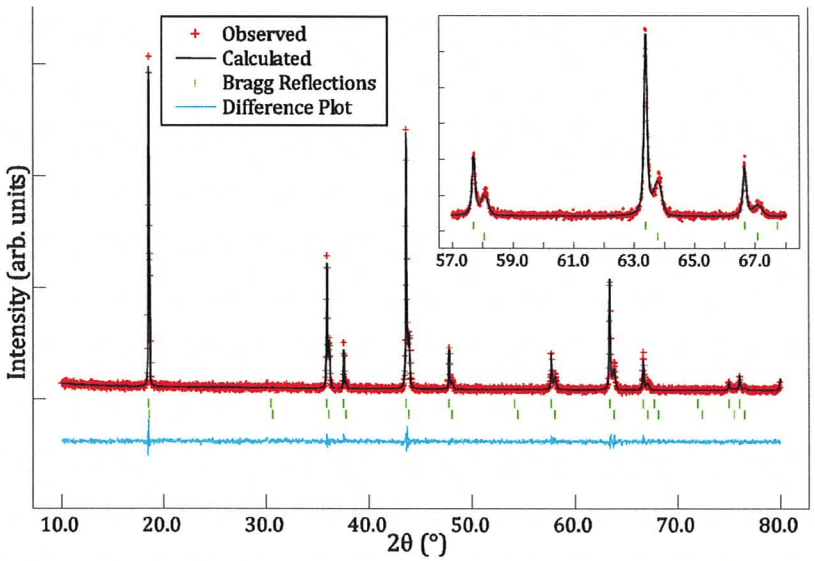

Figure 3-8. Powder x-ray diffraction pattern for Sample 4A, with Rietveld refinement and difference map, and Bragg reflections (top: $Li_2V_2O_4$ lithiated rock salt; bottom: LiV_2O_4 spinel). Inset: Enlargement of range 57° to 68° showing separation of Bragg peaks for LiV_2O_4 and $Li_2V_2O_4$.

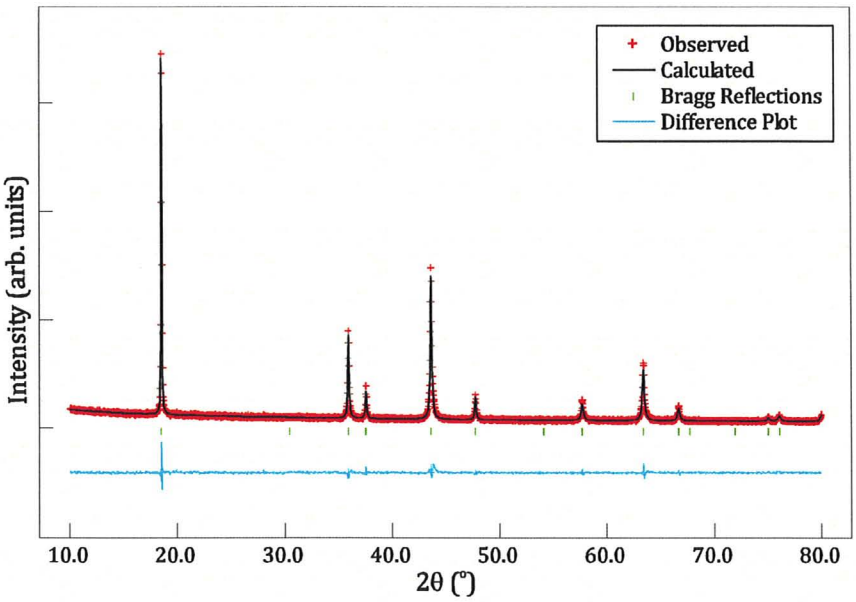

Figure 3-9. Powder x-ray diffraction pattern for Sample 4B, along with Rietveld refinement, difference map, and Bragg reflections for $Li_2V_2O_4$ lithiated rock salt.

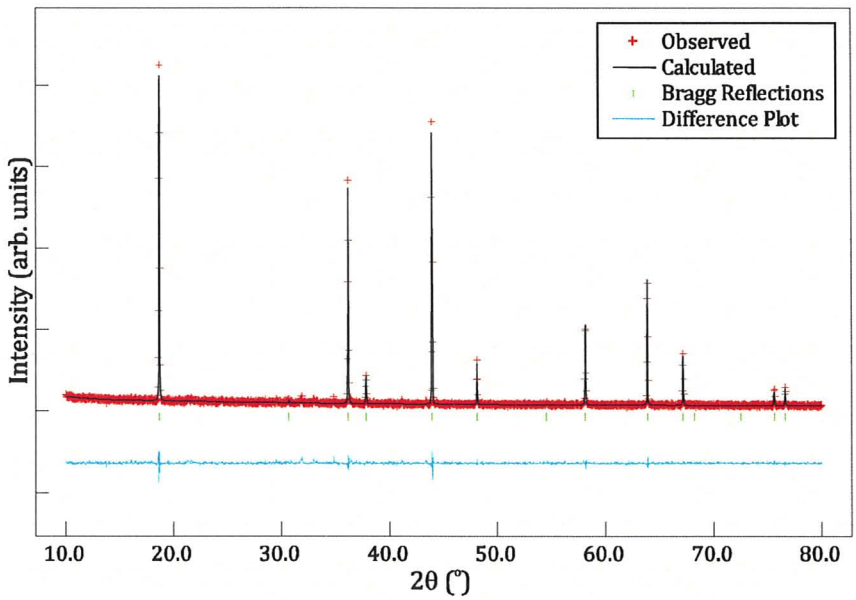

Figure 3-10. Powder x-ray diffraction pattern for Sample 5A, along with Rietveld refinement, difference map, and Bragg reflections for LiV_2O_4 spinel.

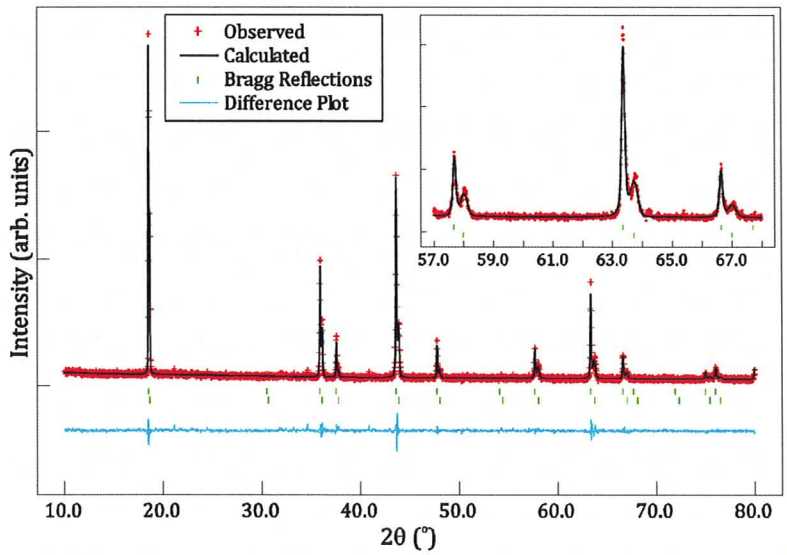

Figure 3-11. Powder x-ray diffraction pattern for Sample 5B following the second lithiation, with Rietveld refinement, difference map, and Bragg reflections (top: $Li_2V_2O_4$ lithiated rock salt; bottom: LiV_2O_4 spinel). Inset: Enlargement of range 57° to 68° showing separation of Bragg peaks for LiV_2O_4 and $Li_2V_2O_4$.

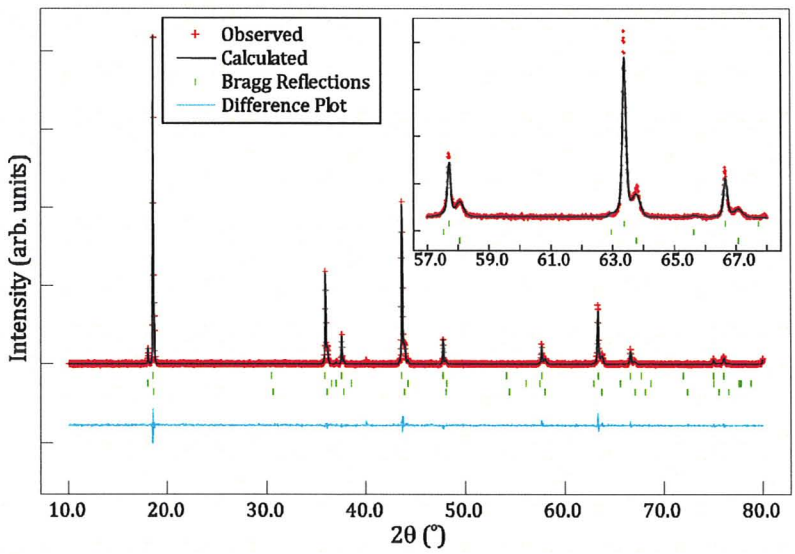

Figure 3-12. Powder x-ray diffraction pattern for Sample 9A, with Rietveld refinement, difference map, and Bragg reflections (top: $Li_2V_2O_4$ lithiated rock salt; middle: $LiVO_2$ layered rock salt; bottom: LiV_2O_4 spinel). Inset: Enlargement of range 57° to 68° showing separation of Bragg peaks for LiV_2O_4 and $Li_2V_2O_4$.

The $Li_2V_2O_4$ lattice parameter *a* determined for Samples 4A, 4B, 5B and 9A is slightly larger than that reported in the literature (*a* = 8.291(1) Å [7]). Of these, only Sample 4B reached 100 % lithiation due to the smaller particles, and therefore greater surface area, formed through the process of ball-milling. This decrease in particle size was confirmed by the systematic line-broadening in the powder x-ray diffraction peaks of LiV_2O_4 in Sample 4. For the remaining, unmilled samples an average lithiation of ~75 % was achieved when reacted with diluted *n*-BuLi. Note that Sample 9A retained a small amount of $LiVO_2$ (~1.5 %), an impurity also found in the parent sample.

It is likely that the residual spinel phase in Samples 2A, 4A, 5B, and 9A underwent partial lithiation since in all cases a small increase in the unit cell volume for LiV_2O_4 compared to the cell volume of the initial sample was observed. The unit cell expanded by 0.35 % for the second lithiation of 5B, but by less than 0.25 % for each other sample. These values are small compared to the approximately 1.8 % cell volume increase for the fully lithiated $Li_2V_2O_4$. According to measurements performed by Manthiram and Goodenough [60] a cell increase of 0.35 % would correspond to approximately 25 % lithiation.

Sample 5B underwent two separate lithiation reactions, first using a large excess of 2.7 M *n*-BuLi, followed by a second reaction with excess *n*-BuLi diluted to ~0.5 M. As can be seen from Table 3-4, the first reaction lithiated 53.0 % of the sample to $Li_2V_2O_4$ while leaving the remainder as the spinel. The second lithiation reaction resulted in an additional 20 % of the sample being lithiated. An explan-

ation for this involves the adsorption of amorphous lithium-organic species to the surface of the particles, hindering the rate of lithium insertion. In concentrated *n*-BuLi adsorption would happen quickly making it difficult for other *n*-BuLi molecules to reach the surface in order to lithiate the particle. Conversely, some of the adsorbed phase would be washed away during the quenching of the initial reaction as well as during stirring of the second reaction mixture, opening new sites where *n*-BuLi can react with the particle. The upper limit reached during the second lithiation of Sample 5B is more likely a consequence of particle size rather than the adsorbed phases, as a similar limit in the degree of lithium insertion was also reached for Samples 4A and 9A.

The adsorbed lithium-organic phase explanation is corroborated by the presence of a whitish powder that was frequently observed along with the black $Li_2V_2O_4$ product. This powder could not be washed away by either hexane or methanol and the lack of discernable peaks in the x-ray pattern suggests that is constitutes an amorphous phase.

ICP-OES measurements consistently gave higher than expected molar ratios for Li:V as well as predicting oxygen contents that were more than twice those expected. Part of the discrepancy in the Li:V ratio may be attributed to partial lithiation of the LiV_2O_4 as mentioned above, but this does not account for all of lithium content observed. The main source of this augmentation appears to be the presence of adsorbed lithium-organic phases mentioned above. The ICP-OES instrument used is unable to detect oxygen directly so the sample weight

corresponding to oxygen content is determined by subtracting the weight of lithium and vanadium from the total weight of the sample. Since the instrument is also unable to detect either carbon or hydrogen, any organic phase present would be included as part of the oxygen weight, augmenting the calculated oxygen content. The oxygen content determined by this method was consistently ~2 to 2.3 times larger than is expected based on the vanadium content, confirmation that additional chemical species is present in the samples which are most likely organic in nature. Since the lithium content is higher than expected, it can be deduced that lithium also constitutes a portion of these adsorbed organic phases. As a consequence, ICP-OES did not prove to be a very useful characterization technique for $Li_2V_2O_4$.

Magnetic Data

Magnetic susceptibility data for Samples 4A, 4B, 5B, and 9A are shown in Figures 3-13 to 3-16. Curie-Weiss fits for all samples resulted in excessively large values for C, suggesting that the paramagnetic temperature range does not begin below 600 K. Enormous values were also determined for θ. Both of these observations point toward the absence of a true Curie-Weiss domain below 600 K, an indication of a strongly geometrically frustrated system.

The shape of the magnetic susceptibility curve is highly sample dependent with the largest similarities evident between Samples 4A and 4B, demonstrating the role played by the magnetism of the parent sample. One feature common to all four

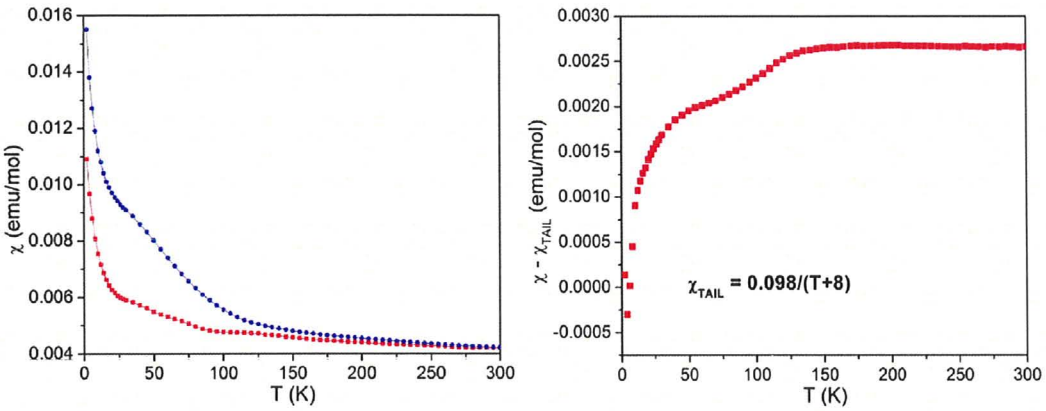

Figure 3-13. Left: Magnetic susceptibility vs. temperature plot for $Li_2V_2O_4$ Sample 4A from 2 to 300 K. Red curve is ZFC, blue curve FC. Right: ZFC susceptibility with the Curie tail contribution subtracted. The C-W law for the Curie tail is shown on the plot.

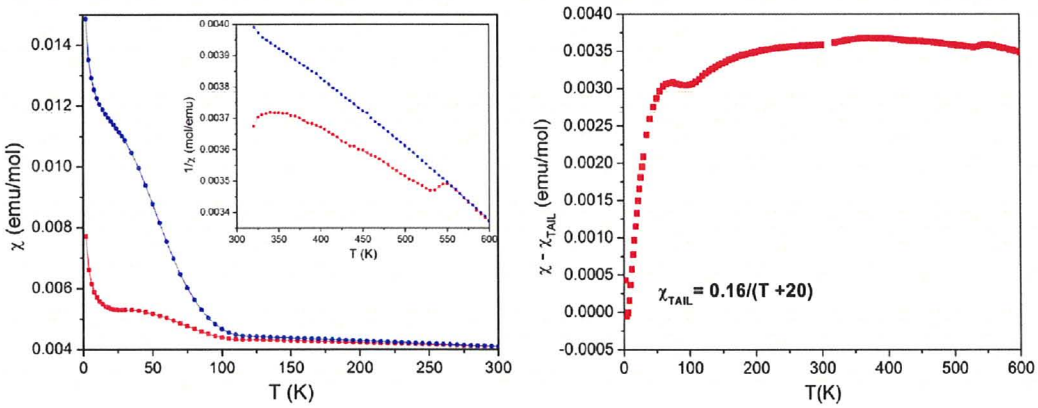

Figure 3-14. Left: Magnetic susceptibility vs. temperature plot for $Li_2V_2O_4$ Sample 4B from 2 to 300 K (main graph) and from 320 to 600 K (inset). Red curves are ZFC, blue curves are FC. Right: ZFC susceptibility with the Curie tail contribution subtracted. The C-W law for the Curie tail is shown on the plot.

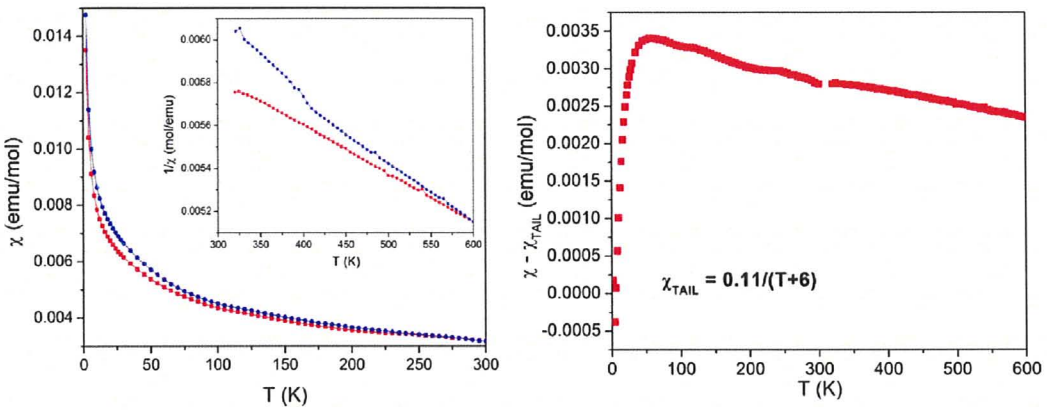

Figure 3-15. Left: Magnetic susceptibility vs. temperature plot for $Li_2V_2O_4$ Sample 5B from 2 to 300 K (main graph) and from 320 to 600 K (inset). Red curves are ZFC, blue curves are FC. Right: ZFC susceptibility with the Curie tail contribution subtracted. The C-W law for the Curie tail is shown on the plot.

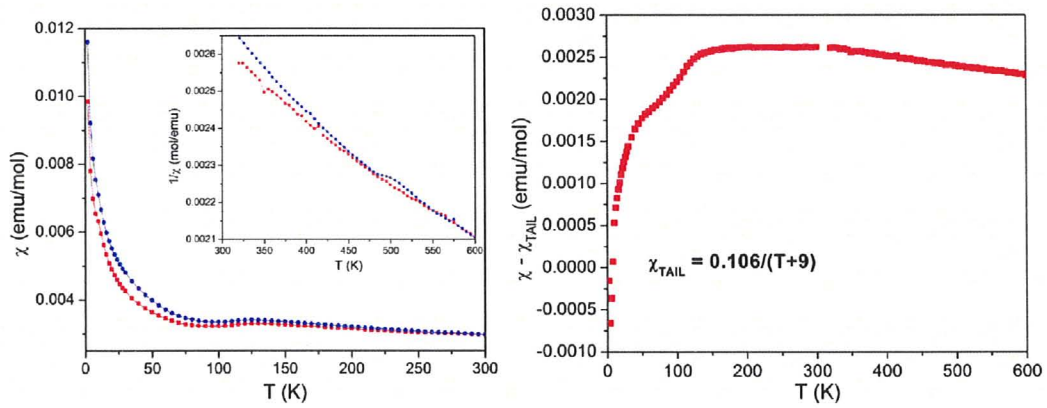

Figure 3-16. Left: Magnetic susceptibility vs. temperature plot for $Li_2V_2O_4$ Sample 9A from 2 to 300 K (main graph) and from 320 to 600 K (inset). Red curves are ZFC, blue curves are FC. Right: ZFC susceptibility with the Curie tail contribution subtracted. The C-W law for the Curie tail is shown on the plot.

curves is a broad, shallow maximum at ~130 K. The trait is difficult to discern in most of the samples but can be distinguished by fitting the Curie tails of each sample to a Curie-Weiss law and subtracting this contribution from the ZFC magnetic susceptibility plots (Figures 3-13 to 3-16, right-hand plots). This also reveals a feature at ~ 50 K which is probably related to the broad feature visible in the unmodified ZFC and FC susceptibility data for Samples 4A and 4B at ~ 35 K.

Divergence between ZFC and FC susceptibility curves is an indication of the onset of magnetic spin interactions in a solid, i.e. that the region lies outside the paramagnetic range, even if no explicit spin ordering has occurred. When cooled in the presence of a magnetic field, the spins align with the field resulting in a larger magnetic susceptibility response than the same sample cooled in the absence of a magnetic field. This does not occur for every compound, as can be seen with the χ vs. T plots for LiV_2O_4 spinel in §3.1.3; however, all samples of the ordered rock salt $Li_2V_2O_4$ shows some divergence between the ZFC and FC curves. Careful inspection of the low temperature susceptibility plots seems to indicate the divergence begins below ~230 to 260 K, although the separation is slight until ~100 K. The heating and cooling curves above 320 K also fail to overlap for most of the data range, although some overlap is seen above 550 K for Sample 4B and 9A. This observation may help explain why no Curie-Weiss region was determined.

The higher temperature heating and cooling curves show the same sample dependence seen for the low temperature ZFC and FC curves. Samples 5B and 9A both show features in the cooling curves at ~395 K and ~500 K, respectively,

though oddly no reciprocal features are evident in the heating curves as would be expected. The feature in Sample 5B also more closely resembles ferromagnetic than antiferromagnetic ordering. The origin of these features is not clear, since any feature in the cooling curve would be expected show up in the heating curve as well, while the reverse is not necessarily true.

The heating curve of Sample 4B shows two pronounced maxima at ~340 K and ~550 K. Neither of these are observed in the other plots, although a small upturn between 320 and 325 K for both Samples 5B and 9A may be related to the ~340 K maximum of Sample 4B. This could indicate that some short range ordering develops in the 20 K gap between the low temperature and high temperature data sets; however, the data at the cusp of this gap is too slight to be able to form any conclusive interpretations. Further magnetic susceptibility studies with overlapping LT and HT data would be needed to fill in the gap and clarify this feature.

3.3 Conclusions

Several different synthetic routes were employed to produce LiV_2O_4 spinel. These were evaluated according to length of reaction time, chemical purity of products, magnetic defect concentration, and reproducibility to find suitable candidates for lithium insertion reactions. Despite some promising developments in the novel chimie douce oxidation of $LiVO_2$ by I_2 (g), the persistence of impurity

phases, inability to reliably replicate results, and high concentration of magnetic defects proved that this synthesis was not ideal for LiV_2O_4 production. By contrast the ceramic reaction of $Li_2VO_{3.5}$ with V_2O_3 produced phase pure samples with relatively few magnetic defects; however, optimization of the synthetic procedure is required to further improve the magnetic purity. The reaction of $LiVO_3$ with VO proved to be problematic due to the uncertainty of oxygen content in the vanadium (II) oxide. All other syntheses showed the presence of impurity phases.

The lithiation of LiV_2O_4 to form $Li_2V_2O_4$ proved to be limited both by the particle size of the spinel and the concentration of *n*-BuLi lithiating agent. The former evidently reduced ion mobility through the spinel structure making it difficult for lithium ions to penetrate to the core of larger particles, while the latter was a problem of kinetic hindrance due to the adsorption of lithium-organic compounds to the particle surface.

The magnetic susceptibility data of $Li_2V_2O_4$ showed strong sample dependence. Common features included broad maxima at ~ 35 to 50 K and ~130 K, divergence between ZFC and FC curves below ~ 100 K and possibly extending up to 600 K, and the complete absence of Curie-Weiss behaviour up to 600 K. These observations all point to a strongly geometrically frustrated d^2 pyrochlore sublattice of the vanadium ions. Further investigation is needed to determine the nature of the frustrated magnetic interactions.

Chapter 4: Synthesis, Structure, and Magnetic Properties of Lithium Titanium Oxide Spinel-Based Systems

4.1 $LiTi_2O_4$ and $Li_2Ti_2O_4$

4.1.2 Background

The lithium titanium spinel series $Li_{1+x}Ti_{2-x}O_4$, $0 \leq x \leq 0.33$, was first discovered by Deschanvres, Raveau and Sekkal in 1971 by solid state reaction of Li_2TiO_3 and TiO_2 in air at 800 °C [64]. Within a decade a new synthesis of the end-member $LiTi_2O_4$ was developed by Murphy *et al.* whereby lithium was topotactically inserted into the anatase polymorph of TiO_2 by chimie douce reaction with *n*-butyllithium (*n*-BuLi) [65] followed by heating above ~ 450 °C for the transition to the spinel [8]. A maximum Li:Ti ratio of 0.5:1 was reached in the lithiated anatase structure when reacted with dilute *n*-BuLi (~0.50 M), though ratios up to 0.7:1 could be reached with higher concentrations (~2.3 M). Particle size has also been established as an important factor on lithium insertion into anatase [66]. The earliest studies determined a lattice parameter of $a \approx 8.39$ Å and oxygen parameter of $u \approx 0.265$ for the 1:2:4 spinel [64, 67]; however, the majority of reports have determined values between 8.40 to 8.41 Å for a and 0.261 to 0.263 for u [68-74]. $LiTi_2O_4$ has been shown to age appreciably in air and moisture, completely losing superconductivity (see below) within 5 days due to a decrease in lithium content [72, 75, 76].

$LiTi_2O_4$ is metallic with a superconducting critical temperature T_c = 10 to 13.7 K, an effect manifested by a sudden drop in the resistivity to ρ = 0 Ω·cm. This is reflected in the magnetic susceptibility by a drop to negative values due to the Meissner effect [67, 71, 74, 75, 77-79]. Above the T_c the magnetic susceptibility of $LiTi_2O_4$ is nearly temperature independent. Several studies have shown the spinel to be a normal type II BCS superconductor with moderate electron-electron correlations [71, 80-83].

Chemical and electrochemical lithium insertion into $LiTi_2O_4$ has been established resulting in an ordered cubic rock salt structure with a = 8.3756(1) Å and u = 0.2552(2) for the end member rock salt $Li_2Ti_2O_4$ [8, 69, 84]. As with other lithium transition metal oxide spinels the lithium ions migrate from the 8*a* tetrahedral sites to the 16*c* octahedral interstices, a process which is calculated to occur beginning at a lithium composition of 1.25 [85]. Murphy *et al.* [8] reported magnetic susceptibility data which could not be fit to a Curie-Weiss law, but which also did not display any distinguishing features.

This chapter deals with the synthesis of $LiTi_2O_4$ and its lithiation reactions. X-ray diffraction and magnetic susceptibility data are examined. The anomalous behaviour of lithium in both the spinel and the rock salt are described and contrasted.

4.1.2 Experimental

Sample Preparation

Polycrystalline samples of $LiTi_2O_4$ (Sample A) were prepared by reaction of anatase-TiO_2 (99 %, BDH) with a two- to fourfold excess of *n*-BuLi in hexane (2.0 M, Sigma-Aldrich or 2.7 M, Alfa Aesar) diluted to ~ 0.5 M according to the reaction procedure described in §3.2.2. White TiO_2 was annealed in air at 500 °C prior to reaction with *n*-BuLi. The resulting black powder was collected in a pyrex or fused silica tube under inert atmosphere, the tube evacuated and sealed and the sample heated to 450 °C for 60 hours for the transition to the dark blue spinel to occur. The air and moisture sensitive products were stored in a nitrogen-filled glove box.

Polycrystalline samples of $Li_2Ti_2O_4$ were prepared by reaction of $LiTi_2O_4$ with *n*-BuLi also using the method described in §3.2.2. The resulting blue-black sample was stored in a nitrogen-filled glove box due to air and moisture sensitivity. Following an initial reaction with n-BuLi (Sample L1), the product was reground in a mortar and pestle for 30 min. before being reacted with *n*-BuLi a second time for three weeks (Sample L2).

Powder X-ray Diffraction

Powder x-ray diffraction patterns were collected using a PANalytical X'Pert Pro diffractometer in the same manner outlined in §3.1.2. Phase identification was performed using EVA and GSAS-EXPGUI was employed for Rietveld refinement [55,

56]. Molar percents of phases in L1 were estimated by converting the weight fractions found using Rietveld scaling factors by the Hill and Howard method [57].

ICP-OES

The relative molar quantities of lithium and titanium were measured by ICP-OES employing the procedure described in §3.1.2. A dilute solution of 2:5:1 HNO_3:H_2SO_4:HF was needed to digest the powders.

Magnetic Measurements

Magnetic susceptibility data were collected using a Quantum Design MPMS SQUID magnetometer in RSO mode with an applied field of 500 Oe. Measurements were collected in 1 K increments from 2 to 20 K and 5 K increments from 25 to 300 K.

4.1.3 Results

Structural Characterization

The x-ray diffraction patterns and Rietveld refinements for Samples A, L1, and L2 are shown in Figures 4-1, 4-2, and 4-3 with the crystallographic results summarized in Table 4-1. Lists of interatomic distances and bond angles are given in Tables 4-2 and 4-3 for $LiTi_2O_4$ based on refinement of Sample A, and in Tables 4-4 and 4-5 for $Li_2Ti_2O_4$ based on two-phase refinement of L1.

Due to difficulties in the refinement of fresh samples, Figure 4-1 was collected about 6 months after the original sample was produced. Two small

Table 4-1. Unit cell parameter a, oxygen position parameter u, and Rietveld refinement factors for Samples A, L1 and L2. For L1, the molar percent of each compound is indicated below the sample formula.

Sample	a (Å)	u (fractional coordinate)	R_p	R_{wp}	χ^2
A: $LiTi_2O_4$	8.39333(5)	0.2616(1)	0.0536	0.0711	1.30
L1: $Li_2Ti_2O_4$ (23.5 %)	8.3847(2)	0.2575(7)	0.0781	0.1106	1.32
$LiTi_2O_4$ (76.5 %)	8.40593(5)	0.2628(2)			
L2: $LiTi_2O_4$	8.40149(4)	0.2646(1)	0.0680	0.0951	2.30

Table 4-2. Selected interatomic distances for $LiTi_2O_4$ Sample A.

Atoms	Distance (Å)
Li – O	1.986(2)
Ti – O	2.006(1)
Ti – Ti	2.96749(2)

Table 4-3. Selected bond angles for $LiTi_2O_4$ Sample A.

Atoms	Angle (°)
O – Li – O	109.4712(4)
O – Ti – O	84.30(7)
O – Ti – O	95.70(7)
Li – O – Ti	121.32(5)
Ti – O – Ti	95.43(6)

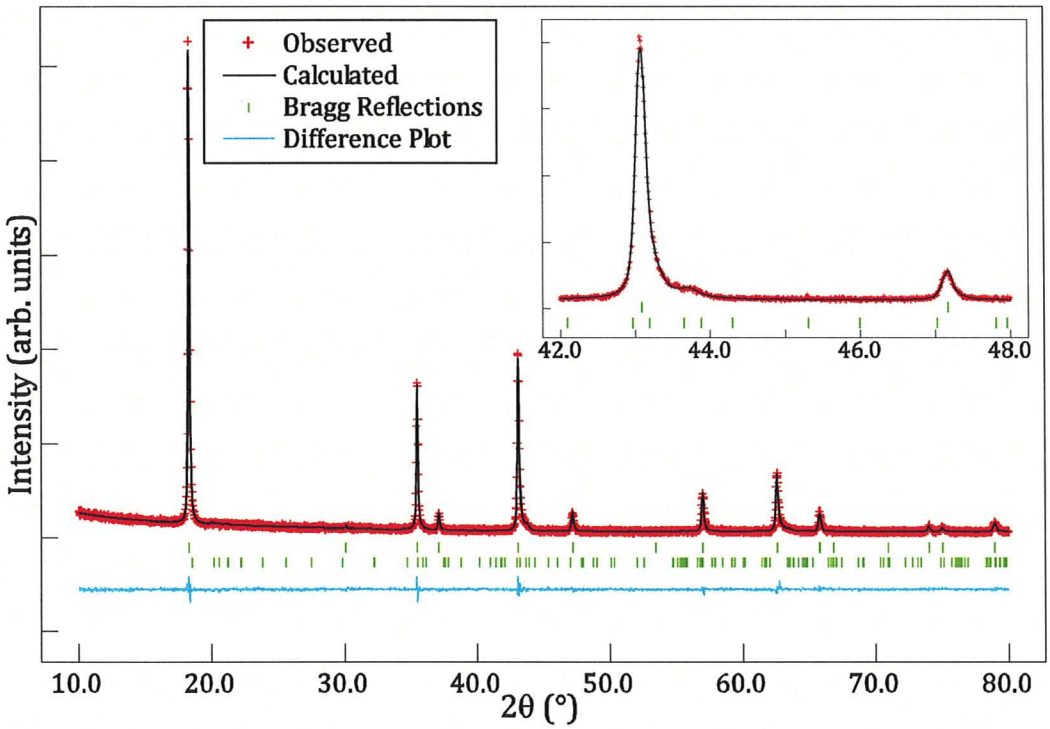

Figure 4-1. X-ray diffraction pattern and Rietveld refinement of Sample A after several months, with major phase $LiTi_2O_4$ spinel (top tick marks) and impurity phase Li_2TiO_3 (bottom tick marks). Inset: Enlargement of range 57° to 68° showing separation of Bragg peaks for LiV_2O_4 and $Li_2V_2O_4$. Crystallographic data are recorded in Tables 4-1 to 4-3.

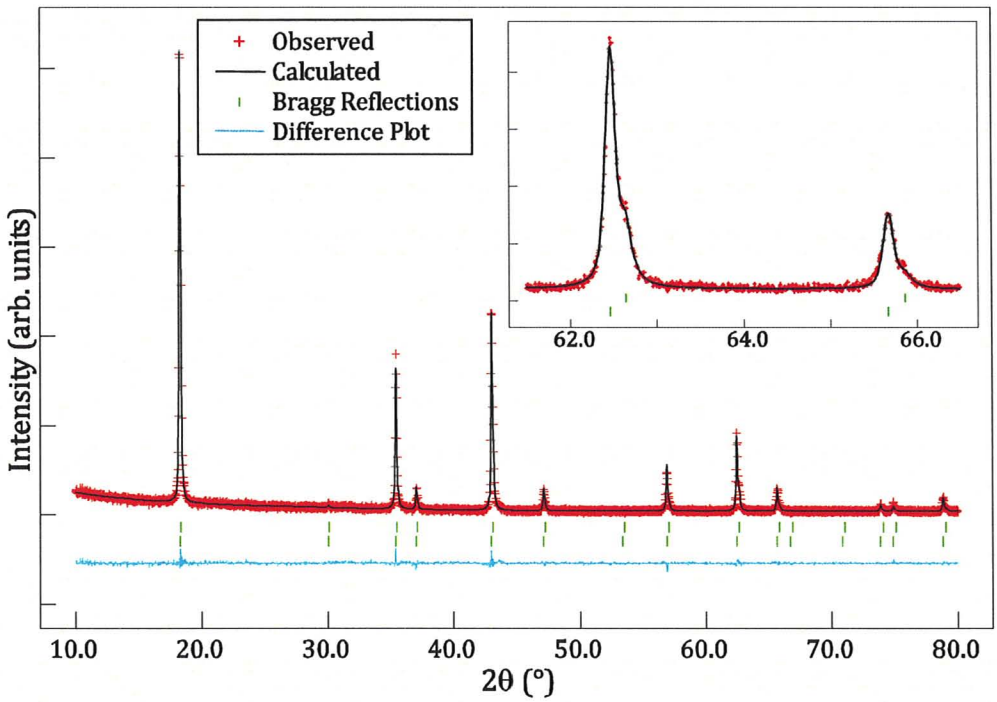

Figure 4-2. X-ray diffraction pattern and Rietveld refinement of Sample L1, the first lithiation of $LiTi_2O_4$ spinel (bottom tick marks) to $Li_2Ti_2O_4$ ordered rock salt (top tick marks). Inset: Enlargement of range 61.5° to 66.5° showing the contribution of $Li_2Ti_2O_4$ to diffraction peaks. Crystallographic data are recorded in Tables 4-1, 4-4 and 4-5.

Table 4-4. Selected interatomic distances for $Li_2Ti_2O_4$ from Sample L1.

Atoms	Distance (Å)
Li – O	2.161(6)
Ti – O	2.035(5)
Ti – Ti	2.96443(8)

Table 4-5. Selected bond angles for $Li_2Ti_2O_4$ from Sample L1.

Atoms	Angle (°)
O – Li – O	86.7(3)
O – Li – O	93.3(3)
O – Ti – O	86.4(3)
O – Ti – O	93.6(3)
Li – O – Li	86.6(3)
Li – O – Ti	93.5(3)
Ti – O – Ti	93.5(3)

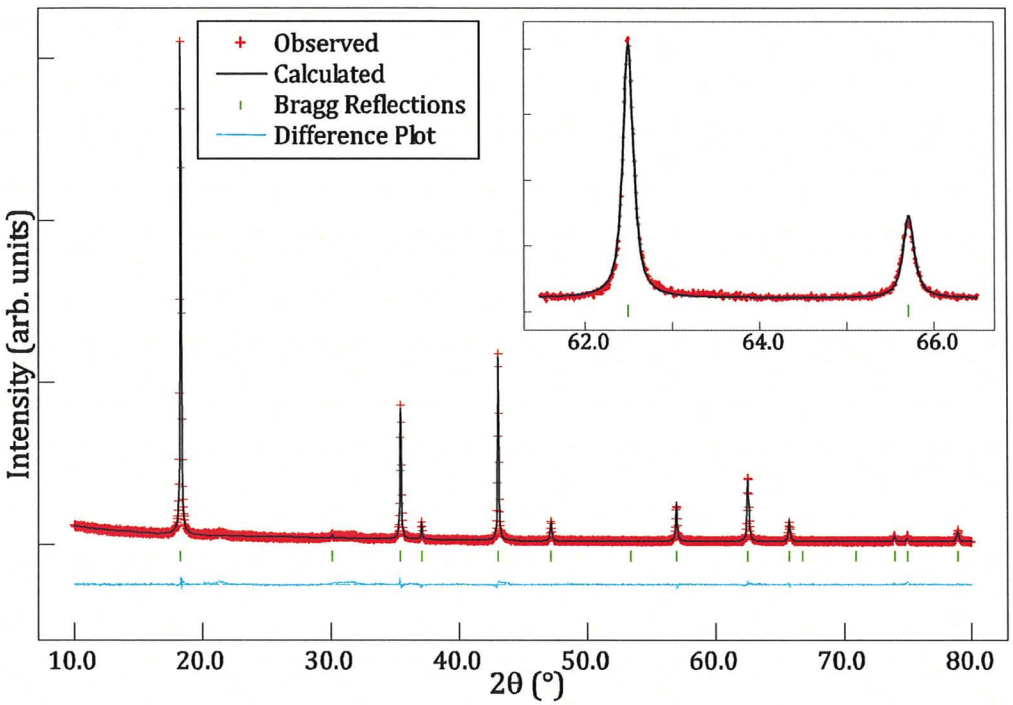

Figure 4-3. X-ray diffraction pattern and Rietveld refinement of L2, the second lithiation of $LiTi_2O_4$ spinel. $LiTi_2O_4$ spinel (bottom tick marks) to $Li_2Ti_2O_4$ ordered rock salt (top tick marks). Inset: Enlargement of range 61.5° to 66.5° showing the absence of contribution of $Li_2Ti_2O_4$ to diffraction peaks. Crystallographic data are recorded in Tables 4-1.

higher-angle shoulders at ~43° and 63° are evidence of an impurity phase that was not evident in earlier diffraction patterns, nor is it evident in the diffraction patterns of L1 or L2. This phase was identified as monoclinic Li_2TiO_3 and refined to 22.8%/mol using the Hill and Howard method [3-32]; however, given the relatively weak intensities, breadth, and dearth of visible peaks for a monoclinic phase, this percentage seems too high to be justified. A refinement considering cubic $LiTiO_2$ as the impurity phase provided a molar percent impurity of 2.3 %, but also resulted in a poorer fit to the data (R_p = 0.0654). Inclusion of either of these impurities resulted in a better fit than a single phase refinement (R_p = 0.0725). The unit cell parameter is close to that determined by Deschanvres, Raveau and Sekkal [64]; however, it is ~0.01 Å smaller than is reported in other literature sources [68-74]. This may be an indication that the lithium stoichiometry is slightly less than 1. This could not be confirmed by ICP-OES (see § 4.1.4). The *u* parameter is in agreement with previous findings.

From the refinement of L1 it was determined that only 23.5 % of the spinel was lithiated to $Li_2Ti_2O_4$ while the rest remained $LiTi_2O_4$. The unit cell parameter *a* and oxygen parameter *u* for $Li_2Ti_2O_4$ are in agreement with the literature [8, 69], as are those for $LiTi_2O_4$.

The spinel phase is the only one present in the refinement of L2, indicating that lithiation failed to occur but also that any previously inserted lithium had been expelled from the $Li_2Ti_2O_4$ phase that had formed. Sources of this delithiation are

discussed in § 4.1.4. The unit cell and oxygen parameters are well in agreement with those found in the literature.

ICP-OES did not prove to be a useful method for evaluating the Li:Ti ratios for each of the compounds due to the strong adsorption of lithium-organic phases to the particle surfaces during lithiation reactions. The relative amount of lithium detected was typically 2 to 4 times higher than what would be expected by stoichiometry. In addition oxygen, carbon and hydrogen cannot be detected directly by the ICP-OES instrument used but must be inferred by subtracting the mass of the other elements present from the total mass of the sample used. Therefore, if an organic phase is present it is only detectable as an augmentation of the mass remaining in a sample once the mass due to lithium and titanium have been subtracted. With this in mind, the calculated oxygen value was 3 to 5 times higher than was expected, evidence of significant amounts of adsorbed material to the samples. This problem may be solved if a suitable solvent can be found that can effectively remove any adsorbed lithium-organic phase while maintaining the integrity of the sample.

Magnetic Data

The magnetic susceptibility plots for Samples A and L2 are shown in Figures 4-4 and 4-5, respectively. Both plots show a superconducting transition due to the Meissner effect, where magnetic susceptibility rapidly plunges below 0 emu·mol^{-1} due to the expulsion of the applied magnetic flux, in turn caused by the complete cancellation of internal magnetic fields. Superconducting transition temperatures T_c

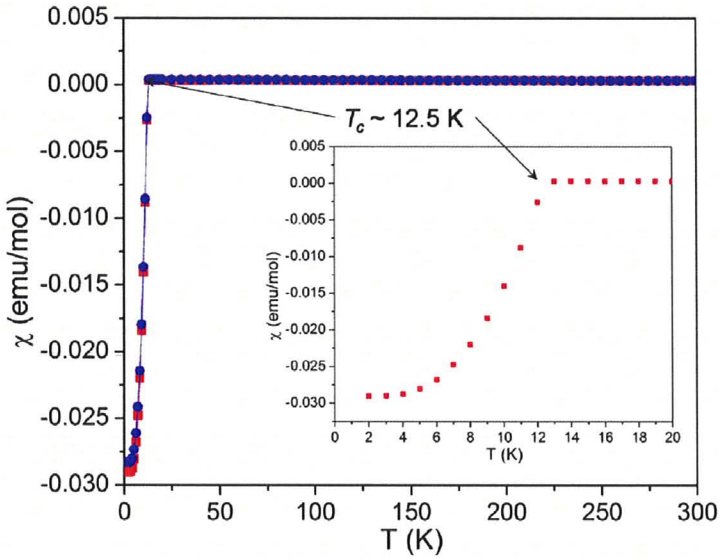

Figure 4-4. Magnetic susceptibility vs. temperature plot for Sample A. Red squares are ZFC data, blue circles are FC. Inset: Close up of the ZFC region 0 to 20 K. The superconducting transition temperature T_c is marked for both plots.

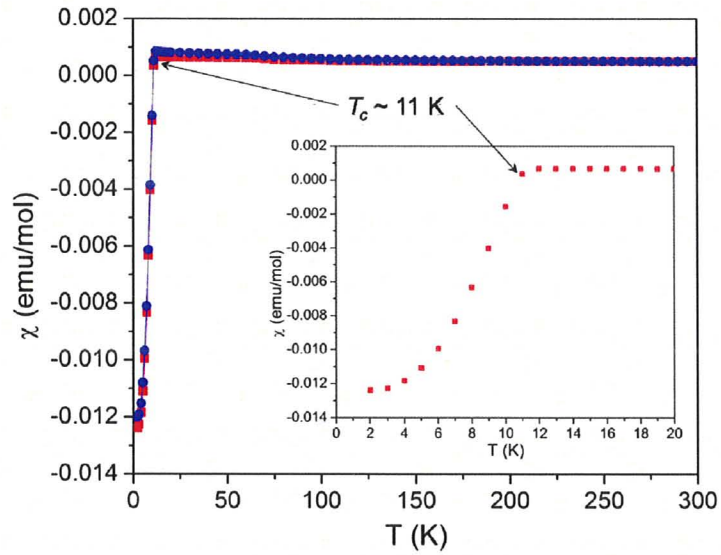

Figure 4-5. Magnetic susceptibility vs. temperature plot for Sample L2. Red squares are ZFC data, blue circles are FC. Inset: Close up of the ZFC region 0 to 20 K. The superconducting transition temperature T_c is marked for both plots.

are both in keeping with literature values, with ~ 12.5 K for A and ~ 11 K for L2 [67, 71, 74, 75, 77-79]. The transition for L2 is probably reduced as a result of site defects introduced to the $LiTi_2O_4$ structure through the processes of lithium insertion and removal. The magnitude of the Meissner effect is also reduced by about half in L2 compared to that of A for similar reasons.

Above the superconducting transition temperatures the behaviours of the two samples differs subtly. The pristine $LiTi_2O_4$ of Sample A displays a weakly temperature dependent susceptibility, described by [70]:

$$\chi_0 = A_m + B_m T \qquad 4.1$$

where A_m = 3.354(2)×10^{-4} emu·mol^{-1} and B_m = -5.71(8)×10^{-8} emu·mol^{-1}·K^{-1}. In contrast, Sample L2 shows two slight features at ~ 60 K and ~ 100 K, both resulting in a small increase in susceptibility with decreasing temperature. These features are attributed to site defects resulting from lithium mobility through the $LiTi_2O_4$ structure. No fit to either a Curie-Weiss law or equation 4.1 was established for L2.

4.1.4 Discussion

The development of a lithium rich impurity phase in Sample A after several months in isolation is likely due to the excess lithium adsorbed to the particle surfaces during the lithiation process as revealed by ICP-OES measurements. The extra lithium is not believed to be derived from the spinel itself since the lattice parameter agrees well with that of the poor quality diffraction pattern taken immediately after synthesis (a =8.3924(1) Å). However, the mechanism of gradual

lithium enrichment is unclear since the expected phase would be $Li_2Ti_2O_4$ rather than related rock salts $LiTiO_2$, which is layered, or Li_2TiO_3, which is partially ordered. The two possible impurities would also be formed by opposing reactions: Li_2TiO_3 requires oxidation of titanium ions while $LiTiO_2$ requires their reduction. Since *n*-BuLi is a reducing agent, the latter scenario seems more likely. It is unclear what the other side products for either scenario would be, although they are likely to be contained in the organic phase.

Complicating this picture is the diffraction pattern of L2. While some delithiation may have occurred during mechanical grinding of L1, this still does not explain the complete absence of the lithiated rock salt or even a lithium enriched impurity phase in the pattern of L2 after an extended reaction period. Assuming the same mechanism to be at work in both cases, one would expect a large quantity of either $Li_2Ti_2O_4$ or the impurity phase to be evident. While broad extremely shallow features around 21° and 30° may indicate a tiny amount of amorphous impurity, these features are nowhere near the diffraction angles of the impurity phase for aged Sample A. A very slight deviation at 43° in the difference map of Sample L2 may be evidence of such a phase, but this deviation is so small as to render such an interpretation meaningless.

Leaching of lithium from $Li_2Ti_2O_4$ would require oxidation of Ti^{3+} to $Ti^{3.5+}$ if the end product were $LiTi_2O_4$. Since the same mechanism is expected to be at work for both the aging of the spinel and the destruction of the ordered rock salt, this adds support to Li_2TiO_3 being the impurity phase in Sample A.

The magnetic susceptibility measurements offer little insight into the matter. While the critical temperature has decreased and the Meissner effect is weaker for L2 than it is for A, this result would be expected for a lithium spinel that has undergone the steps of lithiation and delithiation and therefore increased the number of site-defects in the lattice. However, the slight features at ~ 60 K and ~ 100 K in the magnetic susceptibility may be evidence of an impurity phase. No magnetic susceptibility studies of either Li_2TiO_3 or $LiTiO_2$ could be ascertained to compare against these features.

4.1.5 Conclusions

The study of the lithiation reactions of $LiTi_2O_4$ leaves more questions than answers. The use of *n*-BuLi as a reducing agent and lithium source also leaves the powder particles coated with a lithium-organic phase that makes elemental analysis difficult. This same coating appears to affect the chemistry of the particles as well, gradually forming an impurity phase in samples of $LiTi_2O_4$ while delithiating $Li_2Ti_2O_4$ to the spinel within a few weeks. Magnetic susceptibility measurements prove the reconversion of the rock salt to the superconducting spinel, while small anomalies in the susceptibility above T_c are attributed to lattice defects formed by the cycle of inserting and extracting lithium from the lattice.

Chapter 5: Synthesis, Structure, and Magnetic Properties of Nickel Rhodium Oxide Systems

5.1 $NiRh_2O_4$ and $Ni_xRh_{2-x}O_{3-\delta}$

5.1.1 Background

Nickel rhodite, $NiRh_2O_4$, contains diamagnetic d^6 low-spin Rh^{3+} ions, which have a considerable site preference for octahedral over tetrahedral sites [86]. This forces the d^8 Ni^{2+} into the tetrahedral sites, introducing degeneracy in the t_2 orbitals. In order to relieve this degeneracy, the orbitals undergo Jahn-Teller-type splitting, with the d_{xy} orbital lowering to a singlet and the d_{xz} and d_{yz} orbitals forming an orbital doublet (Figure 5-1) [87]. This splitting results in a tetragonal distortion of the unit cell, creating an elongated c-axis relative to the a- and b-axes and with the new unit cell symmetry of $I4_1/amd$, where a = 5.91 Å and c = 8.67 Å [88]. This unit cell contains half the number of atoms as the cubic $Fd\bar{3}m$ structure and is rotated 45° in the ab-plane relative to the cubic cell, with end-centering of B-site ions in

Table 5-1. Published atomic positions in $NiRh_2O_4$ with space group $I4_1/amd$ [88]. Data were published without standard deviations for the oxygen parameters.

Atom	Position	x	y	z
Ni	4a	0	0.75	0.125
Rh	8d	0	0	0.5
O	16h	0	0.016	0.250

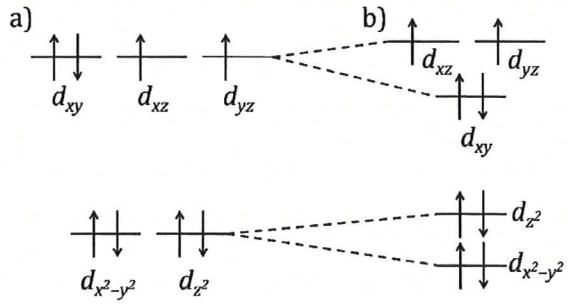

Figure 5-1. Crystal field splitting of d-orbitals in a tetrahedral field for a d^8 transition metal ion a) with no Jahn-Teller type distortion; and b) with Jahn-Teller splitting to relieve the degeneracy of the t_2 orbitals. Crystal field splittings are not to scale.

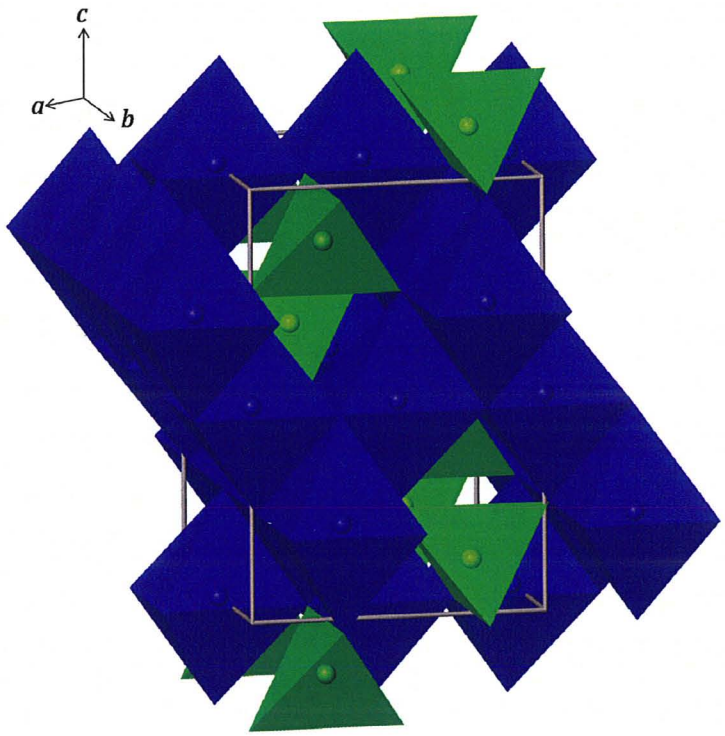

Figure 5-2. Crystal structure of tetragonally distorted $NiRh_2O_4$ spinel in space group $I4_1/amd$, with an elongated *c*-axis. The green tetrahedra represent the Jahn-Teller Ni^{2+} cations, the blue octahedra contain the Rh^{3+} cations, and O^{2-} anions are located at the vertices of the polyhedra.

both the *ab*- and *bc*- planes (Figure 5-2). As with the cubic spinels, the oxygen position is the only adjustable parameter in the unit cell (see Table 5-1).

Magnetic susceptibility data have indicated that $NiRh_2O_4$ undergoes anti-ferromagnetic ordering at T_N = 18 K with θ = -20 K and C = 1.43 emu·K·mol^{-1} Ni (μ_{eff} = 3.38 μ_B) up to 380 K [89]. Above this temperature a structural change to the cubic phase is accompanied by an alteration in the magnetic susceptibility, with C = 2.08 (μ_{eff} = 4.08 μ_B). Note that both these values are significantly above the spin only value for an S = 1 system, i.e. $C_{S.O.}$ = 1 (μ_{eff} = 2.83 μ_B) owing to the incomplete quenching of the angular orbital momentum of tetrahedrally coordinated Ni^{2+}. This effect is enhanced by the increased degeneracy of the high temperature cubic phase. Blasse [90] proposed an exchange mechanism in which the coplanar configuration Ni-O-Rh-O-Ni allows a route for magnetic exchange owing to the significant overlap between Rh e_g orbitals and the O p orbitals.

This chapter deals with the synthesis and magnetic susceptibility data of tetragonal spinel $NiRh_2O_4$ and a newly discovered solid solution $Ni_xRh_{2-x}O_{3-\delta}$, which appears to be based on the orthorhombic structure Rh_2O_3(III). Attention will be given to the structural transformations involved in forming the spinel phase including the emergence of a new phase. The magnetic susceptibility will be compared against published data for the spinel along with discussion about the contribution of the novel phase.

5.1.2 Experimental

Sample Preparation

$NiRh_2O_4$ was produced by reaction of intimately ground and pelletized $NiCO_3$ (99 %, Johnson Matthey) and Rh_2O_3 (99.8 %, Aldrich) at 1000 to 1050 °C under flowing O_2 in a platinum lined alumina boat. The sample was removed every two to four days, ground, and a small amount taken for x-ray analysis before repelletization and further heating. The temperature was kept below 1100 °C to avoid the decomposition of Rh_2O_3 into Rh metal and O_2 [91]. $NiCO_3$ decomposes to CO_2 and NiO, the former of which is removed by the carrier gas while the latter of which takes part in the reaction. The final product was dark grey in colour.

Powder X-ray Diffraction

A PANalytical X'Pert PRO diffractometer was used to collect successive x-ray diffraction patterns of the powder sample. The instrument parameters and data collection conditions have been described previously in § 3.1.2. Phases were identified using EVA and refined using GSAS-EXPGUI [55, 56] and the molar percentages were estimated by converting the weight fractions determined using the Hill and Howard method [57].

Magnetic Measurements

Magnetic susceptibility measurements were performed using a Quantum Design MPMS SQUID magnetometer following the same procedure and program outlined in § 3.1.2. The applied magnetic field was 1000 Oe.

5.1.3 Results and Discussion

Structural Characterization

The powder x-ray diffraction pattern for $NiRh_2O_4$ after the fifth and final sintering is shown along with Rietveld refinement in Figure 5-3 and summarized in Table 5-2. The unit cell parameters for the spinel are in good agreement with the literature value; however, the oxygen parameters were found to be (0, 0.00656, 0.2651), which are shifted somewhat from the literature value [88]. This results in shorter axial Rh - O distances relative to the equatorial distance and greater degree of distortion for the rhodium octahedra while elongating and enlarging the nickel tetrahedra. A small amount of the platinum liner was found incorporated in the powder pattern and was included in the Rietveld refinement. It is not believed to have had an effect on the chemistry of the reactions.

The rhodium (III) oxide used in the synthesis was found to be composed of two polymorphs: a rhombohedral, corundum phase, Rh_2O_3(I), with space group $R\bar{3}c$, and an orthorhombic phase, Rh_2O_3(III), with space group *Pbca*. These are produced under slightly different conditions, with the former being a low temperature phase and the latter emerging by heating the corundum phase between 750 °C to 1000 °C [92]; however, computational studies have shown a broad temperature region where both forms coexist at low pressures [93].

By studying the successive x-ray diffraction patterns, it is readily apparent that the signal due to the corundum phase is negligible by the fifth firing, whereas

Table 5-2. Crystallographic results from Rietveld refinement of the fifth firing of a pellet containing $NiCO_3$ and Rh_2O_3 with a small amount of platinum impurity. Molar percent impurities were estimated by conversion of the weight percents determined via the Hill & Howard method [57]. Rietveld agreement factors were $R_p = 0.0906$, $R_{wp} = 0.1265$, and $\chi^2 = 4.42$.

Compound	**$NiRh_2O_4$**	**$Ni_xRh_{2-x}O_{3-\delta}$**	**Pt**
Space group	$I4_1/amd$	$Pbca$	$Fm\bar{3}m$
Cell Parameters	$a = 5.91043(2)$ $c = 8.67489(5)$	$a = 5.1393(1)$ $b = 5.4209(2)$ $c = 14.6823(5)$	$a = 3.8737(1)$
O parameter ($NiRh_2O_4$)	$x = 0$ $y = 0.0065(5)$ $z = 0.2621(4))$		
Molar Percent	64.1	35.4	0.6

Table 5-3. Selected interatomic distances for $NiRh_2O_4$.

Atoms	**Distance (Å)**
Ni – O	1.927(3)
Rh – O	2.064(3)
Rh – Rh	2.95522(1)
Rh – Rh	3.01165(1)

Table 5-4. Selected bond angles for $NiRh_2O_4$.

Atoms	**Angle (°)**
O – Ni – O	103.8(2)
O – Ni – O	112.4(1)
O – Rh – O	86.3(1)
O – Rh – O	93.7(1)
Ni – O – Rh	121.1(1)
Ni – O –Rh	127.0(2)
Rh – O – Rh	91.4(1)
Rh – O – Rh	93.7(1)

Table 5-5. Fractional coordinates, occupancy and thermal displacement parameters for $Ni_{0.6}Rh_{1.4}O_{3-\delta}$. All atoms are in a general 8*c* position, (*x*, *y*, *z*).

Atom	*x*	*y*	*z*	Occupancy	u_{iso}
M1	0.013(1)	0.2212(8)	0.0777(4)	Ni: 0.2(1) Rh: 0.8(1)	0.018(3)
M2	0.0046(1)	-0.198(1)	0.1776(4)	Ni: 0.42(9) Rh: 0.58(9)	0.025(4)
O1	0.183(8)	0.14(1)	0.232(3)	0.79(6)	0.01
O2	-0.278(5)	-0.073(7)	0.146(3)	1.0	0.01
O3	0.181(7)	-0.127(8)	0.040(3)	0.93(8)	0.01

Table 5-6. Selected interatomic distances for $Ni_{0.6}Rh_{1.4}O_{3-\delta}$.

Atoms	Distance (Å)
M1 – O1	2.46(5)
M1 – O2	1.92(3)
M1 – O2	2.41(3)
M1 – O3	1.86(3)
M1 – O3	2.06(4)
M1 – O3	2.14(4)
M2 – O1	1.87(6)
M2 – O1	2.00(4)
M2 – O1	2.19(6)
M2 – O2	1.67(3)
M2 – O2	2.39(4)
M2 – O3	2.24(4)
M1 – M2	2.707(5)

Table 5-7. Selected bond angles for $Ni_{0.6}Rh_{1.4}O_{3-\delta}$.

Atoms	Angle (°)
O2 – M1 – O3	106(1)
O2 – M1 – O3	115(2)
O2 – M1 – O3	154(2)
O3 – M1 – O3	76(2)
O3 – M1 – O3	89(1)
O3 – M1 – O3	106(1)
O1 – M2 – O1	84(1)
O1 – M2 – O1	86(2)
O1 – M2 – O1	111(2)
O1 – M2 – O2	87(2)
O1 – M2 – O2	97(2)
O1 – M2 – O2	172(2)

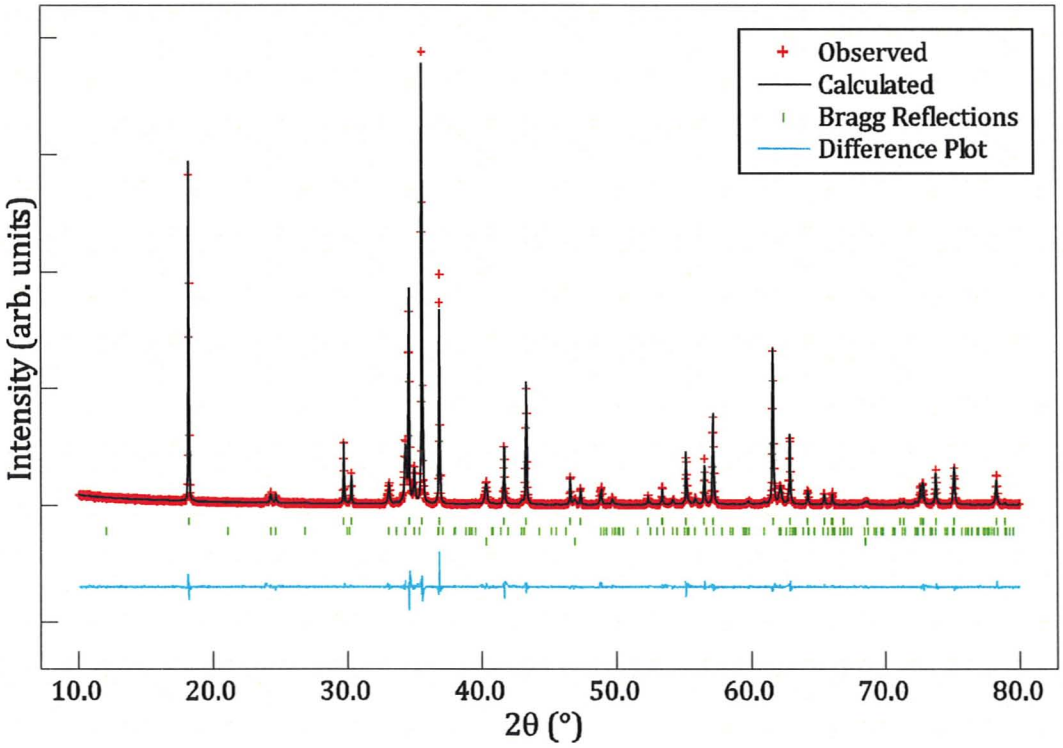

Figure 5-3. X-ray diffraction pattern and Rietveld refinement of $NiRh_2O_4$ with $Ni_xRh_{2-x}O_{3-\delta}$ and Pt metal impurities, represented respectively by the top, middle, and bottom tick marks. Crystallographic data are recorded in Tables 5-2 to 5-7.

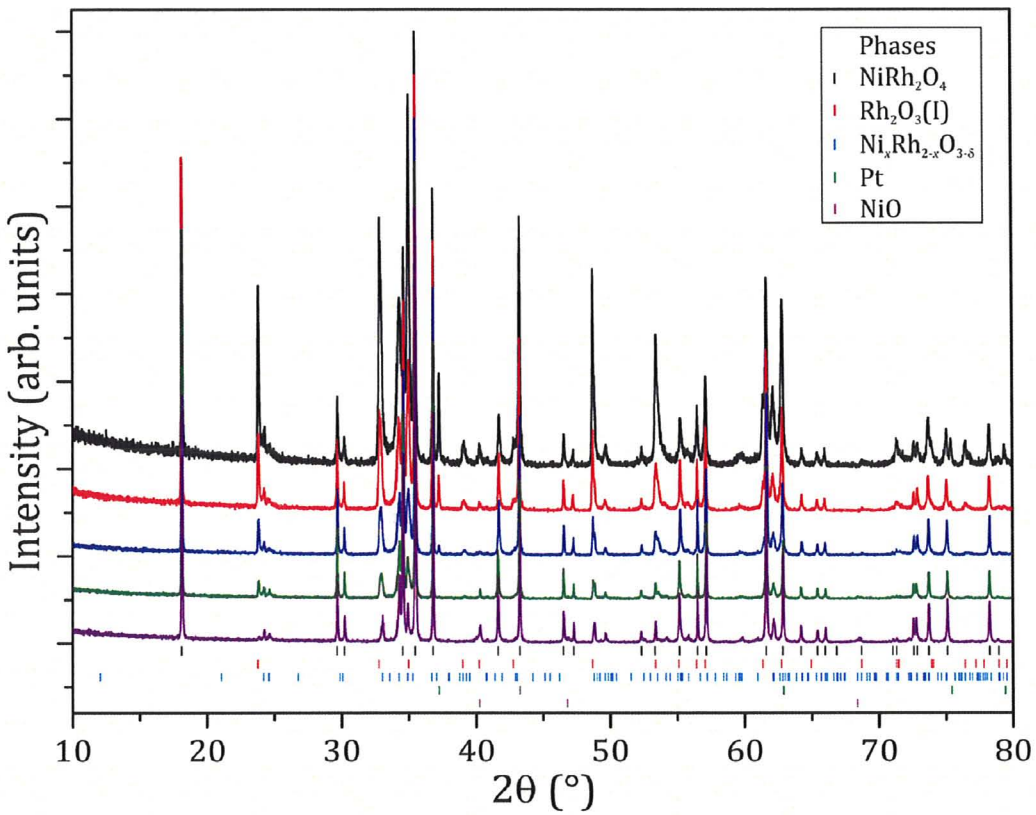

Figure 5-4. Normalized successive x-ray diffraction patterns for reaction of $NiCO_3$ and Rh_2O_3. The top black pattern was collected after 2 days at 1000 °C, with each successive pattern following at 3-4 day intervals. The tickmarks at the bottom represent are for phases $NiRh_2O_4$, Rh_2O_3(I), "Rh_2O_3(III)", NiO, and Pt metal, respectively. Note that while the signals for NiO and Rh_2O_3(I) rapidly disappear and are negligible by the fourth and fifth firing, respectively, the decrease in intensity for peaks attributed to "Rh_2O_3(III)" is insignificant after the third firing.

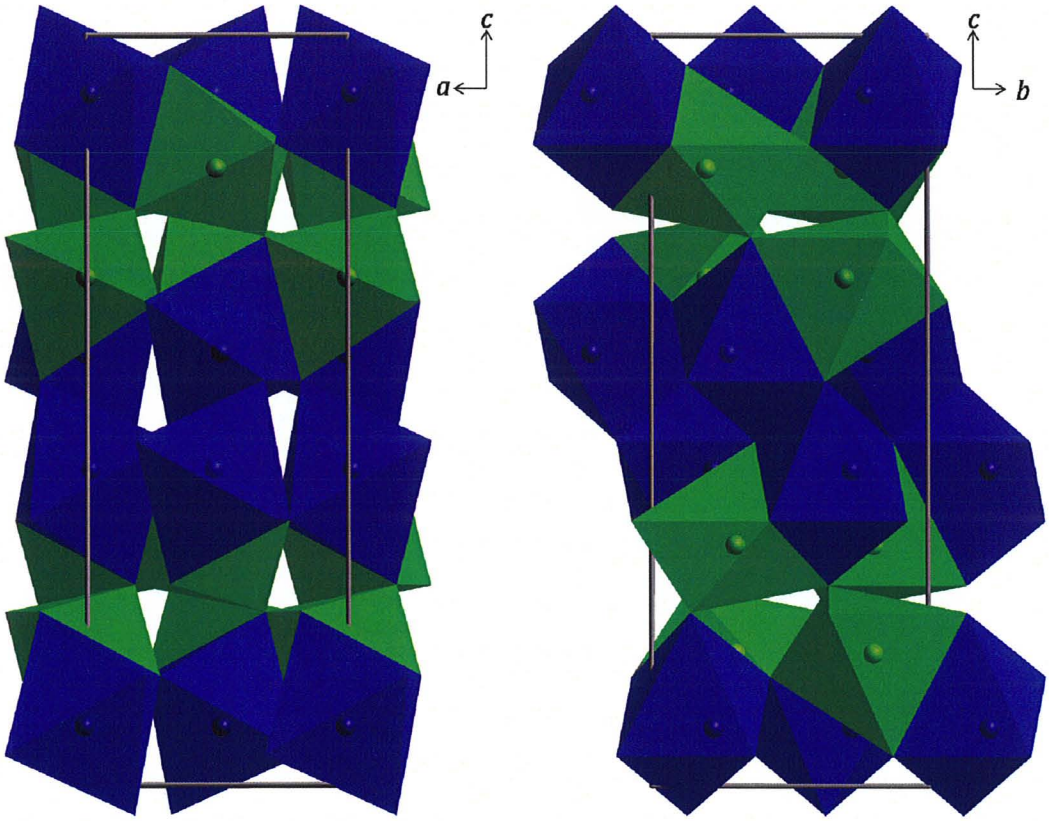

Figure 5-5. Crystal structure of $Ni_{0.6}Rh_{1.4}O_{3-\delta}$ as viewed down the *b*-direction (left) and down the *a*-direction (right). The colours represent the two distinct metal sites, where blue is M1 and green is M2.

the orthorhombic phase persists with a relative peak intensity that appears to remain constant beyond the third firing (Figure 5-4). This may partly involve a phase transition of some of the Rh_2O_3(I) to Rh_2O_3(III), which may suggest that the high temperature phase has reduced chemical activity compared to the low temperature phase. Both structures are composed of face- and edge sharing octahedra, but the orthorhombic phase is somewhat denser than the corundum phase, possibly impeding the diffusion of rhodium ions that is essential for solid state reactions.

It is also worth noting that the first attempts to make $NiRh_2O_4$ in this study were performed in air at 1100 °C and resulted in the decomposition of rhodium oxide into rhodium metal, oxygen, and a third phase with a similar pattern to those of rhodium and nickel metals but with an intermediate unit cell size. In addition, heating the decomposed product under flowing oxygen produced a phase with a diffraction pattern similar to Rh_2O_3(III) but with a smaller unit cell. This reduced unit cell size was also observed in the sample presented here which at no time underwent decomposition. It is proposed that a side reaction between Rh_2O_3 and NiO has occurred involving the incorporation of nickel into the orthorhombic structure leading to $Ni_xRh_{2-x}O_{3-\delta}$, where δ is the oxygen deficiency. Therefore, the decomposition product would likely have been an alloy or solid solution of rhodium and nickel. The proposed side reaction would also explain why in a stoichiometric mixture of nickel oxide and rhodium sesquioxide no diffraction peaks for unreacted NiO were observed despite Rh_2O_3(III) remaining as the major impurity phase.

Treating the orthorhombic impurity phase as a solid solution of NiO and Rh_2O_3(III) in the Rietveld refinement resulted in significant improvement in the agreement factors. The space group and unit cell parameters are shown in Table 5-2 while atomic positions, interatomic distances, and bond angles are summarized in Tables 5-5, 5-6, and 5-7, respectively. Figure 5-5 shows the structure of the $Ni_xRh_{2-x}O_{3-\delta}$. The attempts to refine the u_{iso} of the oxygen atoms and the occupancy of atom O2 resulted in unphysical values and so were left unrefined.

Of the two rhodium sites in the crystal structure M2 appears to have absorbed about twice as much nickel as M1. The reason for this is not clear. The octahedral environments at both sites display significant distortion with M – O bond distances ranging from 1.86(3) to 2.46(5) Å for M1 and 1.67(3) to 2.39(4) Å for M2. The smallest bond distance in the M2 octahedron is appreciably smaller than either the Rh – O or Ni – O interatomic distance predicted using the Shannon radii, respectively 2.05 Å and 2.07 Å for four-coordinate oxygen and six-coordinate metals [94]. This site represents one of the oxygen ions situated along the face shared with an M1 octahedron, raising the possibility of strong M-M interactions through the oxygen atoms in shared faces; however, the interatomic distance from M1 to the same oxygen is 2.41(3) Å, one of the longest M – O bond lengths in the structure. Also, while the M2 site has shifted closer to the shared face relative to the Rh_2O_3(III) structure, M1 has actually moved further away so that the M1-M2 distance through the shared face has increased from 2.668 Å in Rh_2O_3(III) to 2.707(5) Å in the novel phase. The large thermal displacement factor for M2 may reflect some disorder in

the metal site that would largely be attributable to oxygen vacancies, particularly since O1 is calculated to be the site with the most vacancies and forms the basis for half the oxygen atoms in the M2 octahedron. However, it should be noted that oxygen is relatively difficult to detect by x-ray diffraction due to its small atomic number, especially when compared against much heavier elements such as rhodium. The short Rh – O distance should be viewed with some skepticism until a technique that is more sensitive to oxygen can be employed, such as neutron diffraction.

The calculated Ni:Rh ratio in the orthorhombic spinel is ~1:2.3, a value approaching the ratio of 1:2 expected in the spinel. This adds support to the argument that the NiO missing from the powder pattern is being used up to form the new orthorhombic phase. Also, by refining the fractional occupation of oxygen sites a value of $\delta = 0.3$ is obtained, which is the value required for charge balance.

Magnetic Data

Both the χ vs. T and $1/\chi$ vs. T plots are shown in Figure 5-6, the latter also showing the Curie-Weiss fit where $C = 2.403(9)$ emu·K·mol^{-1} Ni and $\theta = -56(1)$ K. The C-W law holds true above ~125 K but the susceptibility deviates strongly below this temperature. The negative Weiss temperature suggests antiferromagnetic spin interactions as reported in the literature [89, 90], but the curvature of the plot strongly resembles that expected for ferromagnetic spin interactions, especially

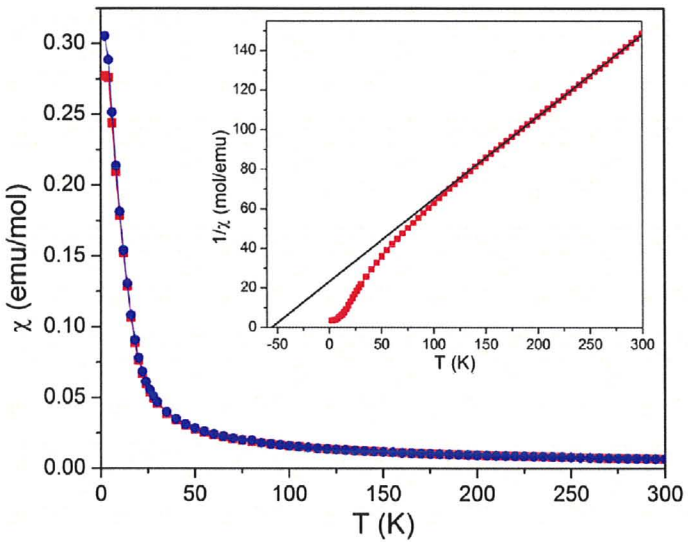

Figure 5-6. Magnetic susceptibility vs. temperature for $NiRh_2O_4$ with impurity phases. Red squares are ZFC data, blue circles are FC. Inset: Inverse magnetic susceptibility vs. temperature along with Curie Weiss fit (black line): C = 2.403(9) emu·K·mol^{-1} Ni and θ = -56(1) K.

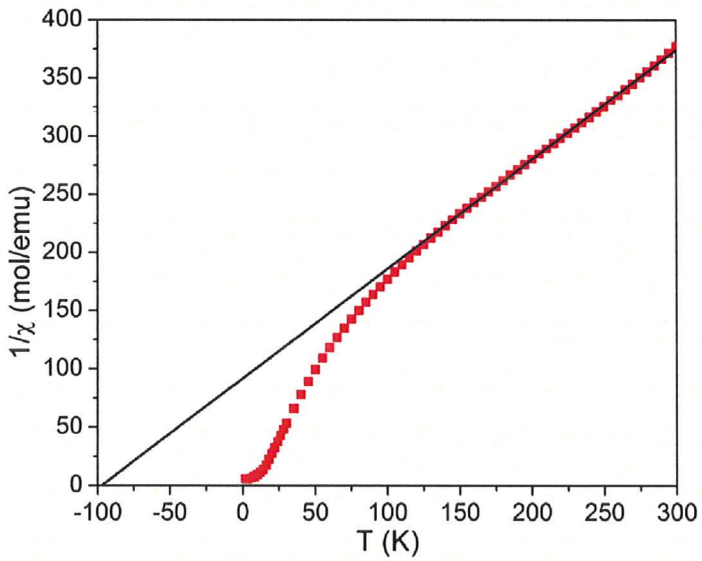

Figure 5-7. Inverse ZFC magnetic susceptibility vs. temperature for $Ni_xRh_{2-x}O_{3-\delta}$ with $NiRh_2O_4$ contribution removed. Curie Weiss fit (black line): C = 1.864(8) emu·K·mol^{-1} Ni and θ = -98(1) K.

for the $1/\chi$ vs. T plot. While the data presented are for freshly sintered powder, the air sensitivity of the sample was also demonstrated by repeating the data collection two months after the initial collection, which found significant enhancement of both the Curie constant and the Weiss temperature.

These data are significantly different from those previously published [90]. The deviation from published work is clearly attributable to the significant phase impurity $Ni_xRh_{2-x}O_{3-\delta}$. An attempt was made to isolate the magnetic susceptibility of the impurity phase by subtracting the contribution of $NiRh_2O_4$ using the data obtained from Blasse [90]. While such a process can be problematic, it can also provide an estimate of the type of magnetic interactions operating in the system. The results are shown in Figure 5-7. Fitting the data to a Curie-Weiss law provides C = 1.864(8) emu·K·mol^{-1} Ni and θ = -98(1) K. The Curie constant is still much larger than is expected for a dilute d^8 spin-only system of Ni^{2+} ions (S = 1, C = 1), indicating that there are significant magnetic impurities present that still have not been accounted for. Similarly, the Weiss temperature continues to indicate antiferro-magnetic interactions despite a curve shape suggestive of ferromagnetic ordering.

5.1.4 Conclusions

In conclusion, the synthesis of $NiRh_2O_4$ is complicated by the decomposition of Rh_2O_3 at 1100 °C, but more importantly by the formation of a novel Ni – Rh – O phase derived from the solid solution of NiO in the orthorhombic Rh_2O_3(III) structure. Rietveld analysis of the spinel reveals a phase that is in agreement with

what has been reported in the literature. The novel nickel rhodite phase refines in the *Pbca* space group with a structure similar to that of Rh_2O_3(III) with ~29 % of the rhodium substituted by nickel and oxygen occupancies close to that required for charge balance. One M – O bond in the structure is anomalously short, but this result must be verified by other methods such as neutron diffraction.

Curie-Weiss fits to the magnetic susceptibility measurements indicate antiferromagnetic interactions despite a curve shape resembling that of a ferro-magnetic material. The Curie constant obtained is significantly larger than expected for a $S = 1$ system, an indication that the system contains many magnetic impurities and defects

Chapter 6: Conclusions and Future Work

6.1 Conclusions

Lithium transition metal oxide spinels, LiM_2O_4 (M = Ti, V) were synthesized using a variety of methods and lithiated to produce rock salt phases of the type $Li_2M_2O_4$ which maintain the pyrochlore sublattice of the transition metal ions. The magnetic susceptibility of the compounds was studied to determine the role of geometric frustration in the lithiated products. In addition, an investigation into the distorted spinel $NiRh_2O_4$ led to the discovery of a new solid solution of nominal composition $Ni_xRh_{2-x}O_{4-\delta}$, which is related to the structure of orthorhombic Rh_2O_3(III).

In the investigations of the lithium vanadium spinel LiV_2O_4, the solid state synthesis using $Li_2VO_{3.5}$ and V_2O_3 as reactants proved to have the fewest chemical and magnetic impurities. A novel chimie douce synthesis using gaseous I_2 to extract lithium from $LiVO_2$ followed by heating to 500 °C to transform the product to spinel showed great promise, but the highly variable results and the inability to generate a spinel phase free of chemical impurities proved this synthesis was less than ideal. Magnetic susceptibility measurements of the lithiated spinel $Li_2V_2O_4$ were highly sample dependent. Common features include broad maxima at ~35 and 130 K, divergence between ZFC and FC curves below at least ~100 K, and the absence of any discernable Curie-Weiss range up to 600 K. All of these are indications of a strongly frustrated antiferromagnet.

In the lithiation of $LiTi_2O_4$ to $Li_2Ti_2O_4$, difficulties arose due to the adsorption of lithium containing organic phases to the particle surfaces during reaction with *n*-BuLi. Lithium extraction from $Li_2Ti_2O_4$ proceeded within a few weeks in an inert environment, regenerating the $LiTi_2O_4$ spinel phase. Differences in the magnetic susceptibility data of the pristine and lithiated-delithiated samples were taken as evidence of the formation of site defects in the regenerated spinel.

The investigation of synthesis and structure of tetragonally distorted $NiRh_2O_4$ spinel uncovered a new phase, $Ni_xRh_{2-x}O_{3-\delta}$, which appears to be a solid solution of NiO in Rh_2O_3(III). The crystallographic results estimate a value of $x = 0.6$, explaining why NiO disappears from the diffraction pattern despite the persistence of the Rh_2O_3(III)-like phase. The magnetic susceptibility curve resembles that of a ferromagnet, but the Curie-Weiss fit indicates antiferromagnetic behaviour with negative θ. The large Curie constant indicates strong magnetic impurities are present, further clouding the magnetic structures of both materials.

6.2 Future Work

There is much work still to be done for each of the investigations presented here. Refinement of synthetic procedures in all cases is required, particularly regarding washing procedures following lithiation reactions with *n*-BuLi in order to remove the lithium-organic phases that contaminate each of the products. A route

must also be discovered that can separate $NiRh_2O_4$ spinel from the newly discovered $Ni_xRh_{2-x}O_{3-\delta}$.

Neutron diffraction would be an invaluable tool in evaluating the crystal structures of all species studied. Unlike x-rays, for which oxygen is difficult to locate and lithium is nearly invisible, neutron diffraction scattering lengths *b* are nearly Z independent and many light atoms have scattering lengths comparable to or greater than heavier elements. With one exception, the elements used in each of the systems studied can easily be distinguished from each other based on scattering length alone. The one exception is between Rh (b = 5.88 fm) and O (b = 5.803 fm) [95]; however, the distinct environments found for each of these elements in both $NiRh_2O_4$ and $Ni_xRh_{2-x}O_{3-\delta}$ would make them easily distinguishable in the first place. Neutron diffraction also provides a way to probe the magnetic structures of the compounds studied even if short-range ordering predominates due to the ability of magnetic fields to diffract neutrons as well as atomic nuclei.

Scanning electron microscopy (SEM) would be useful in determining the particle size of LiV_2O_4 and $LiTi_2O_4$ powders through direct imaging. Electron diffraction using a transmission electron microscope (TEM) could allow single crystal diffraction patterns even from powder samples. ^{7}Li solid state nuclear magnetic resonance techniques (SSNMR) would provide valuable information about the local environments of the elements and could be used to determine the diffusion pathways of lithium ions through the spinel structure.

Heat capacity measurements can give insight into the nature of magnetic ordering by providing information about the amount of entropy removed from a system through the process of ordering and can clarify the nature of features in the magnetic susceptibility even for short range ordering.

Appendix: LiV_2O_4 Powder X-ray Diffraction Patterns

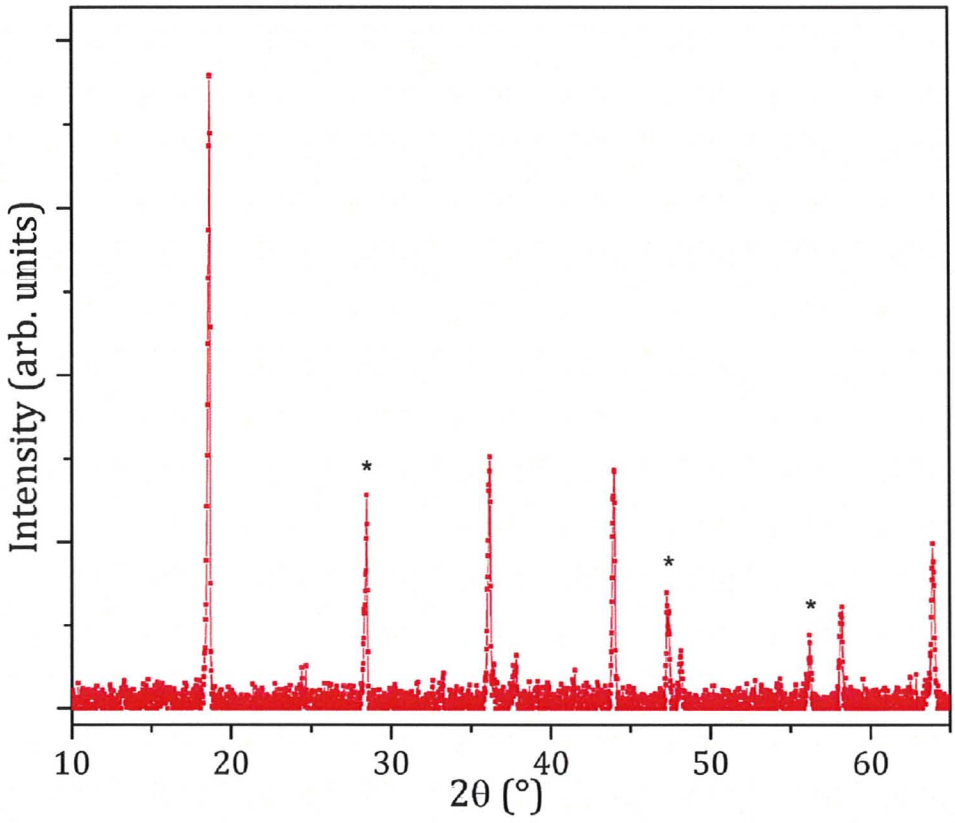

Figure A-1. X-ray diffraction pattern of Sample 1. Silicon peaks are marked with an asterisk (*). Crystallographic data are recorded in Table 3-3.

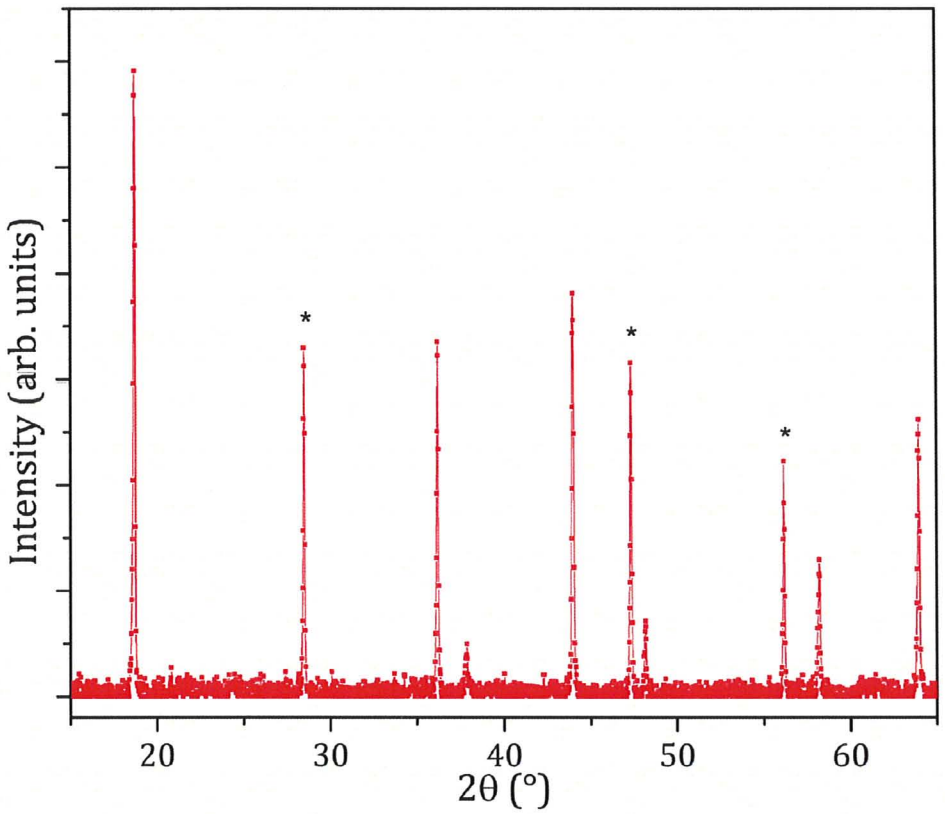

Figure A-2. X-ray diffraction pattern of Sample 2. Silicon peaks are marked with an asterisk (*). Crystallographic data are recorded in Table 3-3.

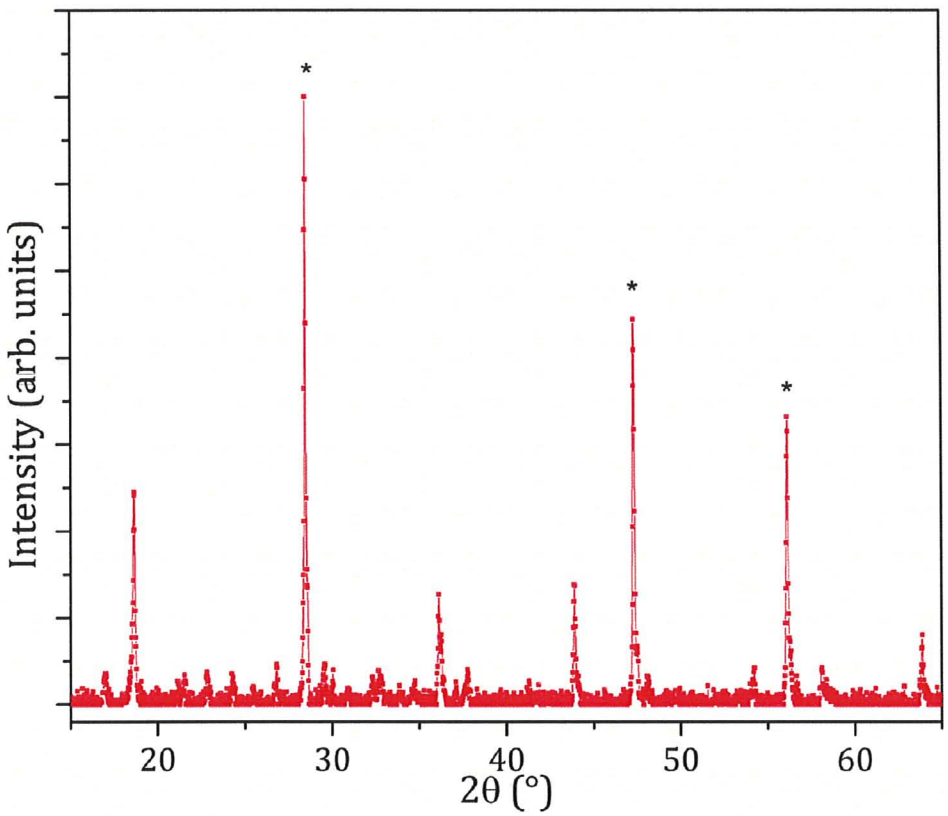

Figure A-3. X-ray diffraction pattern of Sample 3. Silicon peaks are marked with an asterisk (*). Crystallographic data are recorded in Table 3-3.

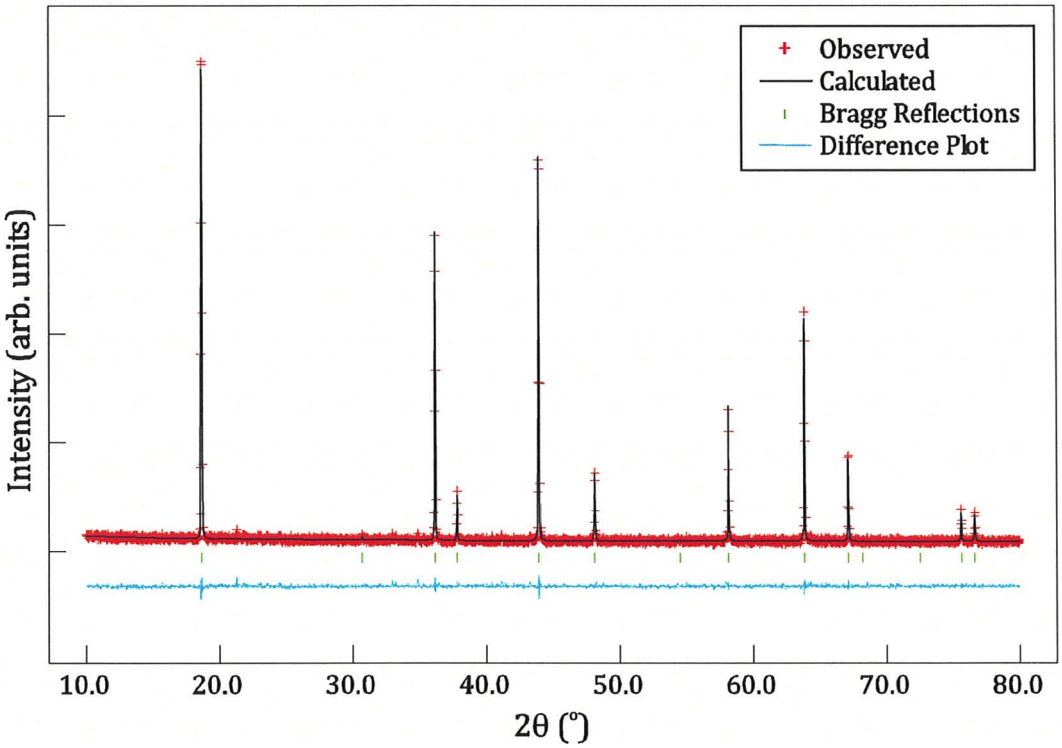

Figure A-4. X-ray diffraction pattern and Rietveld refinement of Sample 5. Crystallographic data are recorded in Table 3-3.

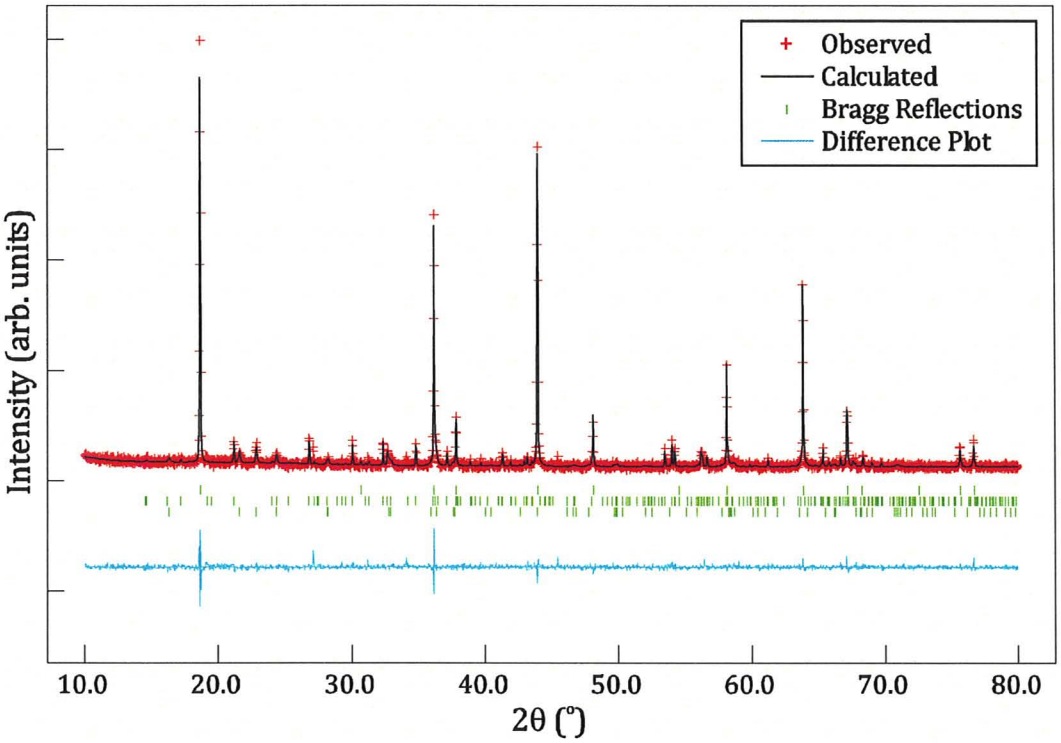

Figure A-5. X-ray diffraction pattern and Rietveld refinement of Sample 6. Impurity phases are Li_3VO_4 (bottom tick marks) and V_4O_7 (middle tick marks). Crystallographic data are recorded in Table 3-3.

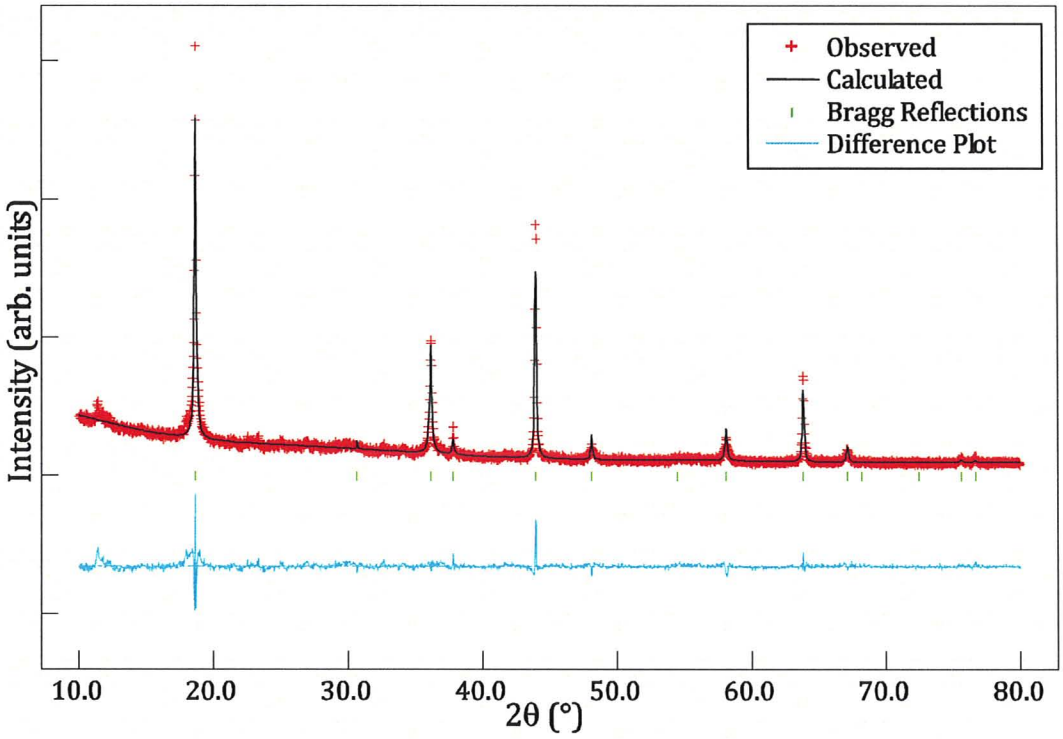

Figure A-6. X-ray diffraction pattern and Rietveld refinement of Sample 7. Inpurity phases are unknown. Crystallographic data are recorded in Table 3-3.

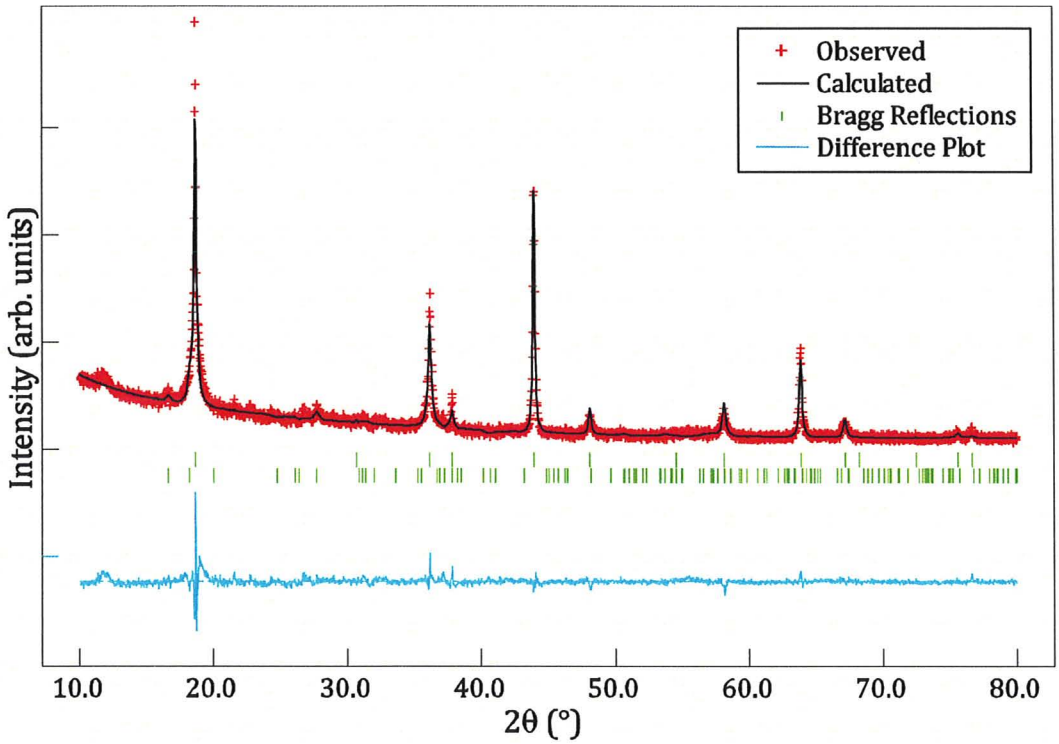

Figure A-7. X-ray diffraction pattern and Rietveld refinement of Sample 8. Impurity phases are LiV_2O_5 (bottom tick marks), Li_3VO_4 (not refined), and other unknown trace impurities. Crystallographic data are recorded in Table 3-3.

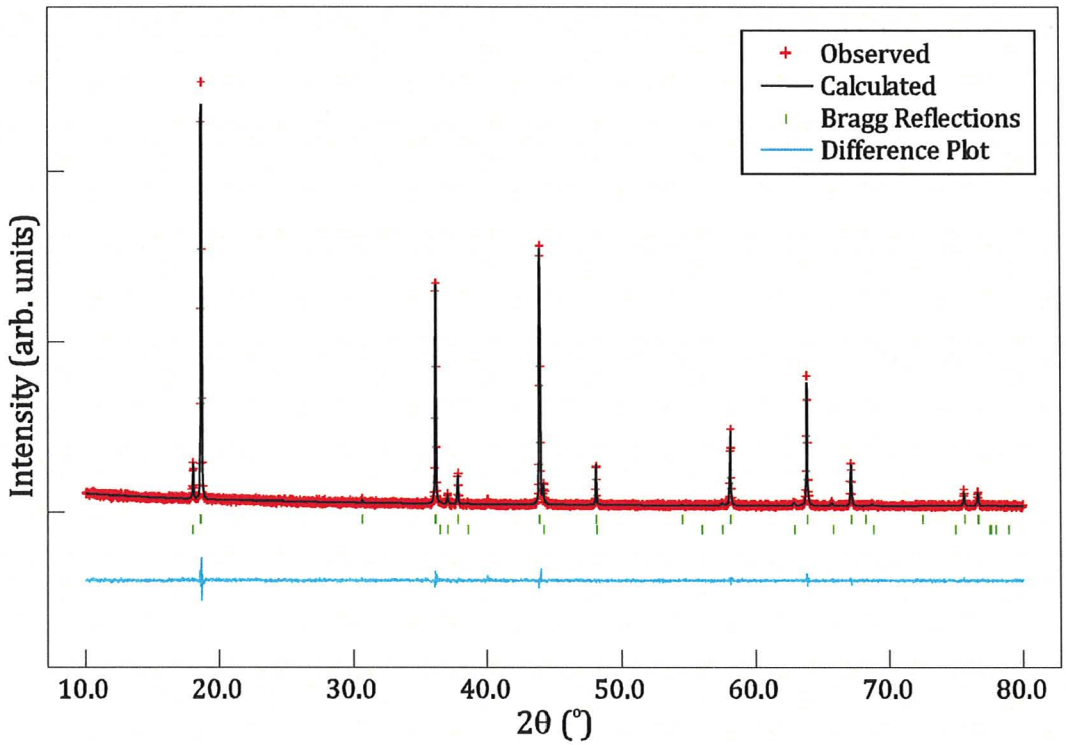

Figure A-8. X-ray diffraction pattern and Rietveld refinement of Sample 9. Impurity phase is $LiVO_2$ (bottom tick marks). Crystallographic data are recorded in Table 3-3.

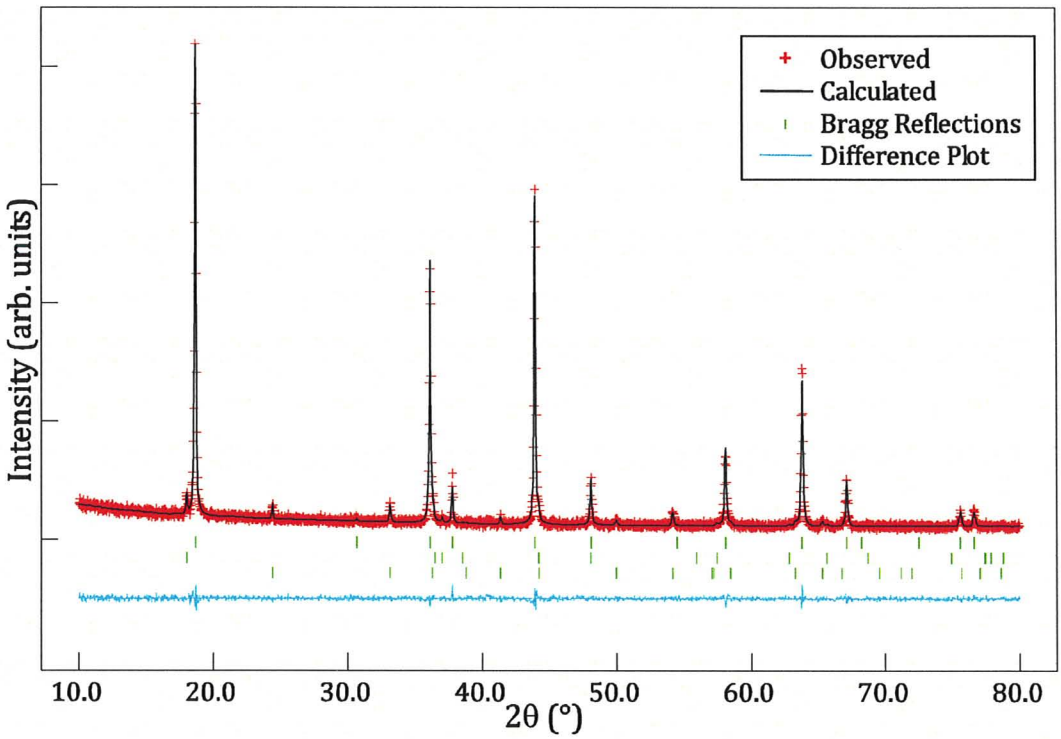

Figure A-9. X-ray diffraction pattern and Rietveld refinement of Sample 10. Impurity phases are $LiVO_2$ (middle tick marks) and V_2O_3 (bottom tick marks). Crystallographic data are recorded in Table 3-3.

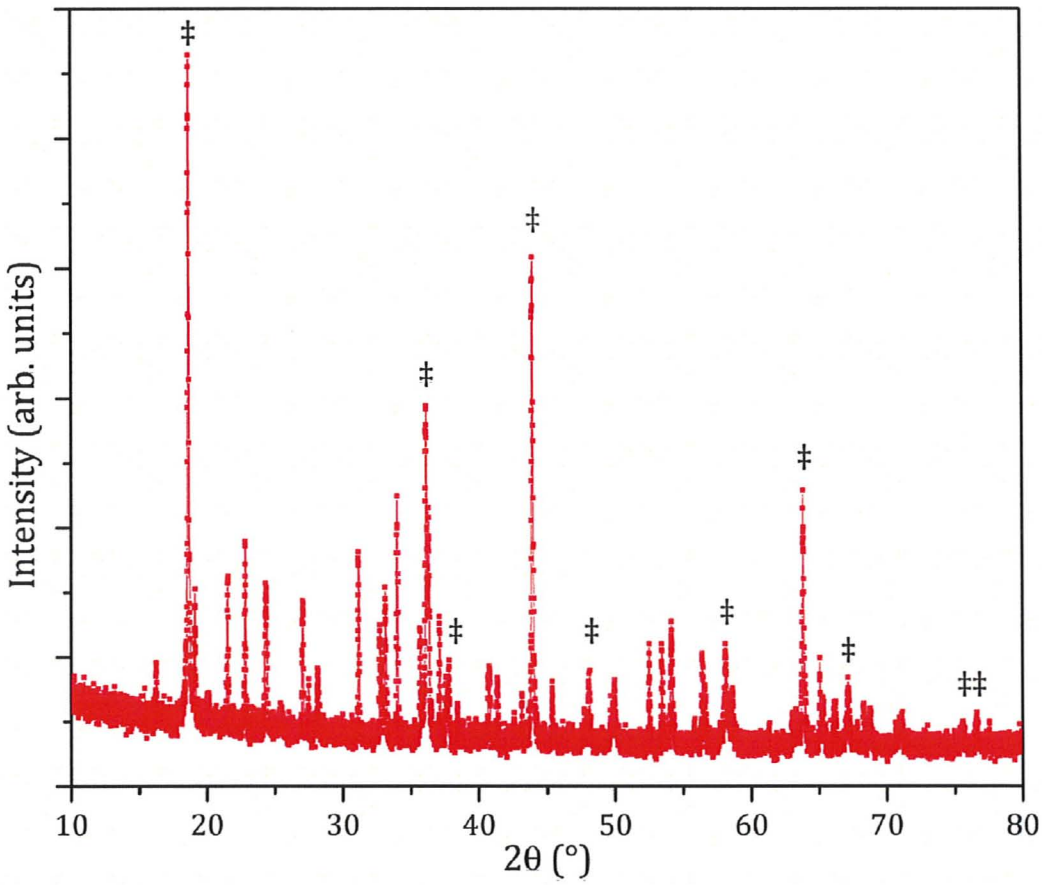

Figure A-10. X-ray diffraction pattern of Sample11. Peaks deriving from diffraction of LiV_2O_4 are marked with (‡). Impurity phases include V_2O_3, V_3O_5, and Li_3VO_4, among other unidentified phases. Crystallographic data are recorded in Table 3-3.

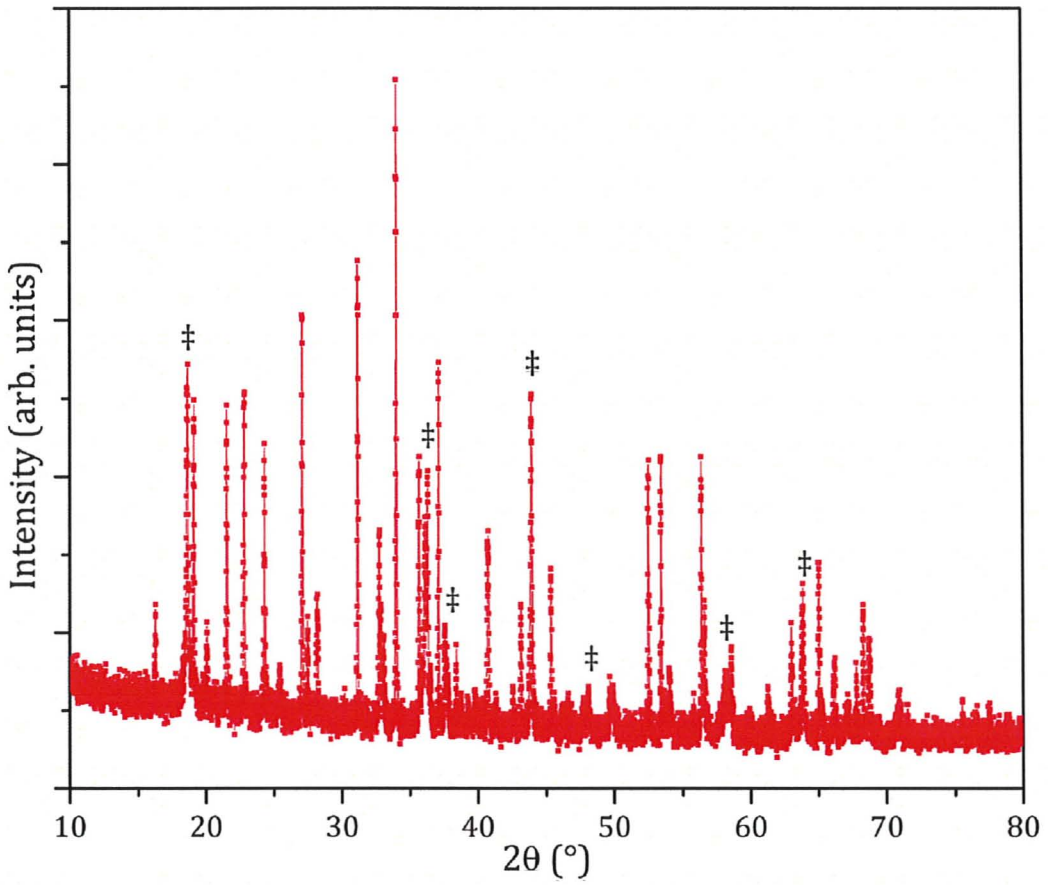

Figure A-11. X-ray diffraction pattern of Sample12. Peaks deriving from the diffraction of LiV_2O_4 are marked with (‡). Impurity phases include V_2O_3, V_3O_5, and Li_3VO_4, among other unidentified phases. Crystallographic data are recorded in Table 3-3.

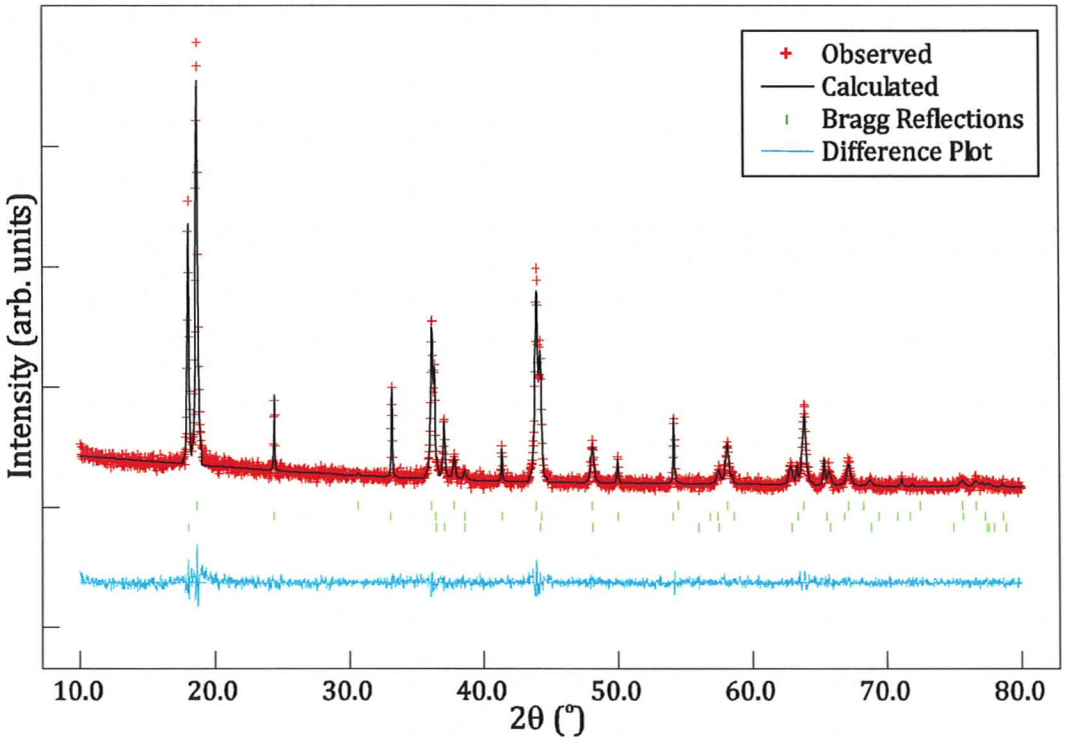

Figure A-12. X-ray diffraction pattern of Sample13. Impurity phases $LiVO_2$ (bottom tick marks) and V_2O_3 (middle tick marks). Crystallographic data are recorded in Table 3-3.

References

[1] O. Muller, R. Roy. *The Major Ternary Structural Families*. Springer-Verlag: New York (1974).

[2] M.M. Thackeray, S.D. Baker, K.T. Adendorff, J.B. Goodenough. *Solid State Ionics*. 17 (1985) 175.

[3] D. Larcher, G. Sudant, J.B. Leriche, Y. Chabre, J.M. Tarascon. *J. Electrochem. Soc.* 149 (2002) A234.

[4] M.M Thackeray, W.I.F. David, J.B. Goodenough. *Mater. Res. Bull.* 17 (1982) 785.

[5] V. Sivakumar, S. Kumar, C.A. Ross, Y. Shao-Horn. *IEEE Trans. Magn.* 43 (2007) 3121.

[6] M.M. Thackeray, W.I.F. David, P.G. Bruce, J.B. Goodenough. *Mater. Res. Bull.* 18 (1983) 461.

[7] L.A. de Picciotto, M.M. Thackeray. *Mat. Res. Bull.* 20 (1985) 1409.

[8] D.W. Murphy, M. Greenblatt, S.M. Zahurak, R.J. Cava, J.V. Waszczak, G.W. Hull, Jr., R.S. Hutton. *Rev. Chim. Minér.* 19 (1982) 441.

[9] A.S. Wills, N.P. Raju, C. Morin, J.E. Greedan. *Chem. Mater.* 11 (1999) 1936.

[10] C.R. Wiebe, P.L. Russo, A.T. Savici, Y.J. Uemura, G.J. MacDougall, G.M. Luke, S. Kuchta, J.E. Greedan. *J. Phys. Condens. Matter*. 17 (2005) 6469.

[11] R.L. Carlin, A.J. van Duyneveldt. *Magnetic Properties of Transition Metal Compounds*. Inorganic Chemistry Concepts 2. Springer-Verlag: New York (1977).

[12] F.E. Mabbs, D.J. Machin. *Magnetism and Transition Metal Complexes*. Lectures in Chemistry at the University of Manchester. Chapman and Hall: London (1973).

[13] J.S. Smart. *Effective Field Theories of Magnetism*. W.B. Saunders Company: Philadelphia & London (1966).

[14] J.B. Goodenough. *Magnetism and the Chemical Bond*. Interscience Publishers: New-York (1963).

[15] J. Kanamori. *J. Phys. Chem. Solids*. 10 (1959) 87.

[16] J.E. Greedan. *J. Mater. Chem.* 11 (2001) 37.

[17] G.H. Stout, L.H. Jensen. *X-ray Structure Determination: A Practical Guide.* The Macmillan Company: New York (1968).

[18] G. Will. *Powder Diffraction: The Rietveld Method and the Two Stage Method to Determine and Refine Crystal Structures from Powder Diffraction Data.* Springer: Berlin (2006).

[19] J.S. Blakemore. *Solid State Physics, 2nd Ed.* Cambridge University Press: Cambridge (1985).

[20] H.M. Rietveld. *J. Appl. Cryst.* 2 (1969) 65.

[21] M. Tinkham. *Introduction to Superconductivity, 2nd Ed.* McGraw-Hill, Inc.: New York (1996).

[22] T. Van Duzer, C.W. Turner. *Principles of Superconductive Devices and Circuits, 2nd Ed.* Prentice Hall PTR: Upper Saddle River, NJ (1999).

[23] C.P. Poole, Ed. *Handbook of Superconductivity.* Academic Press: San Diego (2000).

[24] H.L. Cuthbert. *Ph.D. Thesis.* McMaster University: Hamilton (2009).

[25] B. Reuter, J. Jaskowsky. *Angew. Chem.* 72 (1960) 209.

[26] A. Krimmel, A. Loidl, M. Klemm, S. Horn, H. Schober. *Phys. Rev. Lett.* 82 (1999) 2919.

[27] Y. Nakajima, Y. Amamiya, K. Ohnishi, I. Terasaki, A. Maeda, K. Uchinokura. *Physica C.* 185-189 (1991) 719.

[28] S. Kondo, D.C. Johnston, L.L. Miller. *Phys. Rev. B.* 59 (1999) 2609.

[29] L.A. de Picciotto, M.M. Thackeray. *Mat. Res. Bull.* 20 (1985) 187.

[30] D.B. Rogers, J.L. Gillson, T.E. Gier. *Solid State Commun.* 5 (1967) 263.

[31] Y. Matsushita, J.I. Yamaura, Y. Ueda. *Acta Crystallogr. Sect. E: Struct. Rep. Online.* 61 (2005) i137.

[32] Y. Matsushita, H. Ueda, Y. Ueda. *Nat. Mater.* 4 (2005) 845.

[33] S. Das, X. Zong, A. Niazi, A. Ellern, J.Q. Yan, D.C. Johnston. *Phys. Rev. B.* 76 (2007) 054418.

[34] B.L. Chamberland, T.A. Hewston. *Solid State Commun.* 58 (1986) 693.

[35] S. Kondo, D.C. Johnston, C.A. Swenson, F. Borsa, A.V. Mahajan, L.L. Miller, T. Gu, A.I. Goldman, M.B. Maple, D.A. Gajewski, E.J. Freeman, N.R. Dilley, R.P. Dickey, J. Merrin, K. Kojima, G.M. Luke, Y.J. Uemura, O. Chmaissen, J.D. Jorgensen. *Phys. Rev. Lett.* 78 (1997) 3729.

[36] Y. Ueda, N. Fujiwara, H. Yasuoka. *J. Phys. Soc. Jap.* 66 (1997) 778.

[37] F. Takagi, K. Kawakami, I. Maekawa, Y. Sakai, N. Tsuda. *J. Phys. Soc. Jap.* 56 (1987) 444.

[38] H. Kessler, M.J. Sienko. *J. Chem. Phys.* 55 (1971) 5414.

[39] H. Kaps, M. Brando, W. Trinkl, N. Büttgen, A. Loidl, E.W. Scheidt, M. Klemm, S. Horn. *J. Phys. Condens. Matter.* 13 (2001) 8497.

[40] D.C. Johnston, C.A. Swenson, S. Kondo. *Phys. Rev. B.* 59 (1999) 2627.

[41] O. Chmaissem, J.D. Jorgensen, S. Kondo, D.C. Johnston. *Phys. Rev. Lett.* 79 (1997) 4866.

[42] C. Urano, M. Nohara, S. Kondo, F. Sakai, H. Takagi, T. Shiraki, T. Okubo. *Phys. Rev. Lett.* 85 (2000) 1052.

[43] A. Krimmel, A. Loidl, A.P. Murani, J.R. Stewart, A. Ibarra-Palos, P. Strobel. *Acta Phys. Polon., B.* 34 (2003) 625.

[44] A. Shimoyamada, S. Tsuda, K. Ishizaka, T. Kiss, T. Shimojima, T. Togashi, S. Watanabe, C.Q. Zhang, C.T. Chem, Y. Matsushita, H. Ueda, Y. Ueda, S. Shin. *Phys. Rev. Lett.* 96 (2006) 026403.

[45] V. Eyert, K.H. Höck, S. Horn, A. Loidl, P.S. Riseborough. *Europhys. Lett.* 46 (1999) 762.

[46] V.I. Anisimov, M.A. Korotin, M. Zölfl, T. Pruschke, K. Le Hur, T.M. Rice. *Phys. Rev. Lett.* 83 (1999) 364.

[47] J. Matsuno, A. Fujimori, L.F. Mattheiss. *Phys. Rev. B.* 60 (1999) 1607.

[48] D.J. Singh, P. Blaha, K. Schwarz, I.I. Mazin. *Phys. Rev. B.* 60 (1999) 16359.

[49] I.A. Nekrasov, Z.V. Pehelkina, G. Keller, T. Pruschke, K. Held, A. Krimmel, D. Vollhardt, V.I. Anisimov. *Phys. Rev. B.* 67 (2003) 085111.

[50] R. Arita, K. Held, A.V. Lukoyanov, V.I. Anisimov. *Phys. Rev. Lett.* 98 (2007) 166402.

[51] K. Le Hur. *Phys. Rev. B.* 75 (2007) 014435.

[52] P.E. Jönsson, K. Takenaka, S. Niitaka, T. Sasagawa, S. Sugai, H. Takagi. *Phys. Rev. Lett.* 99 (2007) 167402.

[53] V. Yushankhai, P. Thalmeier, T. Takimoto. *Phys. Rev. B.* 77 (2008) 125126.

[54] H. Tsunetsugu, K. Hattori, T. Ohashi, N. Kawakami, T Momoi. *J. Phys.: Conf. Ser.* 145 (2009) 012015.

[55] A.C. Larson, R.B. Von Dreele. *General Structure Analysis System (GSAS).* Los Alamos National Laboratory, Report LAUR 86-748 (2000).

[56] B.H. Toby. *J. Appl. Crystallogr.* 34 (2001) 210.

[57] R.J. Hill, C.J. Howard. *J. Appl. Cryst.* 20 (1987) 467.

[58] Y. Ueda, J. Kikuchi, H. Yasuoka. *J. Magn. Magn. Mater.* 147 (1995) 195.

[59] S.A. Carter, J. Yang, T.F. Rosenbaum, J. Spalek, J.M. Honig. *Phys. Rev. B.* 43 (1991) 607.

[60] A. Manthiram, J.B. Goodenough. *Can. J. Phys.* 65 (1987) 1309.

[61] L.A. de Picciotto, M.M. Thackeray. *Solid State Ionics.* 18 & 19 (1986) 773.

[62] G. Pistoia, M. Pasquali, L.A. de Picciotto, M.M Thackeray. *Solid State Ionics.* 28 (1988) 879.

[63] L.A. de Picciotto, M.M. Thackeray, G. Pistoia. *Solid State Ionics.* 28-30 (1988) 1364.

[64] A. Deschanvres, B. Raveau, Z. Sekkal. *Mater. Res. Bull.* 6 (1971) 699.

[65] M.S. Whittingham, M.B. Dines. *J. Electrochem. Soc.* 124 (1977) 1388.

[66] M. Wagemaker, W.J.H. Borghols, F.M. Mulder. *J. Am. Chem. Soc.* 129 (2007) 4323.

[67] D.C. Johnston, H. Prakash, W.H. Zachariasen, R. Viswanathan. *Mater. Res. Bull.* 8 (1973) 777.

[68] A.H. Mousa, N.W. Grimes. *J. Mater. Sci.* 15 (1980) 793.

[69] R.J. Cava, D.W. Murphy, S. Zahurak, A. Santoro, R.S. Roth. *J. Solid State Chem.* 53 (1984) 64.

[70] M.R. Harrison, P.P. Edwards, J.B. Goodenough. *J. Solid State Chem.* 54 (1984) 136.

[71] J.M. Heintz, M. Drillon, R. Kuentzker, Y. Dossmann, J.P. Kappler, O. Durmeyer, F. Gautier. *Z. Phys. B Condens. Matter.* 76 (1989) 303.

[72] E.G. Moshopoulou. *J. Am. Chem. Soc.* 82 (1999) 3317.

[73] Y. Takahaski, Y. Gotoh, J. Akimoto. *J. Phys. Chem. Solids.* 63 (2002) 987.

[74] D.C. Johnston. *J. Low Temp. Phys.* 25 (1976) 145.

[75] M.R. Harrison, P.P. Edwards, J.B. Goodenough. *Philos. Mag. B.* 52 (1985) 679.

[76] F. Xu, Y.C. Liao, M.J. Wang, C.T. Wu, K.F. Chiu, M.K. Wu. *J. Low Temp. Phys.* 131 (2003) 569.

[77] H.X. Geng, A.F. Dong, G.C. Che, W.W. Huang, S.L. Jia, Z.X. Zhao. *Physica C.* 431 (2005) 53.

[78] C.P. Sun, Y.F. Huang, S.T. Tsai, C.L. Huang, H.D. Yang. *Physica B.* 378-380 (2006) 395.

[79] C.Q. Feng, L. Li, Z.P. Gwo, D.Q. Shi, R. Zeng, X.J. Zhu. *J. Alloys Compnds.* 478 (2009) 767.

[80] S. Massidda, J. Yu, A.J. Freeman. *Phys. Rev. B.* 38 (1988) 11352.

[81] T. Oda, M. Shirai, N. Suzuki, K. Motizuki. *J. Phys. Condens. Matter.* 6 (1994) 6997.

[82] C.P. Sun, J.Y. Lin, S. Mollah, P.L. Ho, H.D. Yang, F.C. Hsu, Y.C. Liao, M.K. Wu. *Phys. Rev. B.* 7 (2004) 054519.

[83] L. Tang, P.Y. Zou, L. Shan, F. Dong, G.C. Che, H.H. Wen. *Phys. Rev. B.* 73 (2006) 184521.

[84] W. Ra, M. Nakayama, Y. Uchimoto, M. Wakihara. *J. Phys. Chem. B.* 109 (2005) 1130.

[85] M. Anicete-Santos, L. Gracia, A. Beltrán, J. Andrés, J.A. Varela, E. Longo. *Phys. Rev. B.* 77 (2008) 085112.

[86] E.F. Bertaut, J. Dulac. *Phys. Chem. Solids.* 21 (1961) 118.

[87] F. Bertaut, F. Forrat, J. Dulac. *Compt. Rend.* 249 (1959) 726.

[88] J. Dulac. *Bull. Soc. Fr. Minéral. Cristallogr.* 92 (1969) 25.

[89] G. Blasse, D.J. Schipper. *Phys. Lett.* 5 (1963) 300.

[90] G. Blasse. *Philips Res. Rep.* 18 (1963) 383.

[91] D.R. Lide (ed.). *CRC Handbook of Chemistry and Physics, 89th Edition 2008-2009*. CRC Press, Cleveland, Ohio (2009). Accessed online at http://www.hbcpnetbase.com.libaccess.lib.mcmaster.ca/.

[92] H. Leiva, R. Kershaw, K. Dwight, A. Wold. *Mater. Res. Bull.* 17 (1982) 1539.

[93] S. Zhuo, K. Sohlberg. *J. Solid State Chem.* 179 (2006) 2126.

[94] R.D. Shannon. *Acta Cryst.* A32 (1976) 751.

[95] A.J.C. Wilson, Ed. *International Tables for Crystallography, Volume C.* Kluwer Academic Publishers: Dordrecht, the Netherlands (1992).